Carbon-carbon coupling reactions catalysed by palladium nanoparticles supported on the green alga *Ulva armoricana*

BY

FRANKLIN QUELAIN DE BRUIN

B.Sc. Chemical Science, B.Sc.Honours Chemical Sciences

A thesis submitted in partial fulfilment of the requirement for the

Degree of *Magister Scientiae* in Nanoscience in the Department of Chemistry

University of the Western Cape, South Africa

Supervisor

Dr Edith Antunes

Co-supervisors

Prof Denzil Beukes

March 2018

Declaration

I, Franklin Quelain De Bruin, hereby declare that this mini dissertation is my own work and effort and that it has not been submitted anywhere for any award. Where other sources of information have been used, they have been acknowledged and referenced.

Student_______________________________ Date___________________________

Supervisor________________________ Date________________________

Co-supervisor______________________ Date________________________

Co-supervisor______________________ Date________________________

Acknowledgements

A huge thank you to everybody who contributed in their unique ways for the completion of this dissertation.

In particular, I would like to thank:

- Without a doubt the greatest supervisor Professor Edith Antunes for her guidance input encouragement and expertise during the period and completion of the dissertation.
- The collaborators of this project, in particular:
- Prof Denzil Beukes my co-supervisor
- Prof John Bolton
- Martin Stillman
- Dr Subelia Botha at University of the Western Cape (for TEM, EDX and SAED).
- Ms Riana Roussouw at Stellenbosch University (for ICP-AES analyses).
- Dr Remy Bucher at iThembaLabs (for XRD analyses).
- Ms Valencia Jamalie for taking care of the bursary and also purchasing all the necessary reagents and materials required for the project.
- The financial support of this project from the National Nanoscience Postgraduate Teaching and Training Platform (NNPTTP), Department of Science and Technology (DST) and University of the Western Cape, without your financial contribution this project would have not been feasible.
- My family and friends, your encouragement and prayers helped me all the way through.
- All my friends and colleagues from the Marine Biodiversity Research Group (University of the Western Cape) for their continuous support, encouragement, words of advice and help.
- Friends and colleagues from the chemistry department (University of the Western Cape).

Dedication

This work is dedicated to my parents Enoch and Astred De Bruin.

Nellie Williams

Close friends and family.

Abigail Sharolene Meyer

Academic Output

The following section lists technology transfer activities (posters, conference) derived from the results obtained from this research work.

Conferences:

Carbon-carbon coupling reactions catalysed by palladium nanoparticles supported on the green alga *Ulva armoricana* De Bruin F[a], Bolton, J[b], Stillman MJ[c], Beukes D[d], and Antunes E[e]. SACI INORGANIC 2017 incorporating the Carman symposium. Arabella Hotel and Spa, Hermanus, Western Cape.

Carbon-carbon coupling reactions catalysed by palladium nanoparticles supported on the green alga *Ulva armoricana*. De Bruin F[a], Bolton, J[b], Stillman MJ[c], Beukes D[d] , Antunes E[e] South African Marine Natural products symposium. Department of Chemistry, University of the Western Cape, Bellville, 7535.

Abstract

The synthesis of nanomaterials, especially metallic nanoparticles, has attracted an enormous amount of interest over the past decade. They exhibit unique properties that allow the multiple applications in a variety of fields in science and technology. Their applications are limited by the efficiency and control of their synthesis to produce nanoparticles of certain size and shape. With ever mounting concern for the environment, a great amount of research has recently been extended to synthetic procedures that are carried out with limited or no toxicity to human health and the environment. One method involves the use of biological (or biogenic) materials for nanoparticle synthesis. This method is particularly attractive due to the fact that it is a relatively cheap, simple and environmentally friendly method compared to that of conventional chemical methods of synthesis.

A possible route for the synthesis of the metal nanoparticles is through the production of nanoparticles by living plants, as they are known to bio-accumulate metals when exposed to metal salts. The plants are thus able to reduce these metal salts to form crystalline nanoparticles. Synthetic methods using living plants has been reported for Au, Cu, Ag, and Pt. Several papers on the bioaccumulation of palladium nanoparticles (PdNPs) and their use as a catalyst for a range of carbon-carbon coupling reactions such as Heck, Shinogoshira and Suzuki reactions have been reported.

The synthesis of PdNPs using marine algae has been largely unexplored, therefore stimulating our interest. Thus, a green method for the synthesis of PdNPs using living Ulva armoricana is presented. The nanoparticles were characterized using HRTEM, HRSEM and XRD, together with UV/Visible and ICP-OES spectroscopies. The prepared PdNPs were then evaluated as catalysts in Suzuki carbon-carbon coupling reactions were the cross-coupling of alkyl boronic acids with alkyl halides where performed and the products characterized using NMR studies and GC-EIMS.

Contents

List of figures

List of tables

List of equations

List of Abbreviations and Symbols

^{13}C	Carbon NMR
^{1}H	Proton NMR
ATR–FT-IR	Attenuated total reflection Fourier transform infrared spectroscopy
BE	Binding energy
BSE	Back scattered electrons
BTB	Boron tributylamine
$CDCl_3$	Deuterated chloroform
CTAB	Cetyltrimethylammonium
CRT	Cathode ray tube
DLS	Dynamic light scattering
DNA	Deoxyribonucleic acid
EDL	electric double-layer
EDX	Energy dispersive X-Ray spectroscopy
E_k	Kinetic energy
EPA	Environmental Protection Agency
eV	Electron volt
fcc	Face cantered cubic
FDA	Food and Drug Administration
FEG	Field-emission gun
FESEM	Field emission microscope
FT-IR	Fourier transform infrared spectroscopy
GC-MS	Gas chromatography – Mass spectroscopy
h	Hour
HMBC	Heteronuclear multiple bond correlation
hrs	Hours

HRTEM	High resolution transmission electron microscopy
HRSEM	High resolution scanning electron microscopy
HAS	hemispherical analyser
HSQC	Heteronuclear single quantum correlation
Hz	Hertz
MHz	Mega Hertz
MS	Mass spectroscopy
ICP-AES	Inductively coupled plasma atomic emission spectroscopy
ICP-OES	Inductively coupled plasma optical emission spectrometry
IR	Infrared
KeV	Kilo electron volt
M^+	Metal ion
Min	Minutes
mM	Millimolar
$mol.L^{-1}$	Mole per litre
mV	Millivolts
nm	Nanometer
NMR	Nuclear magnetic resonance spectroscopy
NMs	Nanomaterials
NPs	Nanoparticles
OHC	Oil holding capacity
PAMMAM	poly (amidoamine)
Pd/C	Palladium on carbon
PPI	(propylene imine)
PVA	poly (vinyl alcohol)
PVP	poly (*N*-vinyl-2-pyrrolidone)

PdNPs`	Palladium nanoparticles
PEG	Polyethylene glycol
ppm	Parts per millions
PUFA	Polyunsaturated fatty acids
QELS	Quasi-Elastic Light Scattering
SAED	Selected area electron diffraction
SAFA	Saturated fatty acids
SE	Secondary electrons
SEM	Scanning electron microscopy
SWC	Swelling capacity
T	Ton
TEM	Transmission electron microscopy
TGA	Thermal gravimetric analysis
TOP	palladium-trioctlyphosphine
UPS	Universal power supply
UV-Vis	Ultra Violet - Visible spectrophotometry
WHC	Water holding capacity
XPS	X-ray photoelectron spectroscopy
XRD	X-ray powder diffraction spectroscopy
ZP	Zeta potential
Å	Angstrom
d	Doublet
dd	Doublet of doublets
Θ	Bragg diffraction angle (Theta)
Δ	Delta
λmax	Maximum wavelength
m	multiplet
q	quartet
s	singlet
t	triplet

td	triplet of doublets
ζ	Zeta potentia

Chapter 1 Introduction

1.1 Outline

In this chapter, a general overview of the study that will be conducted is given such as the background, problem statement, rationale and motivation, aims and research objectives. A brief introduction to the conventional methods used for the synthesis of transition metal nanoparticles, issues encountered using these conventional methods and the applications of these nanoparticles is given. More importantly, highlights for new "green" methods for the synthesis of these nanoparticles and a brief background on the green seaweed *Ulva armoricana* will be given and discussed.

1.2 Background

Recently a cross roads between biological based technologies, green chemistry and nanotechnology has taken place. The objective of this convergence is to create advanced materials and manufacturing processes that reduce or eliminate the use of hazardous substances that may negatively impact the environment. An important part of nanotechnology is the synthesis of nanoscale materials and the control of particle morphology and dimensions during their formation (Goodsell, 2004; Shah *et al*., 2015). Nanometer scale materials have at least one dimension less than 100 nm and can have a wide variety of geometric shapes such as plates, sheets, tubes, wires, and particles. Numerous studies have shown that nano scale materials exhibit unique chemical, physical, electronic, optical, thermal, mechanical and biological properties that differ significantly from their bulk scale counterparts (Bogunia-Kubik and Sugisaka, 2002). These unique properties result from the extremely small size, shape and the quantum confinement of their electrons. In addition, because of their small size, nanomaterials can act as bridge between bulk scale materials and molecular structures. In terms of composition, nanomaterials can be broadly classified into two types, namely, organic and inorganic materials (Naiwa, 2000). Organic nanomaterials are carbon based, while inorganic nanomaterials include noble metals (gold, platinum and silver), magnetic materials (metal oxide or metal hydrides) and semiconductors such as titanium dioxide and zinc oxide (Mohanpuria *et al*., 2008).

The physicochemical properties of bulk scale materials are understood but the recent achievements in the manipulation of the region between the atomic scale and the much larger bulk scale, has led to major discoveries and breakthroughs. These discoveries arise from the significant increase in the surface area to volume ratio when bulk scale materials are reduced into much smaller amounts (Baker *et al*., 2013). The larger surface area to volume ratio found in nanometer scale materials is but one factor that influences the physiochemical properties. Thus, at the nanometer scale there is significant changes in both surface chemistry and chemical reactivity (Iravani, 2011).These unique size-dependent properties have led to nanoparticles being promoted for a wide, versatile range of applications. Typical applications include biosensors catalysts, environmental remediation, labelling for immunoassays, and hyperthermia treatment of tumours, antibacterial drugs and vector delivery of therapeutic drugs for cancer treatments (Rafie *et al*., 2013). It is of the utmost importance to control particle size and shape during manufacture (Gamal, 2010). Thus, effective control during production enables the customization of nanoparticles for specific applications. The synthesis of nanoparticles can be broadly defined into two approaches. The first is the top down approach and involves a material undergoing significant size reduction via physical or chemical processes (Kannan *et al*., 2013). During size reduction, the resulting particle size, shape, and surface structure are heavily dependent on the technique used. Unfortunately, size reduction also tends to introduce surface imperfections and reduced uniformity that can significantly impact the overall physicochemical properties of the fabricated nanoparticle. The second, bottom up approach builds nanoparticles via the assembly of atoms, molecules, and smaller particles or monomers (Rafie *et al*., 2013).

However, the chemical and physical processes used in both approaches have several drawbacks such as low material conversion rates, they are technically complex, they have high energy requirements, and they are expensive methods. Furthermore, many of these processes employ hazardous chemicals such as reducing agents, organic solvents and stabilizing agents (Chanda *et al*., 2010). Processes such as chemical precipitation and pyrolysis often result in toxic chemical species deposition on the surface of newly formed nanoparticles. The presence of surface contaminants such as harmful chemicals makes these nanoparticles unsuitable for clinical and biomedical applications. Thus a growing interest in developing new eco-friendly production technologies based on the principles of green chemistry and green nanotechnology has been apparent (Khan *et al*., 2008).

To emphasise this alternative approach, recent research has focused on using biological entities to synthesize a wide variety of nanoparticles. Biosynthesis via unicellular and multicellular biological entities such as actinomycetes, bacteria fungus, marine algae, plants, viruses and yeast offer alternative approaches for producing nanoparticles. Each of these biological entities, to varying degrees, can perform as natural bio factories for producing particular nanoparticles. Each of the above entities have merits as well as active molecules and compounds that can act as reducing agents and stabilizing agents to synthesize nanoparticles with diverse sizes, shapes, compositions and physicochemical properties (Smit *et al*., 2008).

Thus, the interest of this study focuses on the use of marine resources namely seaweeds (algae) as a possible source for the biogenic synthesis of nanoparticles. The marine environment covers roughly 70% of the earth’s surface and is largely unexplored. Recent studies have shown that several marine plants have the ability to perform as biogenic sources for the production of nanoparticles (Kim, 2011).

Marine algae contains a diverse range of different species, which are generally classified into two groups, namely, microalgae and macroalgae. Microalgae species such as phytoplankton and cyanobacteria survive suspended in the water column, while macroalgae (commonly known as seaweeds) are plant-like organisms that can range in size from a few centimetres up to several meters in length. Algae are classified into three groups based on the algal body or thallus pigmentation (Gautam and Veggel., 2013). The color groups are brown algae (phaeophytes), green algae (chlorophytes) and red algae (rhodophytes). Brown and red algae are predominantly marine based, with some species of red algae are found at water depths where light levels are extremely low, while green algae is found in both marine and freshwater environments (Gautam and Veggel., 2013). Studies have revealed that seaweeds are a rich source of biologically active compounds such as carbohydrates, carotenoids, polysaccharides, proteins, vitamins, and numerous secondary metabolites. The studies have also shown the active compounds present in seaweeds have medicinal properties that can be used in conventional treatments and alternative therapies. In addition, seaweeds are also found to be capable of accumulating heavy metals and the secondary metabolites of several types of seaweed have anti-biological fouling properties amongst other properties (Gautam and Veggel, 2013). Recent studies have reported the biological reduction of metal ions in aqueous based seaweed solutions and they have confirmed that the various active compounds present in seaweeds can act as both metal reducing agents and capping agents during the formation of stable nanoparticles (Cedervall et al., 2007). Yet using live seaweeds has not yet been explored thus in this study we propose the synthesis of palladium nanoparticles using live seaweed.

1.3 Problem statement

Metallic NPs have been prepared by several physical and chemical approaches depending on the accessibility and viability of procedures in solution using several chemical reductants, such as hydrazine hydrate, sodium borohydride, tri-sodium citrate which are not environmentally friendly. Furthermore, to accomplish stable dispersions of nanoparticles for use in several applications, hazardous stabilizers are frequently employed to avoid aggregation. These approaches have been widely applied, but the stabilizers, reactants, reductants, and several organic solvents employed in these approaches are toxic and hazardous to the environment (Biazar *et al*., 2011).

Most of the chemical approaches need a huge quantity of toxic organic solvents to assist in the stabilization of nanoparticles by using various capping agents. Most of these capping agents are hydrophobic and the adsorption of such toxic chemicals on the NPs' surfaces increases severe toxicity concerns and strictly hinders the biological applications of such nanomaterials (Jain *et al*., 2013).

Among the approaches considered for the synthesis of nanoparticles, the utilization of algal extracts has enticed substantial consideration, due to easy sampling and cost efficiency, enabling the large scale biosynthesis of NPs. Algal extracts comprise of a wide range of naturally occurring chemical compounds, which are generally recognized as marine natural products. These marine natural products possess a variety of biological activities due to their exceptional variance in their chemical structures (Salt *et al*., 1995). These marine based molecules present in algal extracts not only enable the synthesis of the nanoparticles by acting as reducing agents, but it also functions as stabilizing agents. Thus the synthesis of palladium nanoparticles using live *Ulva armoricana* seaweed in this study.

There are numerous examples of nanoparticles that were synthesised using extracts from marine sources as well as terrestrial plants. These nanoparticles that are produced are used in various catalytic reactions such as Heck, Shinogoshira reaction and Suzuki coupling reactions (Parker *et al*., 2014).

On the South African science scene, green nanotechnology is a relatively new avenue and aims at achieving certain goals in applying the principles of green chemistry to create eco-friendly technologies which resolve day to day problems. One of the major policy mandates, strategies and objectives of the Centre for green Nanotechnology launched in South Africa, is the synthesis and development of green, biocompatible NPs for medical diagnostic/therapeutic agents, biological sensors, chemical sensors, smart electronic materials, nanoscale robots and environmentally benign breathing devices (Iravani *et al*., 2011).

1.4 Rationale and motivation

The research interests for this study have been encouraged by a need to be innovative in designing green synthetic methods for PdNPs through the use of live green *Ulva armoricana* seaweeds. At present there are very few reports in the literature describing the use of marine and freshwater algae to produce metal nanoparticles other than Ag and Au (Mukhoro *et al*., 2017). Thus research has to be spear headed by the use of more eco-friendly methods such as using seaweeds directly rather than using extracts which will reduce the number of process as well as waste generated during synthesis of the NPs. However, (Scarano and Morelli, 2003) have reported using the marine phytoplanktonic alga (Phaeodactylum tricornutum Bohlin) to biosynthesize cadmium sulphide (CdS) nanocrystallites when the alga was immersed in aqueous solutions containing Cd ions. Recently the formation of crystalline spherical Pd nanoparticles within green microalgae (*Chlorella vulgaris*) via photosynthetic reactions when the microalgae was immersed in aqueous solutions containing $Na_2(PdCl_4)$ have been reported. Therefore the design and synthesis for PdNPs supported on *Ulva armoricana* will be assessed for its catalytic ability in several carbon-carbon coupling reactions.

1.5 Aims and objectives

1.5.1 Main aims

The study was comprised of two main aims and they are as follows:

1.Synthesis of palladium nanoparticles using the live marine seaweed *Ulva amoricana*. Characterisation of the nanoparticles fully using UV-Vis, HRTEM, ICP-AES, XRD, SEM, TEM, DLS, TGA and FT-IR.

2. Use the bio synthesised PdNPs to demonstrate catalytic activity in Suzuki coupling reactions between a varieties of boronic acid aryl halides. Compare these *Ulva* supported PdNPs to the commercially available catalyst 10% wt Pd/C.

1.5.2 Specific Objectives

Several objectives were set-out to achieve the aim of the study as follows:

1. Collection of seaweed.

2. Optimization of the concentration of palladium salt that will be used in the synthesis of the NPs.

3. Optimization of the amount of live *Ulva armoricana* seaweed used in the palladium reduction process.

4. Characterization of PdNPs synthesized using the live marine seaweed *Ulva armoricana* using various techniques such as UV-Vis, HRTEM, ICP-AES, XRD, SEM, TEM, DLS, TGA and FT-IR.

5. To use the bio-synthesised PdNPs in Suzuki carbon-carbon coupling reactions between boronic acids and a range of aryl halides and compare the catalytic PdNPs to commercially available 10% wt Pd/C catalyst.

1.5.3 Research questions

- Can live *Ulva armoricana* seaweeds be used as an alternative green biosynthetic method for eco-friendly PdNPs?

- Can the *Ulva armoricana* supported PdNPs be used in the Suzuki carbon-carbon coupling reactions between boronic acids and aryl halides and compare its catalytic performance to commercially available 10% wt Pd/C catalyst.

1.5.4 Outline of the thesis

Chapter 1: The chapter gives some background to the study, including a brief discussion on the conventional methods used for metallic nanoparticle synthesis, issues encountered using conventional methods, applications of these nanoparticles and the importance of green synthetic methods, in addition to a brief review on the green seaweed *Ulva armoricana*. The research problem and its importance, the study's aim and objectives, research questions as well as the outline of the thesis are also presented.

Chapter 2: This chapter presents the general literature on the principles of green chemistry, the biosynthesis of nanoparticles using marine organisms, the methods used in the synthesis of different nanoparticles, some background on *Ulva armoricana*, the techniques used in the characterization of nanoparticles and applications of PdNPs.

Chapter 3: This chapter reports the synthesis of PdNPs using the live marine seaweed *Ulva armoricana* and the characterization of the resultant NPs produced using a selection of techniques such as UV-Vis spectroscopy, HRTEM, ICP-AES, XPS, XRD, SEM, TGA and FT-IR spectroscopy.

Chapter 4: This chapter reports and demonstrates the catalytic activity of the PdNPs versus the commercially available Pd/C catalyst in Suzuki coupling reactions between the boronic acids and a variety aryl halides.

Chapter 5: Contains a detailed discussion for the synthesis of the *Ulva* supported PdNPs and their application to the Suzuki carbon-carbon coupling reaction.

Chapter 2 Literature review

2.1 Green chemistry

In modern synthesis one of the most important new aspects of chemistry is the development of green Synthetic Chemistry processes and the practise of green Chemistry. Supported by the American Chemical Society, the USEPA and other Federal agencies, green Chemistry has prevailed as an important aspect of all chemistry. Green Chemistry is the design of chemical products and processes that reduce or eliminate the use and generation of hazardous substances. Green Chemistry is based on twelve Principles (Anastas *et al*., 1998).

- **Prevention:** Try not to produce waste, then you do not have to clean it up.
- **Atom economy:** The final product should aim to contain all the atoms used in the process.
- **Less hazardous chemical synthesis:** Wherever it is possible, production methods should be designed to make substances that are less toxic to people or the environment.
- **Designing safer chemicals:** Chemical products should be designed to do their job with minimum harm to people or the environment.
- **Safer solvents**: When making materials try not to use solvents or other unnecessary chemicals. If they are needed then they should not be harmful to the environment in any way.
- **Design for energy efficiency:** The energy needed to carry out a reaction should be minimized to reduce environmental and economic impact. If possible, processes should be carried out at ambient temperatures and pressures.
- **Use of renewable feedstocks:** A raw material should be renewable wherever possible**.**
- **Reduce derivatives:** Minimise the number of steps in the reaction because this means more reagents are needed and more waste is made.
- **Catalysis**: Reactions that are catalysed are more efficient than uncatalysed reactions.
- **Design for degradation**: When chemical products are finished with, they should break down into substances that are not toxic and do not stay in the environment indefinitely.
- **Real-time analysis for pollution prevention**: Methods need to be developed so that harmful products are detected before they are made.
- **Inherently safer chemistry for accident prevention**: Substances used in a chemical process should be chosen to minimise the risk of chemical accidents, including explosions and fire.

2.2 Methods to produce palladium nanoparticles

Nanotechnology is responsible for one of the major breakthroughs of modern science, enabling materials of distinctive size, structure and composition to be formed. These nano dimensional materials (in the 1–100 nm size domain) are seen as a bridge between atomic and bulk materials and have been shown to exhibit a variety of unique chemical, physical and electronic properties (Moores and Goettmann, 2006). Exploring these properties has become an increasing priority area in chemistry, physics, and biology, medicine and material sciences. However, reliable preparations of the nanomaterials are required for their manipulation, and this remains an area of active research (Sangeetha and K. Saravanan, 2014).

Given that palladium is one of the most efficient metals in catalysis, the study of palladium-based materials is hugely significant and valuable. As a consequence, palladium nanoparticles of (PdNPs) have been comprehensively studied in a wide range of catalytic applications including hydrogenation, oxidation, carbon–carbon bond formation, and electrochemical reactions in fuel cells (Aiken III and Finke, 1991. A good example of its application is the propensity of palladium to adsorb hydrogen, thus PdNPs are also utilised in hydrogen storage as well as sensing applications (Astruc, 2007).

The preparation of PdNPs with well-controlled particle sizes and shapes of a high monodispersity is a key process in producing materials that are more effective and efficient than the current state of the art. For example, particle size can play a critical role in a catalytic process and a nanoparticle with an optimal size enables the most efficient use of the valuable metal and the highest selectivity in subsequent reactions. In this section of the thesis different methodologies of palladium for the synthesis of PdNPs and factors contributing to stability and morphology, will be discussed (Hou *et al.*, 2005).

2.2.1 Stabilization of palladium nanoparticles

Nanoparticles are typically thermodynamically unstable with high levels of agglomeration. Consequently, they need to be kinetically stabilised and this is typically done using a stabiliser (Brust et al., 1994). Stabilisation is achieved by electrostatic or steric forces or a combination of the two known as (electrosteric forces). The stabiliser is typically introduced during the formation of the nanoparticles, and this is achieved via the chemical or electrochemical reduction or thermal decomposition of metallic precursors. The interaction between the stabiliser and the surface of the nanoparticle is a dynamic one, with its strength and nature often controlling the long-term stability of a nanoparticle dispersion. This interaction can take many forms, such as a strong covalent linkage chemisorbed atom or an electrostatic interaction with a layer of anions. The formation of palladium nanoparticles are stabilised by the most common stabilisers organic ligands, surfactants, polymers and dendrimers (Brust et al., 1994) as depicted in (Figure 2-1).

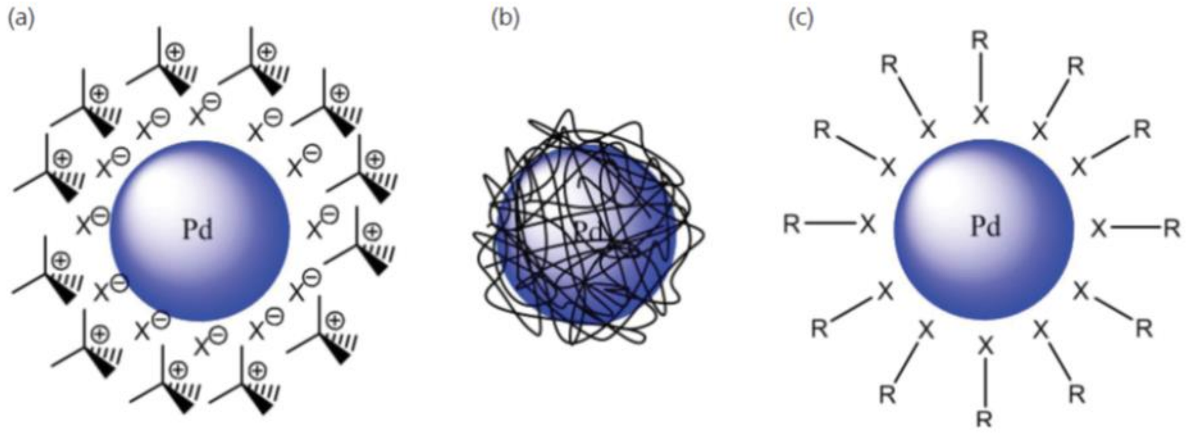

Figure 2-1 Structure representing the stabilisation of palladium nanoparticles using different protecting groups: (a) surficants; (b) polymers; and (c) ligands (J. Cookson., 2012).

2.2.2 Sulphur-based ligands

The strong interaction between the platinum group metals and soft sulphur-based donors make sulphur containing ligands highly efficient stabilisers for nanoparticles (Lee *et al*., 2005). In general, it is the use of thiol and thioether ligands as stabilizers that dominates the literature due to the high stability of the nano structures that they can generate (Chauhan *et al*., 2004). Furthermore sulphur based catalyst's has been demonstrated to be a stable and recyclable catalyst in the Suzuki-Miyaura C–C coupling reaction of halogenoarenes and the phenylboronic acid as demonstrated in (Figure 2-2) by (Lu et al., 2004).

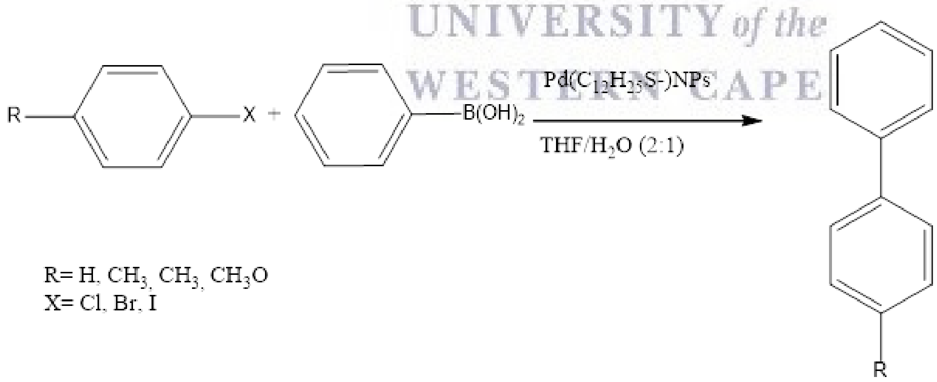

Figure 2-2 Reported catalytic transformation using thiol-stabilised palladium (NPs) for the use in the Suzuki-Miyaura carbon -carbon coupling reaction of halogenoarenes and phenylboronic acid (Lu et al., 2004).

Given that there is much literature on the stabilisation of PdNPs by thiol ligands and that there is a strong interaction between palladium and sulphur, there are surprisingly few other Sulfur-based ligands that have been reported as stabilisers, such as thioether and thioester functional groups (Ganesan *et al*., 2007).

The interaction between these groups and the metal surface is weaker than for thiols, as the ligand is unable to form anionic species via the same mechanism by which thiols readily form thiolates (Huc and

Pelzer, 2008). However, this can lead to advantages, with greater surface accessibility in applications such as catalysis and facile post-synthetic modified cations via ligand displacement reactions (Hussain *et al*., 2005).

2.2.3 Phosphorus-based ligands

The use of phosphorus-containing compounds in the formation of nano systems dates back to the 19th century, when Faraday prepared gold nanoparticles by reducing tetrachloroaurate salts with phosphorus vapours (M. Faraday., 1857). The use of phosphine ligands has been reported by several authors for the preparation of monodisperse palladium nanoparticles. Hyeon and co-workers (Hyeon *et al.*, 2004*)* reported how the thermolysis of a preformed palladium-trioctlyphosphine (TOP) complex yielded such nanoparticles (Kim *et al*., 2003).

2.2.4 Nitrogen-based ligands

The use of electron-rich nitrogen-containing ligands has been extensively used to stabilise precious metal nanoparticles (Mazumder and Sun, 2009). The lone pair of the nitrogen species (such as long-chain primary amines) is able to strongly chemically adsorb onto the surface of the metal, with the alkyl group preventing agglomeration via steric stabilisation (Li *et al*., 2010). Mazumder and Sun prepared monodispersed palladium nanoparticles by reducing $Pd(acac)_2$ in oleylamine with boron tributylamine (BTB) at 90 ^{o}C in (Figure 2-3).

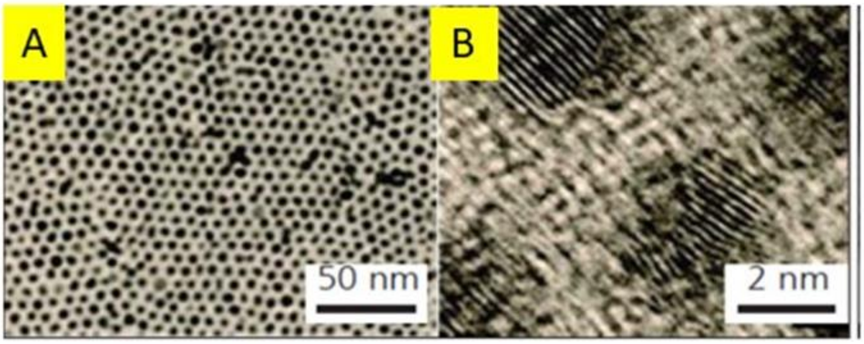

Figure 2-3 (A) TEM; And (B) high resolution-TEM images of 4.5 nm PdNPs prepared by the reduction of $Pd(acac)_2$ in oleylamine and BTB (Cookson., 2012), (Copyright 2009 American Chemical Society).

2.2.5 Other ligands

In general, ligands containing heteroatoms stabilise precious metal nanoparticles by forming strong bonds with the surface. However, recently there have been examples of nanoparticles being stabilised with carbon-based ligands (Chen *et al*., 2006). Palladium has been extensively used as the contact metal of choice in the fabrication of carbon nanotube-based nano-electronic devices and circuitries because of its low contact resistance, and so it is not unexpected that carbon can be used to stabilise nanoparticles (Tarakeshwar and Kim., 2005).

2.2.6 Surfactants

Salts/surfactants is a popular route to stabilising metal nanoparticles. Frequently, tetra-N-alkyl ammonium halide salts are chosen for this purpose, although other analogous materials such as imidazolium-based ionic liquids can act as stabilisers using the same mechanism. Here the stabiliser is able to prevent irreversible agglomeration of the metal via a combination of electrostatic and steric effects. Both elements of the surfactant play a key role in protecting the metal from agglomeration. Changing the nature of the cationic component allows the nanoparticles to be dispersed in either organic or aqueous media (Ishizuka *et al.*, 1994). Furthermore, surfactants such as cetyltrimethylammonium bromide (CTAB) enable the generation of anisotropic particle shapes as depicted in

2.2.7 Polymers

Polymers, such as poly (N-vinyl-2-pyrrolidone) (PVP) and poly (vinyl alcohol) (PVA), are widely used to protect nanoparticles because of their commercial availability at relatively low cost and their solubility in a range of solvents, including water (Toshima and Yoneswa, 1998). The use of polymers is often associated with the 'polyol method', in which a metal precursor is dissolved and reduced at high temperatures by an alcohol (typically ethylene glycol). In (Figure 2-4) a schematic represents the reduction of metal salts in a presence of a stabilising polymer.

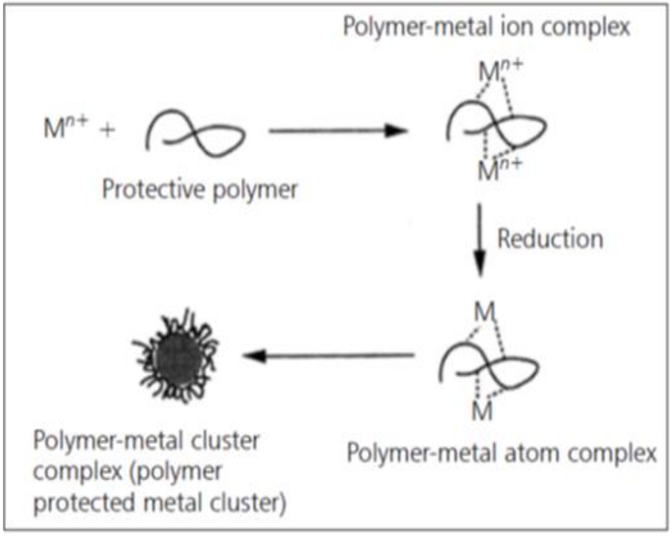

Figure 2-4 Schematic representation of the reduction process of metal salts in the presence of a stabilising polymer (Cookson. 2012), (Royal Society of Chemistry Reproduced with permission).

2.2.8 Dendrimers

Dendrimers are macromolecules that, unlike polymers, are perfectly defined on the molecular level. Their internal cavities behave as molecular boxes that can entrap and stabilise metal nanoparticles, especially if there are heteroatoms present in the interior of the dendrimer (Centomo and Canton, 2004). Two families of dendrimer have been extensively studied and are commercially available: poly (amidoamine) (PAMAM) and poly (propylene imine) (PPI) as shown in (Figure 2-5).

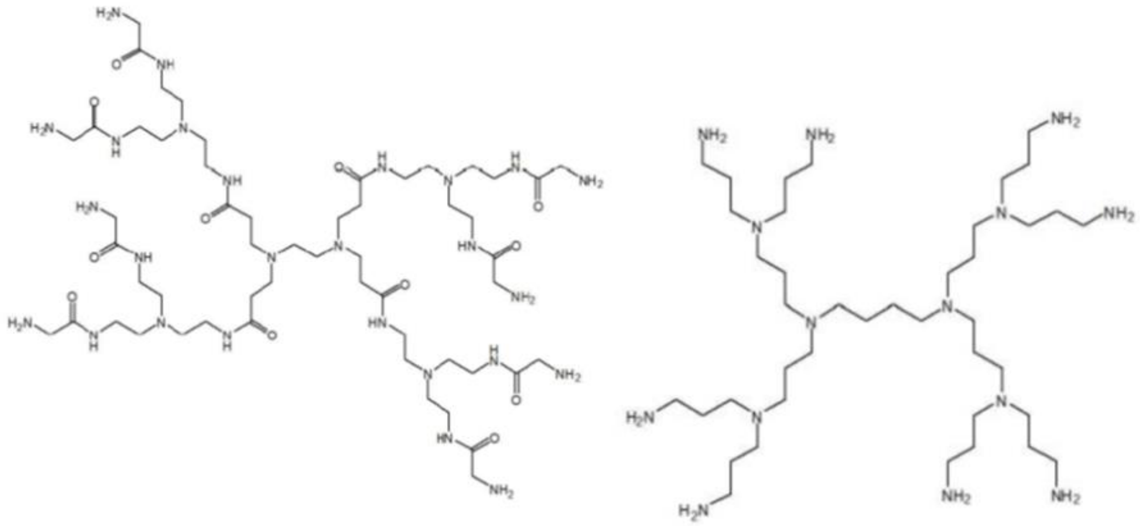

Figure 2-5 Structure of the two most commonly used dendrimer building blocks: poly (amidoamine) (PAMAM) on left and poly (propylene imine) (PPI) and on right (Cookson. 2012).

2.2.9 Electrochemical techniques

Electrochemical technique are commonly employed to reduce metal ions to their zero-valent metallic state directly on the electrode surface. During anodic dissolution metal ions can be produced and then reduced to metallic atoms adsorbed on the cathode surface. The most interesting process is production of metallic nanoparticles in an organic solvent (that acts as electrolyte) and surfactant that acts as a stabilizer and an electrolyte simultaneously (Aiken and Finke, 1991). The adsorbed metallic atoms or nano clusters may be easily trapped by the surfactant to form metal colloid and non-metallic powder a schematic of this is shown in (Figure 2-6).

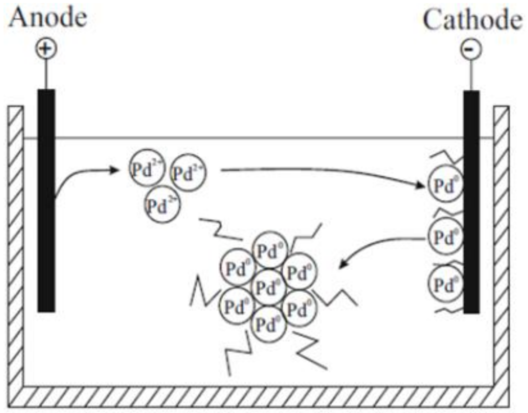

Figure 2-6 Schematic image of metal colloid formation after palladium reduction on cathode surface (Aiken and Finke, 1991).

2.2.10 Biogenic synthesis

Biogenic synthesis of palladium and platinum nanoparticles from plants and microbes has captured the attention of many researchers because it is economical, sustainable and eco-friendly (Mahdavi *et al*., 2013). Plant and their parts are known to have a variety of primary and secondary metabolites which are able to reduce the metal salts to metal nanoparticles. The biogenic fabrication of Pd/Pt nanoparticles, their potential application as catalyst, medicine, biosensor, medical diagnostic and pharmaceuticals (Parker *et al*., 2014).

The main aim of green synthesis is to minimize the use of toxic chemicals to protect the environment from pollution. The biogenic routes for the fabrication of nanomaterials are therefore becoming more and more popular. The three main conditions for nanomaterials preparation are

(i) The choice of an environment-friendly solvent medium,

(ii) The reducing agent

(iii) A nontoxic material for their stabilization.

Nanomaterials fabricated from plants, fungi and bacteria have several potential applications in all fields of science and technology. The reduction of metal ions occur by the proteins, amines, amino acids, phenols, sugars, ketones, aldehydes and carboxylic acids present in the plants and microbes (Eroglu, X. Chen, Bradshaw *et al*., 2013). The geometrical shape, size and stability of nanoparticles may be controlled by monitoring the pH, temperature, incubation time and concentrations of plant extract and that of the metal salt (Eroglu, X. Chen, Bradshaw *et al*., 2013).

Currently the mechanism of how nanoparticles are formed via biosynthetic means is not fully understood. However, studies have revealed that many of the biomolecules found within the cell walls of several terrestrial plants and seaweeds can act as a biocatalysts to assist in the reduction of precursor metal salts for nuclear clusters of metal and metal oxide nanoparticles (Kumar *et al*., 2013). Larger amphiphilic biomolecules can act as surficants which direct and control nanoparticle growth. The biogenic synthesis of nanoparticles is a straightforward room temperature process as seen in (Figure 2-7).

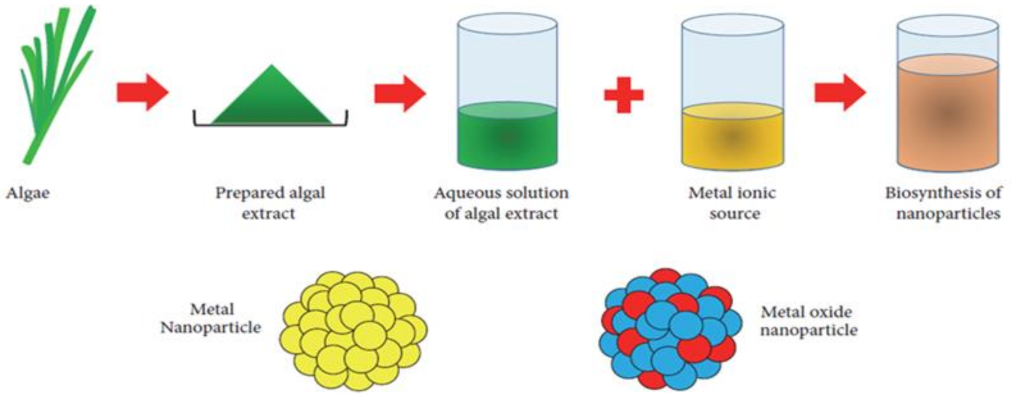

Figure 2-7 Bottom up assembly of atoms via biosynthesis using marine algae and a metallic ionic sources to form metal or metal oxide nanoparticles (Fawcett et al 2017).

This process involves mixing a metal salt solution with an aqueous solution containing either an extract or a live plant or marine plant species. Reduction may start immediately and a colour change is immediately evident in some cases. A good example of this is a recent study by Arockiya *et al*., 2012) gold (Au) nanoparticles were synthesized using brown alga *(Stoechospermum marginaium)*. The growth of nano particles in solution begins with metal ions being converted from their mono or divalent oxidation states to zero-valent states. This is followed by metal ion reduction and then nucleation. Following the initial nucleation a kinetically controlled process takes places in which larger particles are attacked by smaller neighbouring particles attaching to low energy faces and forming crystals to create a thermodynamically stable nano particles (Stalin Dhas *et al*., 2012).

The recent discovery of a green synthetic method for AuNP synthesis using a live marine green seaweed *Ulva armoricana* by (C. Mukhoro *et al*., 2017) has opened a new method for the use of live marine seaweed as bio factories for nanoparticle production. The formation of AuNPs was at first visually observed with a change in solution colour from yellow and to a deep pink colour, and confirmed by monitoring with UV-Vis spectroscopy. UV-Vis spectroscopy showed that the production of AuNPs immersed in the solution after 30 min as observed by an increase in absorbance at the surface plasmon resonance (SPR) band of AuNPs at 550 nm, and a shoulder at 660 nm, up until 120 min, when a decrease in the maximum absorbance was observed at both wavelengths The change in colour is shown in (Figure 2-8).

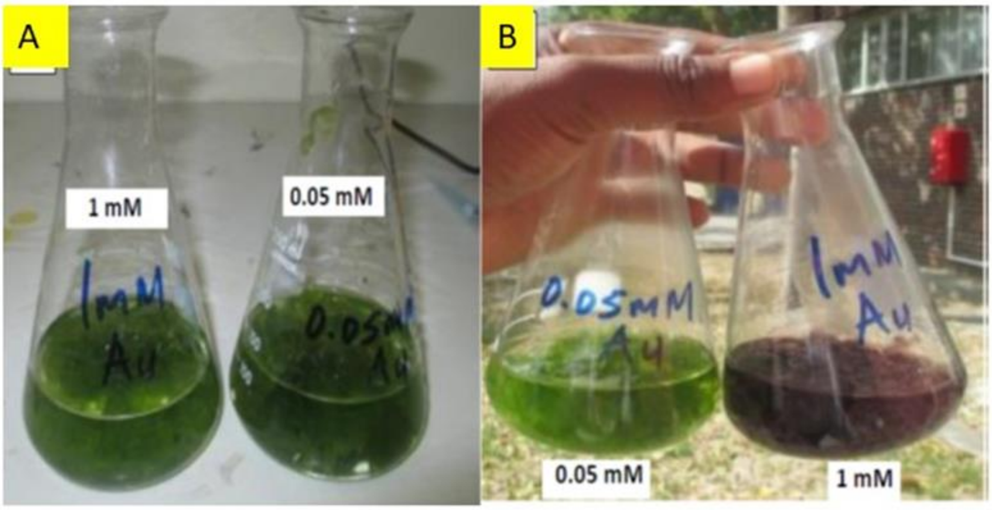

Figure 2-8 green synthesis of AuNPs using live Ulva organism in gold chloride solution concentration of 0.05 mM and 1 mM at time (A) 0 mins and (B) 6 hrs (Mukhoro et al., 2017).

2.3 Application of palladium nanoparticles

Nowadays, the chemical applications of PdNPs is too wide and varied, and only a few important applications are listed below (Li et al., 2011).

These are:

(i) Catalysis for organic coupling reactions
(ii) Hydrogenation of unsaturated olefins
(iii) Alcohol oxidation
(iv) Activation for electroless metal deposition

2.3.1 Catalysis for organic coupling reactions

The coupling reactions of an arylboronic acid with aryl halides provide a versatile route for synthesizing biaryls, which are important precursors for polymers, liquid crystals, *etc*. These types of reactions, called Suzuki coupling reactions, were traditionally catalyzed by a phosphine-ligand palladium complex (Li *et al*., 2011). However, because of such problems as separation from the reaction mixture and catalyst recovery some new approaches were subsequently developed. Today colloidal palladium has become a commercial catalyst for the Suzuki coupling reactions and the effects of particle size on the catalytic efficiency in the Suzuki reactions have been studied in detail (Li *et al*., 2001).

2.3.2 Hydrogenation of unsaturated olefins and hydrogen storage

The PdNP-based composites have been extensively used as affective catalysts for the partial hydrogenation of dienes to alkenes. One of the more promising methods of catalysing hydrogenation of olefins is the use of PdNPs encapsulated with dendrimers (Nui *et al*., 2001). The dendrimers proved to be effective for the separation of chemical species due to their crowded structure. Dendrimers have also been used as stationary phases in various liquid separation techniques (Zhao *et al*., 1999).

2.3.3 Activation for electroless metal deposition

Plating studies of different types of coatings from aqueous solutions without using an external current source were described in the literature as electroless deposition. This chemical process was widely used for the metallation of a nonconductive substrate and predominantly related to metal/ alloy depositions (often Cu; Ni and Co). Deposition of oxides, salts, polymers, *etc*. is also possible (Djokic' *et al*., 2010).Two electrochemical reactions, reduction of metal ions and oxidation of a reducing agent, occur at the same active place on the electrode–electrolyte interface. The overall reaction is shown (Equation 2-1).

Equation 2-1

$$M^{z+}(solution) + Red\ (solution) = \ M^0\ (solid) + Ox\ (solution)$$

The catalytic surface can be the substrate itself or a surface coated with catalytic colloids. A reducing agent binds to the active planes and is oxidized so producing electrons to reduce metal ions to a zero-valent metallic state (Prestianni *et al*., 2014). Continuous reduction provides the generation of hydrogen that in turn promotes new catalytic sites for metal deposition. Therefore, the process is called autocatalytic electroless deposition (Prestianni et al., 2014).

2.4 Techniques used in nanoparticle characterization

A variety of characterization techniques are to identify the morphology chemical and physical properties that these new material possess. These techniques range from UV-Vis, HRTEM, ICP-AES, XRD, SEM, DLS, TGA and FT-IR and XPS.

2.4.1 Zeta potential measurements

This section will gives a general overview of the concept of the zeta potential (ZP).The two parameters that control the nature and behaviour of every system in which one phase is dispersed in another phase will be discussed. The phases are known as the disperse phase (for the phase forming the particles) and the dispersion medium (for the fluid in which the particles are distributed). The two parameters are the extent of the interface and the interfacial chemistry of the disperse phase. The physical nature of any dispersion depends on the respective roles of the constituent phases (Hunter, 2001).

The physico-mechanical and physicochemical characteristics that constitute the two respective fundamental parameters are summarized in (Table 2-1).

Table 2-1 The physico-mechanical and physicochemical characteristics that constitute the two perspectives fundamental parameters depend on.

Interfacial Extent	**Interfacial chemistry**
Particle Size and Distribution	Surface Charge
Particle Shape/Morphology	Nature/Type of Group(s)
Surface Area (External/Internal)	Number and Distribution
Porosity	Dissociation
	Preferential Adsorption
	Hydrophobic/Hydrophilic Balance
	Surface (Interfacial) Tension
	Contact Angle

All materials will naturally acquire a surface electrical charge when brought into contact with a polar medium (*i.e*. water). Generally an interface in deionized water is negatively charged, but there are materials that can be positively charged (Hunter, 2001).

The various charging mechanisms are:

- Electron affinity differences of two phases
- Ionization of surface groups
- Differential ion adsorption from electrolyte solution
- Differential ion dissolution from a crystal lattice
- Surface anisotropy
- Isomorphous substitution

The electrical double layer also plays a significant role in zeta potential analysis. A particle dispersed in a liquid is solvated and the extent of the solvated layer is influenced by the solution conditions such as composition (i.e., ionic strength), temperature and pressure. The boundary between the edge of this solvated layer and bulk liquid is termed the shear plane (Pons *et al*., 2006).

The electric double-layer (EDL) is established such that the particle surface charge is neutralized by an adjacent layer in solution containing an excess of ions of opposite charge to that of the surface, i.e., counter ions; ions of the same charge as the surface are termed co-ions (Smoluchowski 1917).

The EDL can be regarded as consisting of two regions or layers (hence the term electric double-layer; a region closest to the surface (the Stern layer) that is considered immobile (and it may include adsorbed ions) and an outer region (the diffuse layer) that allows diffusion of ions that are distributed according to the influence of electrical forces and random thermal motion (French *et al*., 2009) this is shown in (Figure 2-9).

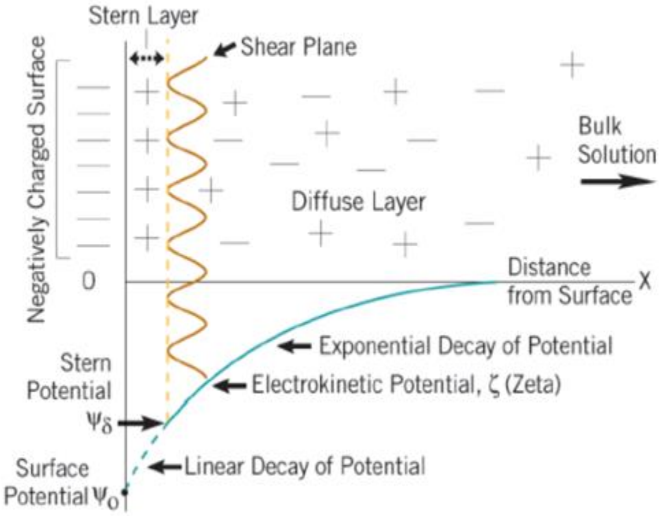

Figure 2-9 Simplified model of the electrical double-layer at a charged interface in an aqueous solution adapted from (Particle Sciences drug development services).

2.4.2 Dynamic light scattering (DLS)

Dynamic light scattering (DLS) is a physical method to determine the size and submicron particles by measuring their thermal motion (diffusion) in suspensions and emulsions (Brar and Verma, 2011). In particle size analysis and determination DLS has been established over many years for the characterization of sub-micron particles and macromolecules (Sapsford *et al.*, 2011). This technique is synonymous with Quasi-Elastic Light Scattering (QELS) and Photon Correlation Spectroscopy (PCS) but is not fully established and understood for (PCS) analysis. The measurement principle is based on a time-resolved measurement of the scattered light intensity from a sample cell that contains the particle system in a solvent (Pons *et al.*, 2011). Due to the changeable motion of the particles caused by non-compensated impacts of the solvent molecules caused by Brownian motion or diffusion, the intensity oscillates round an average value. The frequency of these fluctuations contains information about the diffusion coefficient of the particles, which is a size-dependent variable. The measurement principle requires that diffusion is the only cause of motion in the sample (Brar and Verma, 2011). The interpretation of DLS data has to be carried out with caution, since an unambiguous relationship between the measured diffusion coefficient and the particle size can only be found for dilute dispersions of spherical particles. Therefore there are restrictions regarding sample concentration and particle shape. In orthodox DLS high a sample with a high concentration is a major problem. If the scattered light from one particle encounters other particles before it is registered at the detector as so-called multiple scattering, the size information of the signal is lost. In the last few years commercially available instruments that suppress multiple scattering effects have been developed. Thus, the quantifiable concentration range is now remarkably extended (Mahdavi *et al*., 2013). It also serves another function of measuring the zeta-potential of a particle and measuring or estimating the molecular weight of organic compounds. The particle size is then determined from the translational diffusion coefficient by the use of the Stokes-Einstein equation, (Equation 2-2)

Equation 2-2

$$d(H) = \frac{kT}{3\pi\eta D}$$

2.4.3 X-ray diffraction

X-ray diffraction (XRD) is one of the most valuable non-destructive tools used to analyse a range of matter -ranging from fluids, to powders and crystals (Chauhan and Chauhan, 2014). From research to production and engineering, XRD is an in dispensable method for structural materials characterization and quality control which makes use of the Debye-Scherrer method. This technique uses X-ray diffraction on powder or microcrystalline samples, where ideally every possible crystalline orientation is represented equally (Chauhan and Chauhan, 2014). In the so called diffractogram the diffracted intensity is shown as function either of the scattering angle 2θ which makes it independent of the used X-ray wavelength. The diffractogram is like a unique "signature "of materials (Sharma *et al*., 2007). (Figure 2-10) demonstrates this claim.

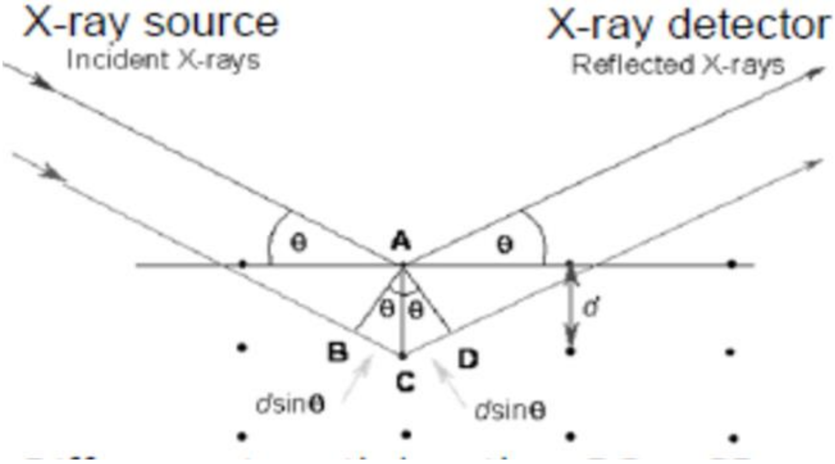

Figure 2-10 Graphical representation of a sample interacting with an X-ray source.

Difference in path length = BC + CD

BC = CD = $d_{hkl}\sin\Theta_{hkl}$

Difference in path length = 2 $d_{hkl}\sin\Theta_{hkl}$

Must be an integral number of wavelength, $n\lambda = 2\, d_{hkl}\sin\Theta_{hkl}$

(n = 1, 2, 3…)

English physicists Sir W.H. Bragg and his son Sir W.L. Bragg developed a relationship in 1913 to explain why the cleavage faces of crystals appear to reflect X-ray beams at certain angles of incidence (theta, Θ). The variable d is the distance between atomic layers in a crystal, and the variable lambda λ is the wavelength of the incident X-ray beam; n is an integer. This observation is an example of X-ray wave interference (Borchert et al., 2005).

This is explained by the Bragg (Equation 2-3).

Equation 2-3

$$\lambda = 2d_{hlk} \sin\theta_{hlk}$$

Although Bragg's law was used to explain the interference pattern of X-rays scattered by crystals, diffraction has been developed to study the structure of all states of matter with any beam, e.g., ions, electrons, neutrons, and protons, with a wavelength similar to the distance between the atomic or molecular structures of interest.

The size of the nanoparticles may be calculated from the powder XRD diffraction pattern using the Debye-Scherrer equation, (Equation 2-4) (Borchert et al., 2005).

Equation 2-4

$$d = \frac{k\lambda}{\beta \cos\theta}$$

Where: d is the size; k is the Scherrer constant (0.9); λ is the X-ray wavelength; β is the width of XRD peak at half height determined from the pattern; and θ is the Bragg diffraction angle (Mahdavi *et al*. 2013).

In X-Ray diffraction the broadness of the peak reveals valuable information about the sample and the size of a crystalline material is determined by measuring the broadness of the reflections in a diffraction pattern (Mahdavi *et al*. 2013). The broadening of the XRD is inversely proportional to the size of the crystalline particles, therefore, the more narrow the peak, the larger the crystallite size. Several factors affect the broadening (narrowness or wideness) of the peak such as the periodicity of the individual crystallite domains, reinforcing the diffraction of the X-ray beam (Mahdavi *et al.* 2013).

Advantages and applications of XRD include:

- XRD is a non-destructive technique.
- Used to identify crystalline phases and orientation.
- Used to determine structural properties: Lattice parameters (10-4Å), strain, grain size, expitaxy, phase composition, preferred orientation (Laue) order-disorder transformation, thermal expansion.

- Can be used measure thickness of thin films and multi-layers.
- Used to determine atomic arrangement.

Disadvantage include

- Detection limits: ~3% in a two phase mixture; can be ~0.1% with synchrotron radiation spatial.
- Resolution: normally none.

2.4.4 Fourier Transform Infra-Red (FT-IR) spectroscopy

The infrared spectrum is formed as a result of the absorption of electromagnetic radiation at frequencies that correlate to the vibration of specific sets of chemical bonds from within a molecule or compound. It is important to understand the distribution of energy possessed by a molecule at any given moment, defined as the sum of the contributing energy terms (Johal, 2011).

FT-IR spectroscopy is commonly used to obtain information about the capping agent of the NPs such as organic functional groups (e.g. carbonyls, hydroxyls) and biomolecule conjugation bound to NPs surfaces (Cantor and Schimmel, 1980). In recent years, attenuated total reflection (ATR–FT-IR) spectroscopy has been become prevalent. ATR–FT-IR employs the property of total internal reflection in combination with IR spectroscopy to examine the structure of the sample at a solid/air or solid/liquid interface (Hind et al., 2001). ATR–FT-IR provides IR spectra for the investigation of certain properties such as alterations in surface characteristics and identification of chemical properties (Johal, 2011; Kazarian and Chan, 2006; Liu and Webster, 2007).

2.4.5 X-ray photoelectron spectroscopy (XPS)

X-ray photoelectron spectroscopy (XPS) is based on the photoelectric effect. Each atom has core electron with the characteristic binding energy that is equal to the ionization energy of that electron. When an X-ray beam is directed to the sample surface, the energy of the X-ray photon is adsorbed completely by the core electron of an atom (Menard *et al*., 2006). If the photon energy, hv, is large enough, the core electron will then escape from the atom and emit out of the surface. The emitted electron with the kinetic energy of E_k is referred to as the photoelectron. The binding energy of the core electron is given by the Einstein relationship in (Equation 2-5).

Equation 2-5

$$hv = E_b + E_k + \varphi$$

Where hv is the X-ray photon energy (for Al Ka, hv =1486.6eV); Ek is the kinetic energy of photoelectron, which can be measured by the energy analyser, and φ is the work function induced by the analyser, about 4~5 eV.

Basic requirements for XPS measurement include:

- A source of fixed-energy radiation (an x-ray source for XPS or, typically, a He discharge lamp for UPS)
- An electron energy analyser which can disperse the emitted electrons according to their kinetic energy, and thereby measure the flux of emitted electrons of a particular energy
- High vacuum environment to enable the emitted photoelectrons to be analysed without interference from gas phase collisions
- Avoid contaminated active surfaces.
- To extend the lifetime of X-ray source and other electronic optics in the XPS system.

The sample area is illuminated by X-rays which results in the release of photoelectrons with wide range of energies and directions. The magnetic lens units focus the photoelectrons and collect the information from the emitted photoelectrons which are further transferred via a series of apertures to the analyser entrance slit. Within the hemispherical analyser (HSA), electrostatic fields are formed which allows the electrons to pass through to the detector slits to the detector revealing the sample data (Shem *et al.*, 2009). In (Figure 2-11) depicts the main components of an XPS system.

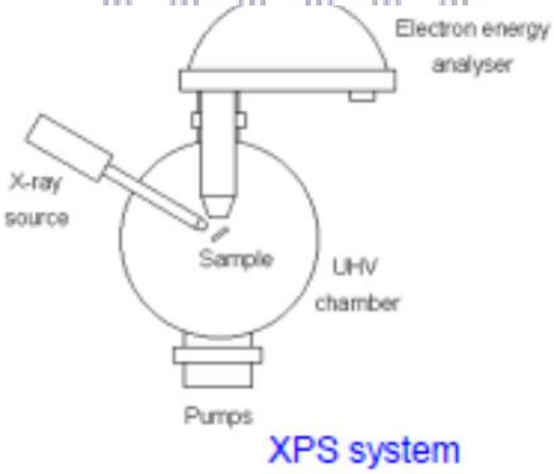

Figure 2-11 Schematic of a XPS system featuring main components (Shem et al., 2009).

In a recent study, using XPS was used on a dried Pd-plant material *arabidopsis* was conducted by (Parker *et al.*, 2014). They confirmed that the observed (metal nanoparticles) MNPs were indeed palladium deposits. The spectra showed two chemically distinct spin- orbit pairs in the Pd 3d levels, centred at 334.5 eV and 339.7 eV binding energies, these peaks were not present in the control plant material as shown in (Figure 2-12). The peak at 334.5 eV corresponds to fully reduced Pd(0) nanoparticles, whilst the second peak at 339.7 eV is due to unreduced $Pd^{(2+)}$ ions. Thus XPS shows the elements present, the oxidation state of the elements and indicate the energy of the photoelectrons only ejected from the first 3 Å of the material surface.

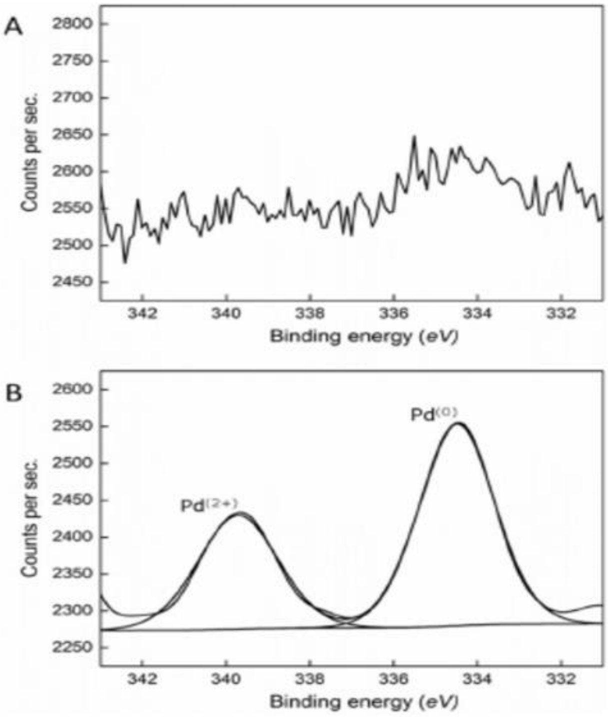

Figure 2-12 XPS spectra showing (top) un-dossed control plant, bottom plant dosed with palladium for 24 hrs (Parker et al., 2014).

2.4.6 Thermo-gravimetric analysis (TGA)

TGA is a thermal analysis technique which measures shifts in the physical or chemical properties of a sample with respect to time with uniform temperature and/or constant weight loss, temperature (with constant heating rate) and atmosphere. TGA reveals vital information about the physical properties of the material such as vaporization, adsorption, sublimation, absorption, vaporization, desorption and second order transitions (Coats and Redfern, 1963). It also gives information about the chemical properties of a sample such as that in solid-gas reactions (e.g. oxidation or reduction), decomposition, chemisorptions and desolvation (especially dehydration).

Thus, the basic instrumentation for TGA analyses are a weighing balance with pan loaded with the material, and a furnace which is programmable for certain temperatures and time. Furnace programming can be either for a uniform heating rate or that of heating to obtain constant weight loss over time (Tikhonov et al., 2009).

TGA has many applications in this part of the discussion one application is mentioned here is an ethyl cellulose sample, the experiment utilized gas switching and this was done on a TGA 4000. The sample gas purge rate was 30 mL/minute for nitrogen and air. The gas-switch from nitrogen to oxygen was triggered by a simple software command from within the sample method. The change in the Y axis percentage after the gas switch is the carbon content of this material this is shown in (Figure 2-13).

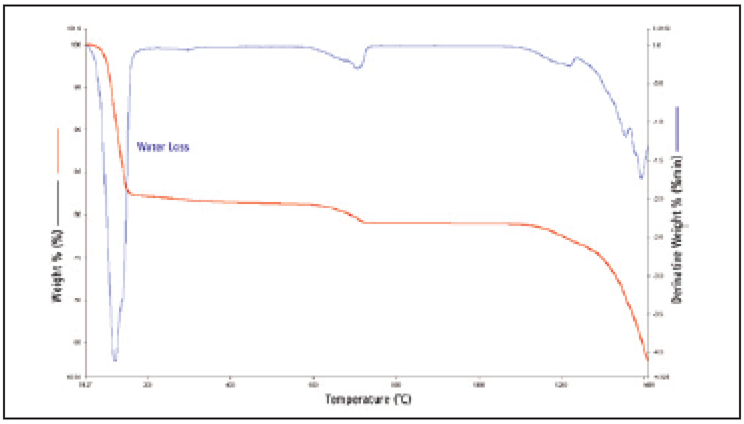

Figure 2-13 TGA of ethyl cellulose undergoing a temperature ramp with a gas purge rate of 30 ml/min using nitrogen gas (http://www.perkinelmer.com/product/tga-4000-system-100-240v-50-60hz-n5370210).

2.4.7 Electron microscopy

There was a need for new light source, in the 1920s it was discovered that accelerated electrons behave in vacuum just like light. Furthermore, it was found that electric and magnetic fields have the same effect on electrons as glass lenses. Dr. Ernst Ruska at the University of Berlin combined these characteristics and built the first transmission electron microscope in 1931 (Goldstein et al., 1992). For this work he was awarded the Nobel Prize for Physics in 1986 (Golding et al., 2016). The first electron microscope used two magnetic lenses and three years later he added a third lens and demonstrated a resolution of 100 nm, twice as good as that of the light microscope. Today the use of five magnetic lenses in the imaging system, a resolving power of 0.1 nm at magnifications of over 1 million times can be achieved (Golding *et al*., 2016; Galbraith and Galbraith 2011; Winey *et al*., 2013).

2.4.8 Transmission Electron Microscope (TEM)

The Transmission Electron Microscope (TEM) can be compared with a slide projector. Light from a light source is made into a parallel beam by the condenser lens; this passes through the slide (object) and is then focused as an enlarged image onto the screen by the objective lens. In the electron microscope, the light source is replaced by an electron source a tungsten filament heated in vacuum (Figure 2-14), the glass lenses are replaced by magnetic lenses and the projection screen is replaced by a fluorescent screen which emits light when struck by electrons (Ruska and Knoll, 1931). The whole trajectory from source to screen is under vacuum and the specimen has to be very thin to allow the electrons to penetrate it (Rosenauer et al., 2014; Guzzinati et al., 2015; Wang et al., 2000). Not all specimens can be made thin enough for the TEM. There is considerable interest in observing surfaces in more detail. Early attempts at producing images from the surface of a specimen involved mounting the specimen nearly parallel to the electron beam which then strikes the surface at a very small angle.

Only a very narrow region of the specimen appears in focus in the image and there is considerable distortion. The technique has not found wide application in the study of surfaces (Howe *et al*., 2008).

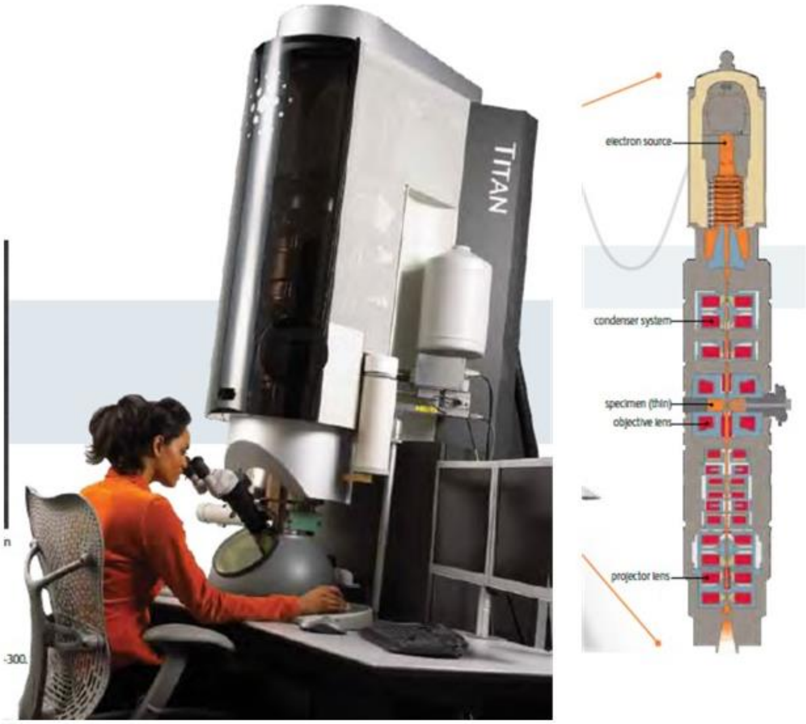

Figure 2-14 Left the Titan TM 80- 300 and right cross section of a column of a modern transmission electron microscope

The sample preparation process is the most important steps in TEM analysis especially when working with biological samples. Sample preparation involves three main steps, namely: chemical fixation, dehydration and finally embedding (Douglas and Tyla, 2010). Biological samples comprise have a high moisture content and thus, to be able to view it using TEM, the first step of preparation involves fixation, wherein the sample is fixed in such a way that the cell structure or tissue morphology is as close to the living material as possible (McDonald, 2009). This is then followed by dehydration step which comprises of washing using acetone or ethanol, then passed via a solvent such as propylene oxide and finally infiltrated and fixed in a liquid resin e.g. epoxy and White resin. The resin block is then thick sectioned in a process known an ultramicrotomy. In this process, thick sections of about 50-70 nm are collected on metal mesh 'grids' which are then stained with electron dense stains and therefore ready to view under EM (Sobol, 2010; Gidding, 2003; McDonald, 2009; Douglas and Tyla, 2010).

TEMs has a distinct advantage of being equipped with several detectors which includes backscattered, bright-field and dark-field STEM detectors. However these detectors are not only involved in imaging process, they also reveal chemical composition of the sample (Strasser *et al*., 2010). . The equipped detectors includes: EDX which is used for elemental identification of metal NPs and SAED which reveals the crystallography of the same sample (Strasser *et al*., 2010). TEM is a very useful instrument with a number of advantages as well as disadvantages as listed in (Table 2-2).

Table 2-2 Advantages and disadvantages of a Transmission Electron Microscope (TEM).

Advantages	**Disadvantages**
Produces high quality images	Potential interferences from sample preparation
TEM have high magnification levels	TEM is expensive piece of equipment
TEM has wide variety of applications	Takes up a lot of space due to multiple equipment working in tandem
With training fairly easy to operate	Sample should allow electron to penetrate and tolerate the vacuum chamber as well as have a snug fit
TEM provides insight into elemental composition and compound structure	Sample preparation is laborious
TEM provides information on morphological features of the material	Requires specialised facility and maintenance
	Special training required to operate equipment
	Images are presented as black and white

TEM and biological TEM to demonstrate the ease with which it is possible to distinguish nanoparticles as well as their morphology as shown in

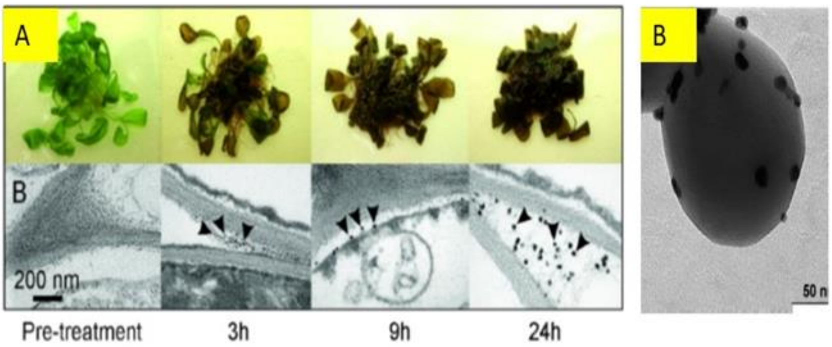

Figure 2-15 (A) Appearance of 3-week-old plants 24 h after treatment with K_2PdCl_4 and TEM showing accumulation over time of PdNPs in cell wall corners. (B) TEM image of Pd/TiO_2 (H_2O) (Parker, 2014).

2.4.9 Scanning Electron Microscopy (SEM)

These days SEMs can have a resolving power of 1 nm and can magnify over 400 000x (Hanada et al., 2008). The electron gun at the top of the column produces and electron beam which is focused into a fine spot less than 4 nm in diameter on the specimen (Goldstein et al., 1992). This beam is scanned in a rectangular raster over the specimen. Apart from other interactions at the specimen, secondary electrons are produced and these are detected by a suitable detector. The amplitude of the secondary electron signal varies with time according to the topography of the specimen surface (Goldstein et al., 1992). The signal is amplified and used to cause the brightness of the electron beam in a cathode ray tube (CRT) to vary in sympathy. Both the beam in the microscope and the one in the CRT are scanned at the same rate and there is a one to one relationship between each point on the CRT screen and a corresponding point on the specimen (Hanada *et al*., 2008). Thus a picture is built up Recording is done by photographing the monitor screen, making video images or storing a digital image. A SEM is usually equipped with two image monitors, one for observation by the operator and the other, a high resolution monitor, is equipped with an ordinary photo camera (which can be 35 mm or Polaroid). To facilitate the observation and correct choice of the parameters mentioned above, FEI SEMs have an image store in which the image is built up scan by scan and displayed at TV speed so that there is a steady, flicker-free image on the viewing monitor. Images are digital and can be stored electronically for subsequent enhancement and analysis (Liu *et al*., 2008).

The most distinct differences between TEM and SEM are:

•The beam is not static as in the TEM: with the aid of an electromagnetic field, produced by the scanning coils, the beam is scanned line by line over an extremely small area of the specimen’s surface.

•The accelerating voltages are much lower than in TEM because it is no longer necessary to penetrate the specimen; in a SEM they range from 200 to 30000 volts.

•Specimens need no complex preparation (Liu et al., 2008).

Figure 2-16 Left the JEOL 6700F High Resolution Scanning Electron Microscope adapted from http://www.matter.org.uk/tem/default.htm.

Table 2-3 Advantage and disadvantages of SEM (scanning electron microscope).

Advantages	**Disadvantages**
Reaches superior magnification limits (up to 1,000, 000x), with ultimate resolution of 1 nm.	SEMS are expensive and take up a large area and require specialized rooms free of electrical, magnetic or vibrational interferences.
Gives greater insight than just the surface topography.	Difficulty in Maintence such as keeping steady voltage to electromagnetic coils and a cooling system.
Digital data generated from sample as technological advances are made.	Interferences can result in sample preparation.
Specimen preparation time relatively short compared to TEM.	SEM are limited to solid and inorganic samples.
SEM is a non-destructive technique.	Minimal exposure of radiation with electrons scattering from sample surface.
Accommodates larger samples with diameters of above 200 mm.	Requires specialized training to operate and safety precautions must be in place.

2.4.10 Inductively coupled plasma - atomic emission spectroscopy (ICP-AES)

ICP-AES also known as inductively coupled plasma optical emission spectrometry (ICP-OES) is a spectroscopic technique used to quantify the elemental composition of nanomaterials, as well as detection of trace metals in simple and complex matrices (McClenathan *et al*., 2006)

ICP-AES functions on the basic principle of the use of high energy plasma from an inert gas such as Argon (Ar) which forms excited atoms and ions which release the electromagnetic wavelength properties of a specific sample by rapidly ashing the sample with flame temperature of about 6000 to 10000 K. The electromagnetic wavelength emission intensity of the sample of interest shows the concentration of the element present (Orbaek and Barron, 2014)

For ICP-AES, the sample must be digested in order to allow the atoms to be vaporized in the plasma consistently. Metal containing NPs are digested using a strong acid to bring atoms into the solution since failure to do this could hinder some metals being vaporized and the sample is not recorded accurately.

2.4.11 UV-Vis spectroscopy

UV-Vis spectroscopy is a commonly used technique which allows the estimation of a NP's size, concentration and aggregation level, particularly with AuNPs and AgNPs (Amendola and Meneghetti, 2009; Pal *et al*., 2007). Light wavelengths in the 200–800 nm range are generally used for characterizing various metal nanoparticles in the size range of 2–100 nm (Feldheim and Colby, 2002). Absorption measurements in the wavelength range of 400–450 nm are typically used to characterise AgNPs (Huang and Yang, 2004), while those between 500–550 nm are used for AuNPs (Shankar *et al*., 2004) due to the intense absorption attributed to the Surface Plasmon Resonance (SPR) bands of the AgNPs and AuNPs in these regions.

In another study using Solanum trilobatum leaf extract, the bioreduction of Pd ions in aqueous solution was monitored by periodic sampling of aliquots (0.2 ml) of the suspension, then diluting the samples with 2 ml deionized water and subsequently measuring UV-Vis spectra of the resulting diluents (Amarnath Kanchana1 *et al*., 2010). The UV-Vis spectra recorded from the aqueous palladium chloride-Solanum leaf broth reaction medium as a function of time of reaction (Figure 2-17). After completion of the reaction, the wavelength of the surface plasmon band stabilized at 270 nm, 240 nm and 200 nm for S-PdNP, S-PdNP-lipoic acid and S-PdNP-lipoic acid-vitamin, respectively (Amarnath Kanchana1 *et al*., 2010). The nanoparticle absorption band is slightly asymmetrical with indications of an additional weaker component at 370 nm. The presence of this shoulder indicates either formation of stable aggregates of the palladium nanoparticles in solution or shape anisotropy in the particles (Amarnath Kanchana1 *et al*., 2010).

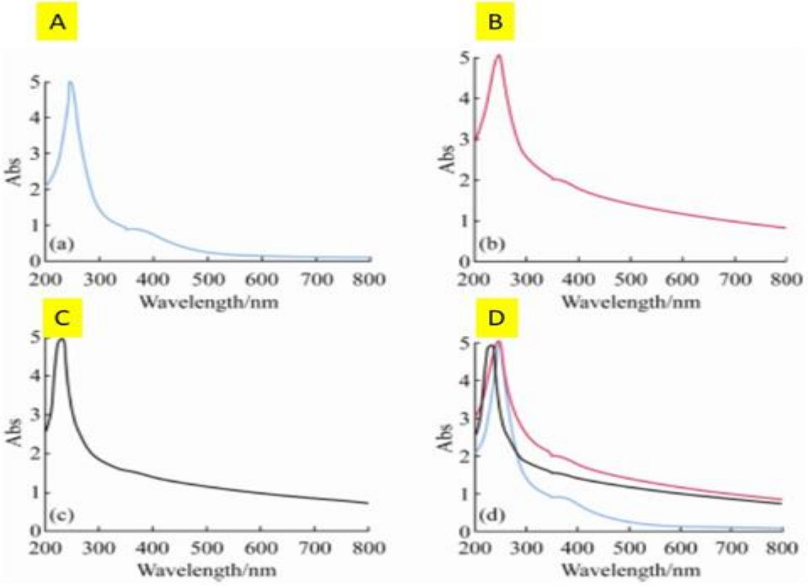

Figure 2-17 UV-Visible Spectroscopy image of palladium nanoparticles from Solanum trilobatum leaf extract. (a) Synthesis of palladium nanoparticles from Solanum trilobatum leaf extract;(b) Conjugate of lipoic acid in Solanum trilobatum palladium nanoparticles; Conjugation of vitamin along with lipoic acid in Solanum trilobatum palladium nanoparticles;(d) Combination of (a), (b) and (c) (Amarnath Kanchana1 *et al*., 2010).

2.5 *Ulva armoricana*

Algae are a heterogeneous group of plants. Due to their reduced content in lipids, elevated concentration in polysaccharides, natural richness in minerals, polyunsaturated fatty acids and vitamins as well as their content in bioactive molecules, marine algae are known to be a good source of healthy food (Scarano and Morelli, 2003). These algae have no roots, leaves or vascular systems; however they nourish themselves through the process of osmosis (Hayden et al., 2003). Two major types of algae that have been identified are the microalgae which are found in both benthic and littoral habitats and also throughout the ocean waters as phytoplankton and the macroalgae or seaweeds which occupy the littoral zone. Seaweeds grow in the intertidal as well as in the sub-tidal area up to a certain depth where very little photosynthetic light is available.

Seaweeds are classified into green algae (chlorophyta), brown algae (phaeophyta) and red algae (rhodophyta) on the basis of chemical composition. The color in case of green seaweeds is due to the presence of chlorophyll a and b in the same proportions as the ’higher’ plants; beta-carotene (a yellow pigment) and various characteristic xanthophylls (yellowish or brownish pigments) (Scarano and Morelli, 2003). Brown and red algae are marine only based, with some species of red algae being found in water depths where light levels are extremely low, while green algae is found in both marine and freshwater environments (Silva et al., 1996).

Several studies have revealed that seaweeds are a rich source of biologically active compounds such as carbohydrates, carotenoids, polysaccharides, proteins, vitamins, and numerous secondary metabolites. The studies have also shown the active compounds present in seaweeds have medicinal properties that can be used in conventional treatments and alternative therapies (Lobban and Harrison, 1997).

Studies have also shown seaweed extracts can have both anti-inflammatory and inhibitory properties that can be used to treat various medical conditions and suppress some forms of cancer. In addition, seaweeds are also capable of accumulating heavy metals and the secondary metabolites of several types of seaweed have anti-biological fouling properties. Moreover, recent studies have reported the biological reduction of metal ions in aqueous based seaweed solutions. These studies have confirmed that the various active compounds present in seaweeds can act as both metal reducing agents and capping agents during the formation of stable nanoparticles (Scarano and Morelli, 2003).

2.5.1 Scientific classification

Linnaeus in his Species Plantarum (1753) described the genus Ulva, together with three other algal genera namely Fucus, Conferva and Chara (van den Hoek et al., 1995). The Ulvaceae are morphologically simple ubiquitous algae (Silva et al., 1996). Ulva and Enteromorpha are the most commonly known members, probably because they are prevalent in coastal ecosystems and responsible for "green-tides", an event whereby dense blooms of free-floating algae form as a result of eutrophication (Adams, 1994; Blomster *et al*., 1998).

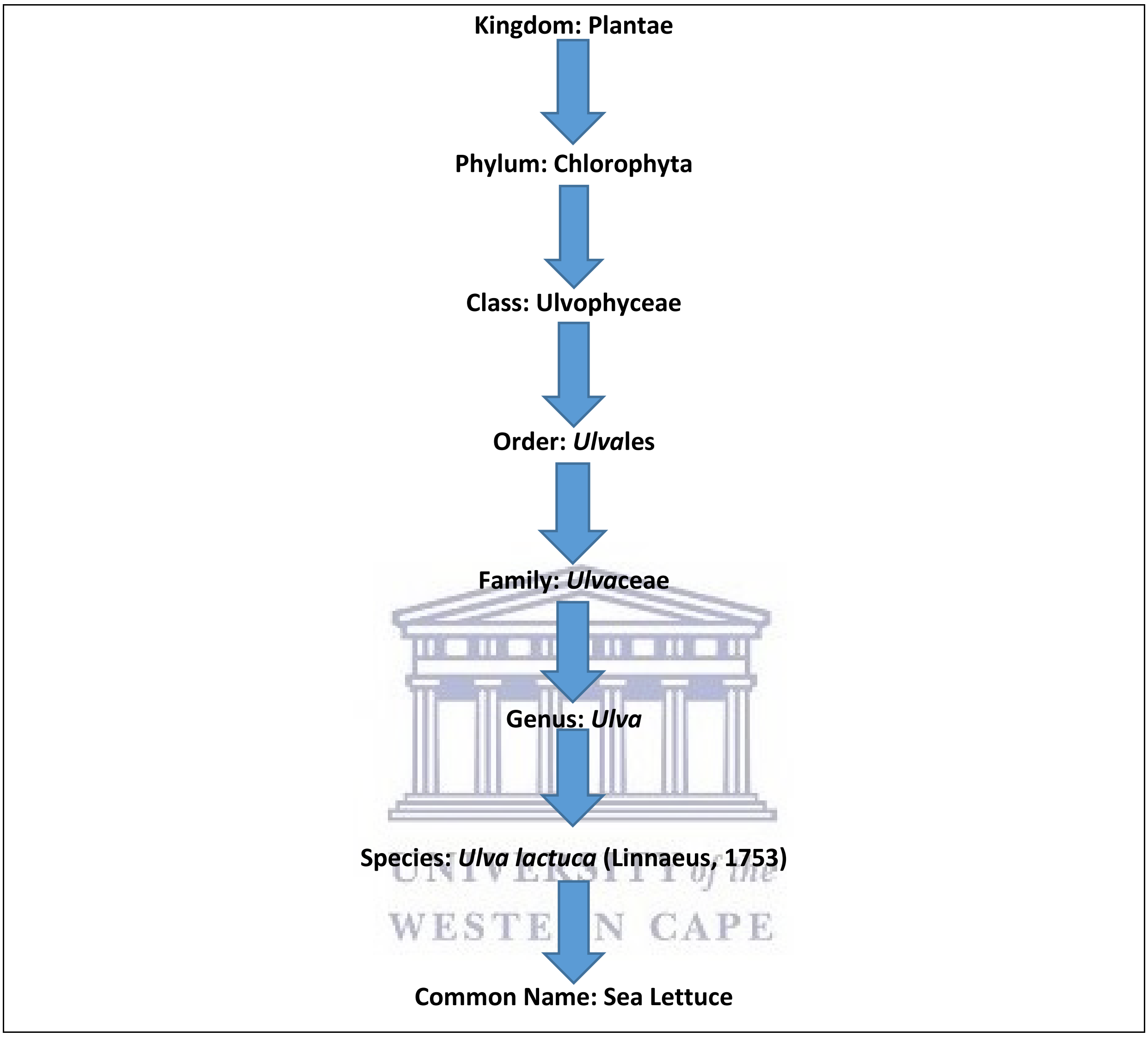

2.5.2 The Ulvaceae

The macroalgae in this family are known for their simple morphology, which enforces the difficulties encountered in their identification (van de Hoek et al., 1995). Included are all parenchymatous green seaweeds of varied morphology that are derived from uniseriate filaments by divisions of the cells in two or three planes (Beach et al., 1995) as shown in (Figure 2-19). *Ulva* is a member of a huge genus of marine and brackish green seaweed. Most importantly is a thin, flat green seaweed which grows to only 2 cell layers thick which means every cell is in contact with the external medium (Figure 2-18). A recent phylogenetic study based on nuclear and chloroplast DNA sequences, supported a monophyletic Ulvaceae consisting of *Chloropelta*, *Enteromorpha*, *Percursaria*, *Ulva* and *Ulvaria* (Lüning *et al*., 2008).

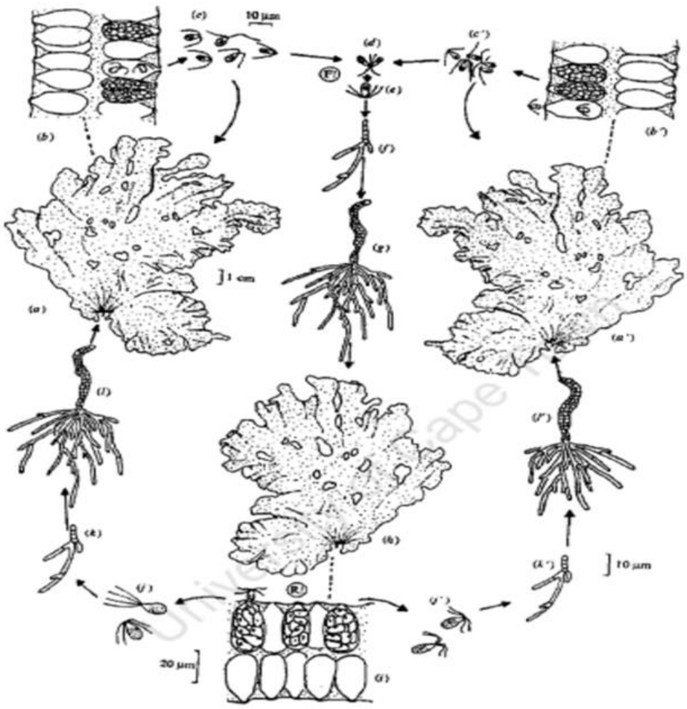

Figure 2-18 The life cycle of U. laetuea (Ulvaceae, *Ulvales*). (a, a') Flat blade-like gametophytes. (b, b'l Division of the cell contents into biflagellate gametes; these are unequal, copulation being anisogamous. (el Female gametes. (e') Male gametes. (d) Anisogamous copulation. (e) Quadriflagellate planozygote. (f) Uniseriate filamentous germling of sporophyte generation attached via branched rhizoids. (g) Tubular germling of sporophyte generation. (h) Fully developed blade like sporophyte (diploid). (i) Meiotic division of sporophyte cells to form haploid quadriflagellate zoids (meiospores). (J, j') Quadriflagellate meiospores. (k, k') Uniseriate filamentous germlings of the female and male gametophytes. (1, 1') Tubular germlings of the female and male gametophytes. F! = fertilization; R! = reduction division (meiosis). Source: Hoek et al. (1995).

Figure 2-19 Photograph of a whole plant of Ulva armoricana showing the typically crumpled texture. Specimen collected at the Ile Verte near Roscoff on 4 May 1995 (Dion *et al*., 1997).

2.5.3 The biogeographical distribution of Ulva

Factors such as the temperature regime of a habitat and temperature requirements for growth, reproduction and survival are known to determine the biogeographical distribution of marine organisms

(Bolton 1986; Breeman, 1988). The genus *Ulva* is well known for its wide distributions from marine to fresh water all over the world. Most of the species in the genus are found in near-shore marine and estuarine waters, upper to mid- intertidal (eulittoral and supralittoral zones), and in some locations may be found in the subtidal zones (Stegenga et al., 1997). *Ulva* species often form extensive mats in highly dynamic environments, one would often find rocks and boulders on the shore covered with layers and films of *Ulva* (Dickinson, 1963).

The records of *U. lactuca* Linnaeus, shows this species to have a wide distribution from Arctic, Ireland, Europe, Atlantic Islands, North America, Central America, South America, Africa, Indian Ocean Islands, Asia, South-east Asia, Australia and New Zealand, Pacific Islands, Antarctic and sub Antarctic (www.algaebase.org). Thus, Stegenga *et al*. (1997) suggested that most records are probably not correct and there is molecular evidence that South African *U. lactuca* is not genetically identical to the original European *U. lactuca* (Kandjengo, PhD unpublished data). In addition, currently three species of *Ulva* are being grown commercially in South Africa. At Irvin & Johnson (I & J) farm, one of the species is called *U. lactuca* is not likely to be *Ulva lacticia* one is called *U. rigida* but cannot be separated from *Ulva armoricana*, and the other species grown at Wild Coast abalone currently has no name (*sensu* Stegenga *et al*., 1997).

2.5.4 Uses of *Ulva*

Interest in seaweeds as novel food sources with potential nutritional benefits (Darcy-Vrillon, 1993), and animal fodder (Davies et al., 1997) is fast growing. This interest has led to the implementation and development of extensive mariculture systems for seaweeds in the ocean, ponds and also intensive land based systems using tanks (Lignell *et al*., 1987).

2.5.5 Ulva cultivation

Since the late 1990’s seaweed mariculture experiments were carried out using *Gracilaria* on an experimental sub-surface raft at Saldanha Bay (Anderson *et al*., 1996) based on the methods developed at Luderitz Bay, Namibia (Rotmann, 1987; Dawes, 1995). Recently, seaweed demand has increased with the rapid development of the South Africa abalone industry, since seaweed (harvested wild kelp) initially formed the primary diet of the farmed abalone and is still the main diet on many farms (Troell et al., 2006). Unfortunately, harvest of wild kelp for abalone feed is now approaching limits of sustainable harvesting in kelp concession areas where abalone farms are concentrated (Robertson-Andersson, 2007). Thus, in situ cultivation of seaweed on the farms is desirable in order to deal with growing requirements of feed, and this has led to the initiation of collaborative research projects on the mariculture of various seaweeds in South Africa (Troell *et al*., 2006).

More recently, according to Bolton *et al*. (2008), Wild Coast Abalone farm (at Haga Haga near East London on the southeast coast) has become a foremost leader in *Ulva* cultivation, and the current estimated figure of *Ulva* cultivation in South Africa is about 1,100 tonnes wet weight per annum. This farm grows most of the South Africa's *Ulva* and a main impetus for this culture was the lack of available kelp in the East London region (Bolton et al., 2008). In early 2006, an integrated abalone/*Ulva* system with partial re-circulation was set up at a farm on the southwest coast (Irvin & Johnson West Coast Abalone in Gansbaai). This system has been running commercially since January 2006 (Robertson-Andersson et al., 2008). Currently, the seaweeds cultivated on local abalone-seaweed farms are mainly *Ulva* species and at least four of different species are being cultivated (Bolton *et al*., 2008).

A study by Bolton *et al*. (2008) detailed the benefits and drawbacks of *Ulva* cultivation in South Africa. The local cultivation of *Ulva* has proven benificial so far, and the flow-through systems at Wild Coast Abalone (Haga Haga) farm produce about 2 t of *Ulva* per working day throughout the year, in a series of 32 large-scale ponds growing seaweed in effluent from the flow-through abalone tanks (Bolton *et al*., 2008).

2.5.6 Chemistry of Ulva

A study conducted by Yaich *et al*. (2011) to determine the chemical composition and functional properties of the dried *U. lactuca* seaweed collected from the shoreline between the Taboulba and Sayada area on the Tunisian coast. The soluble, insoluble and total dietary fibre content, mineral amount, amino acid and fatty acid profiles, swelling capacity (SWC), water holding capacity (WHC) and oil holding capacity (OHC) of the dried *Ulva* lactuca algae was investigated (Yaich et al., 2011). It was found that the *U. lactuca* powder contained a high fibre content (54.0%), minerals (19.6%), proteins (8.5%) and lipids (7.9%) (Yaich *et al*., 2011). The neutral fibres comprised of hemicellulose (20.6%), cellulose (9.0%) and lignin (1.7%), while the protein content analysis showed that it contains essential amino acids, which represent 42.0% of the total amino acids. During the fatty acids profile analysis, it was found that the most constituent fatty acids are palmitic acid (60%), followed by oleic acid (16.0%). Saritha *et al*. (2013) reported that *U. lactuca* has high protein content of 20.8% followed by carbohydrates with 13.2% then 4.4% lipid content (Saritha *et al*, 2013).

*Ulva*n (Figure 2-20) is the main water-soluble polysaccharide found in the cell wall of green seaweed of the order Ulvales (*Ulva* and Enteromorpha sp.). About 8–29% of the algae dry weight is represented by Ulvan (Robic *et al*., 2009), comprising sulfate, rhamnose, xylose, iduronic and glucuronic acids as major components (Lahaye and Ray, 1996; Percival and McDowell; 1967).

Ulvan has been shown to have a structure with greater complexity and variability with the polysaccharides containing repeating units (Lahaye and Robic, 2007). The two major repeating disaccharide sequences of *Ulva* are Ulvanobiouronic acid 3-sulfate composed of either glucuronic or iduronic acid. Furthermore, there are minor repeating units made up of sulfated xylose substituting the uronic acid or glucuronic acid as a branch on O_2 of the rhamnose-3-sulfate (Lahaye and Ray, 1996; Percival and McDowell, 1967; Lahaye *et al*., 1997).

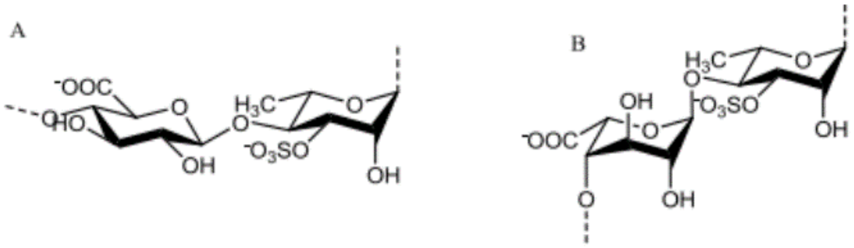

Figure 2-20 The main repeating disaccharide unit of Ulvan A. [→4)-β-D-Glcp-(1→4)-α-LRhap3S-(1→]n; B. [→4)-α-L-Idop-(1→4)-α-L-Rhap3S-(1→]n. (Jiao et al., 2011).

2.5.7 Bioactivity of compounds isolated from *Ulva*

Algae contains a high content of amino acids, terpenoids, phlorotannins, steroids, phenolic compounds, halogenated ketones and alkanes, cyclic polysulphides, fatty acids, acrylic acid (Mtolera and Semesi, 1996; Taskin et al., 2007), proteins, polysaccharides, vitamins, minerals and fibres (Lehaye, 1991; Darcy-Vrillon, 1993). Marine green algae have been reported several times to have the antibacterial (Lavanya and Veerapan, 2011), antiviral (Trono, 1999), antifungal (Oumaskour, 2012), anticoagulant (Yasantha, 2007), antitumor and anti-inflammatory (Scheuer, 1990) activities. Alginate, carrageenan and agar isolated from seaweeds have been used for medicinal and pharmaceutical purposes (Siddhanta *et al*., 1997).

Seaweeds are known to possess a variety of secondary metabolites. In a study carried out by Manchu *et al.* (2014) in investigating the phytochemicals of three *Ulva* species, glycosides, carbohydrates, steroids, terpenoids and phytosterols were detected in all three seaweeds. Moreover, the *Ulva lactuca* and *U. intestinalis* samples exhibited the presence of flavonoids, quinones and proteins. *U. intestinalis* was found to be the good resource for bioactive compounds than *U. lactuca* and *U. fasciata* (Manchu *et al*., 2014).

2.6 Suzuki carbon-carbon coupling reaction

2.6.1 Introduction

The development of transition metal-catalyzed cross-coupling reactions, which form carbon-carbon and carbon-heteroatom bonds, is perhaps one of the most important contributions to synthetic organic chemistry and organometallics over the last half-century (Hartwig *et al*., 2010). This broad class of Pd catalysed methods have become a vital tool in the synthesis of small and macromolecular architectures, which in turn are relevant and applied to medicinal chemistry, natural products chemistry, industrial-scale synthesis and materials science (Nicolaou *et al*., 2005). The mildness of the reaction conditions and tolerance thereof, is typically compatible with a variety of sensitive functional groups, and the regioselectivity is often superior to traditional methods for the formation of multiply-substituted arenes as these reactions typically have high yields (King *et al*., 2004).

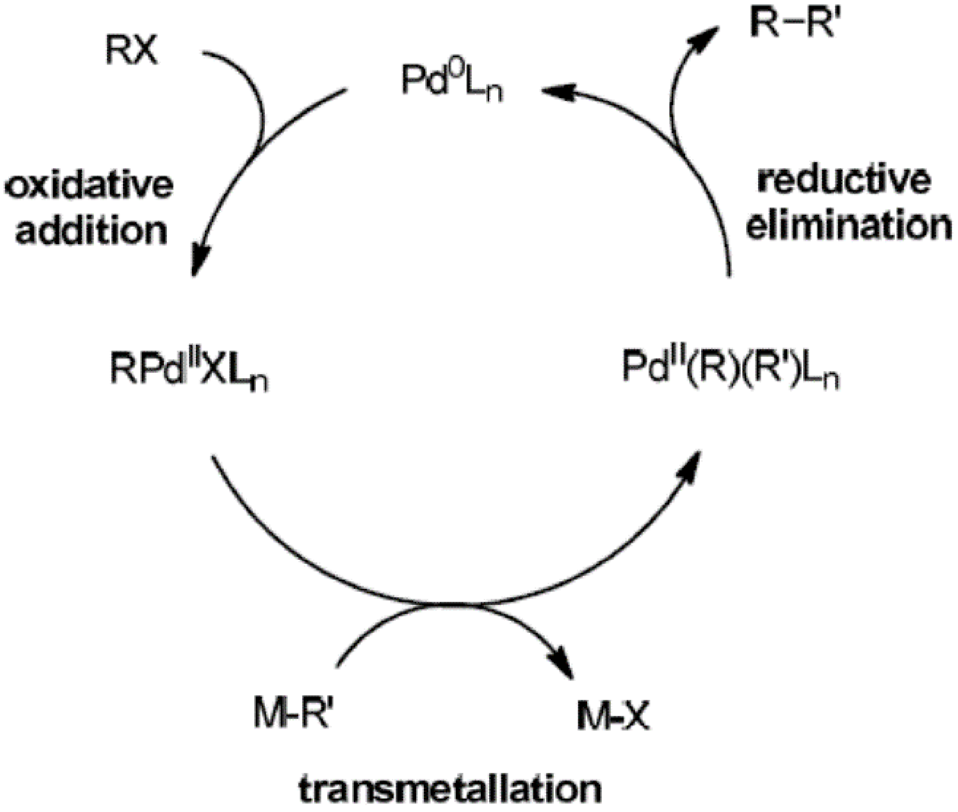

Figure 2-21 The general catalytic cycle of palladium-catalyzed cross-coupling reaction (Hartwig *et al*., 2010).

The general catalytic cycle of palladium-catalyzed cross-coupling has changed little since the seminal reports of these transformations as in (Figure 2-21). Catalysis takes place first by oxidative addition of a C-X bond (X = I, Br, Cl, OSO2R) to a palladium(0) complex, transmetallation transfers a second covalent ligand from an appropriate main group organometallic reagent, and C-C or C-X (X = N, O, S) bond-forms finally reductive elimination completes formation of the organic product and regenerates a Pd(0) intermediate (Amatore *et al*., 1999) The types of organometallic agents used in cross-coupling reactions are typically categorized by name reactions, including organo-tin, boron, silicon, zinc (also zirconium and aluminum), and magnesium compounds found in (Figure 2-22).

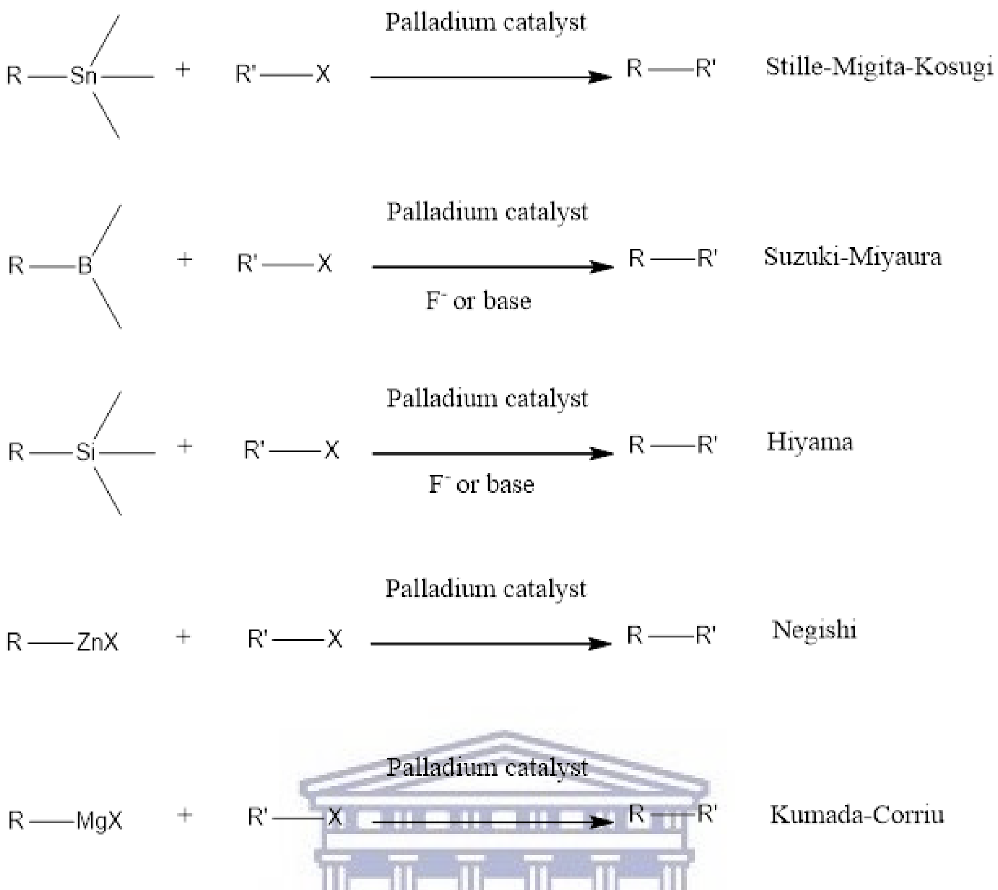

Figure 2-22 Named reaction of organometallic cross-coupling reactions (Littke *et al*., 2000).

Additionally, coupling reactions of haloarenes with olefins to form substituted alkenes (Mizoroki-Heck) or with terminal alkynes to form internal alkynes (Sonogashira) are typically associated with cross-coupling reactions as seen in (Figure 2-23). More recently, coupling reactions of electrophiles with heteroatom nucleophiles such as amines (Buchwald-Hartwig), alcohols, and thiols to form substituted amines, ethers, and sulphides have been developed (Bedford *et al*., 2004). These C-X bond-forming reactions are also commonly referred to as cross-coupling reactions because they share some mechanistic similarities to those of C-C bond-forming cross-coupling reactions (Negishi, 2003).

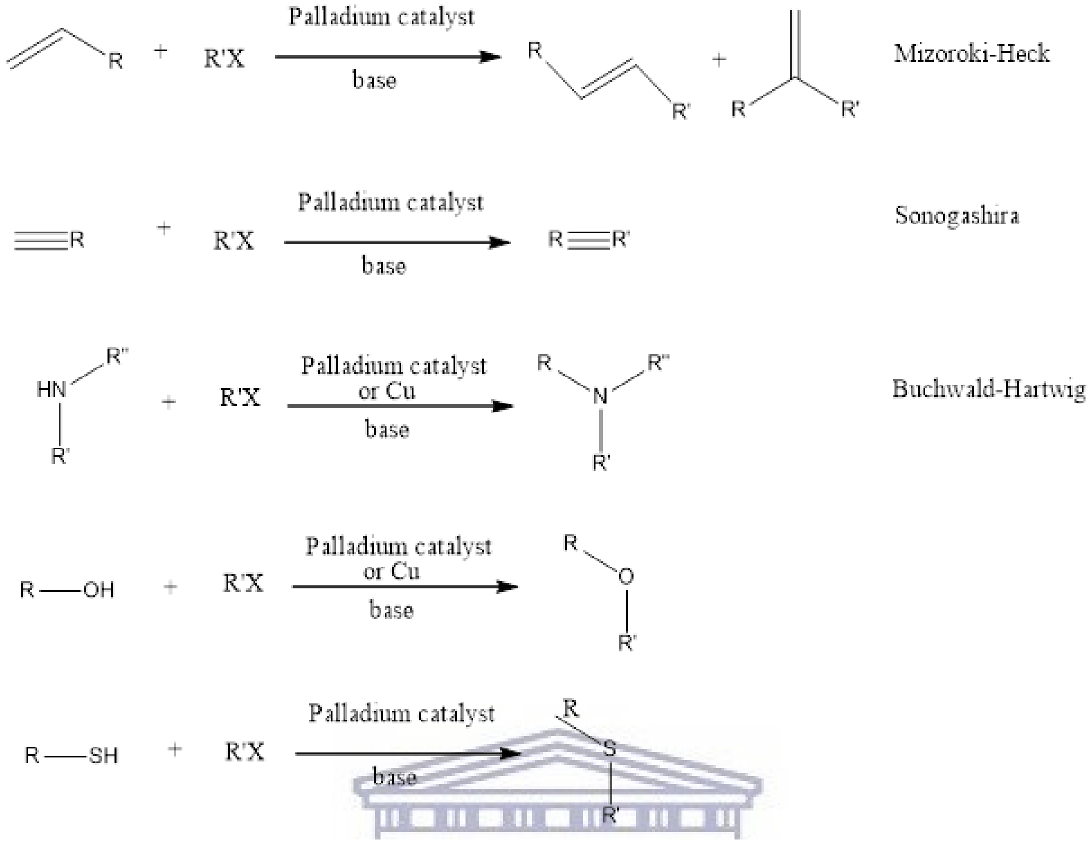

Figure 2-23 Additional coupling reactions of haloarenes with olefin forming substituted alkenes.

The structure of palladium catalysts for cross-coupling reactions has evolved together with the design of new ancillary ligands that afford enhanced catalytic activity. Most often these ancillary ligands are aryl- and alkyl phosphines, although N heterocyclic carbene (NHC) ligands are commonly used as well.

2.6.2 The Suzuki reaction

In 1981 the field of organic synthesis was changed when Suzuki and Miyaura *et al*. made a breakthrough in the methodology of biaryl compound synthesis by using aryl boronic acids and aryl bromide under homogeneous palladium catalyzed conditions in the presence of different bases (King *et al*., 2004) in (Figure 2-24).

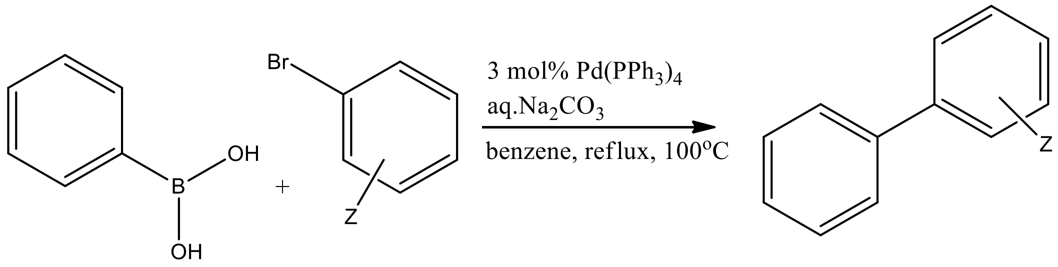

Figure 2-24 Reaction scheme for the synthesis of biaryl compound proposed by Suzuki and Miyaura (A. King et al., 2004).

This remarkable reaction, the "Suzuki-Miyaura Cross Coupling Reaction" is named after its inventors, and it is an extremely advantageous reaction, although many improvements have been made since its discovery (Miyaura, 2002). Under mild conditions, these reactions produce biaryl compounds with high selectivity and high yields.

Suzuki-Miyaura Cross Coupling reaction has been used in the pharmaceutical industry to produce Valsartan which has been used treatment for hypertension and heart failure by Novaratis and Borcalid a fungicide for food crops developed by BASAF as shown in (Figure 2-25).

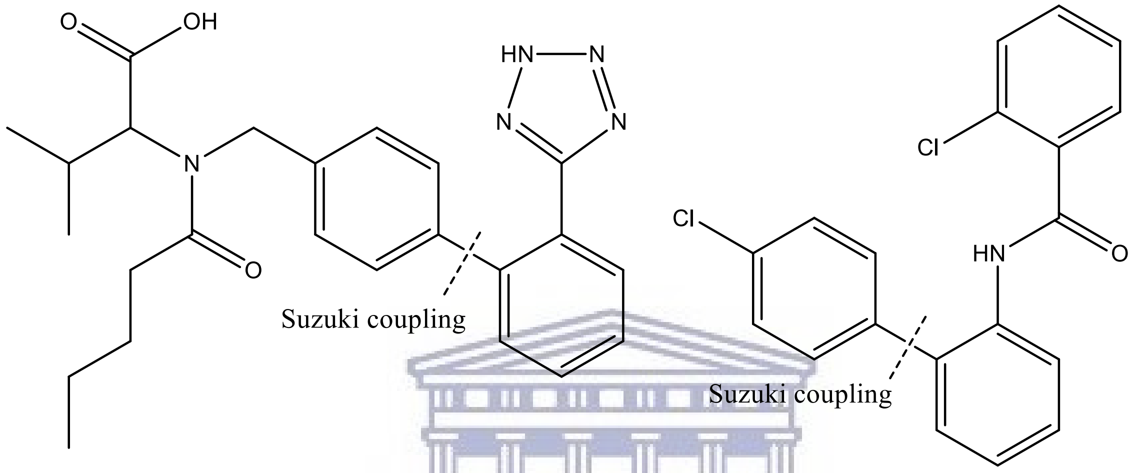

Valstran

Borcalid

Figure 2-25 Left Valstran by Novartis and on right Borcalid by BASAF.

Furthermore, there are few restrictions in terms of functional group requirements, thus making it possible for the synthesis of biaryls with diverse components such as hydroxy, carboxyl and formyl groups. It is possible to synthesize sterically-hindered pyridylphenol derivatives (Nicolaou *et al*., 2005) as shown in (Figure 2-26).

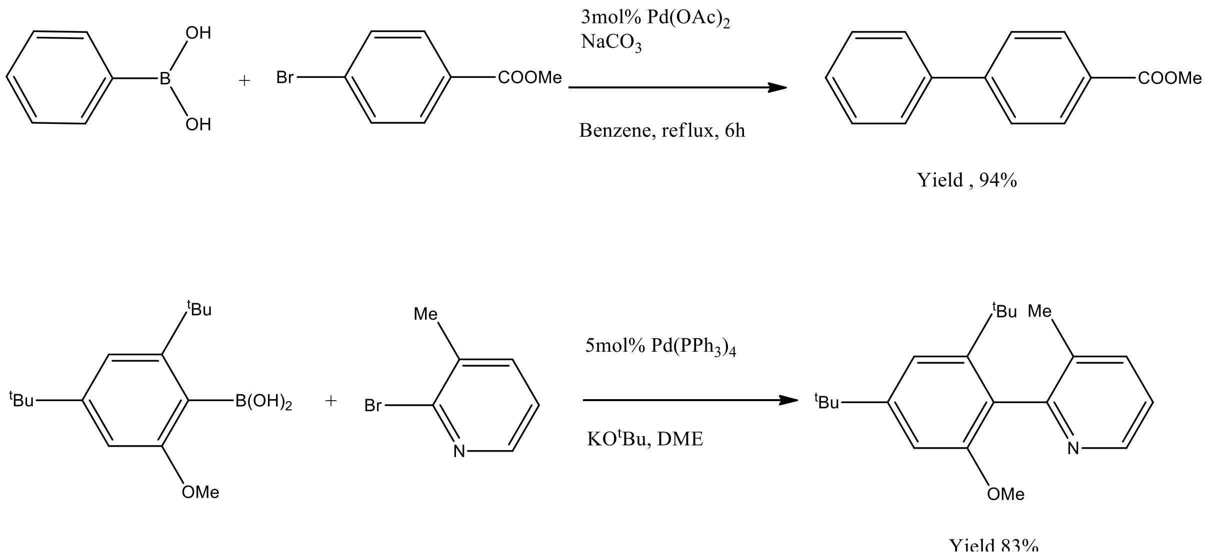

Figure 2-26 Example of synthesis of biaryls with diverse substituent components such as hydroxy, carboxyl and formyl groups and sterically-hindered pyridylphenol derivative (Nicolaou *et al*., 2005).

Recently many modifications have been made to the Suzuki-Miyaura Cross Coupling reaction, such as using water as a solvent, thus fulfilling a “green Chemistry's” perspective. For example, ArB $(OH)^{3-}$ $Bu4N^{+}$, generated is when tetrabutyl ammonium bromide and aryl boronic acid react in water, accelerates the cross-coupling reaction as shown in (Figure 2-27) reaction scheme cross coupling reactions using the water-soluble Pd(0) catalyst have also been reported (P Zhao *et al*., 2007).

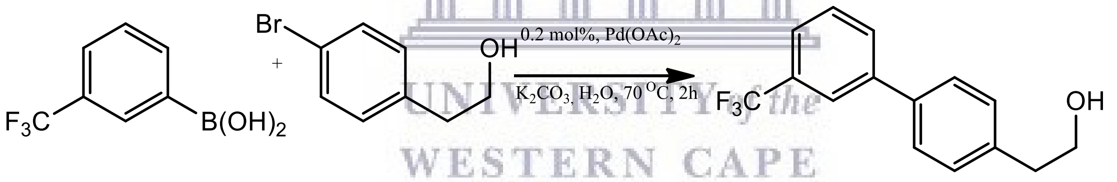

Figure 2-27 Modification of the Suzuki-Miyaura using water as a solvent.

Cross-Coupling reactions where the use of an amphiphilic polymer-supported Pd catalyst have also been reported as depicted in (Figure 2-28). This Pd catalyst forms a networked super molecular complex, which is insoluble in water and in organic solvents, and it is easily recovered from the reaction system. As Pd is firmly supported by the phosphino based groups of the copolymer, it does not elute during the reaction, and therefore it can be used repeatedly with high efficiency and yield (Chan *et al*., 2006).

Since the first report of the Suzuki-Miyaura cross coupling reaction, there have been many applications toward solid phase synthesis and other various syntheses. Aryl iodides and aryl bromides bound to Merrifield resin react with many different types of aryl boronic acids, and they produce biaryls in high yields (Miyaura and Suzuki., 1995) as shown in (Figure 2-28).

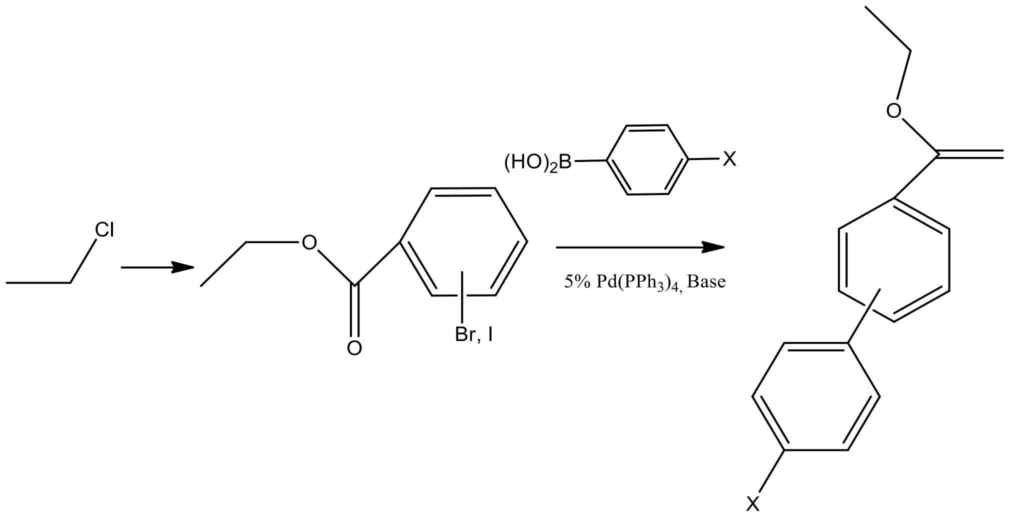

Figure 2-28 Suzuki-Miyaura cross-coupling reaction using amphiphilic polymers.

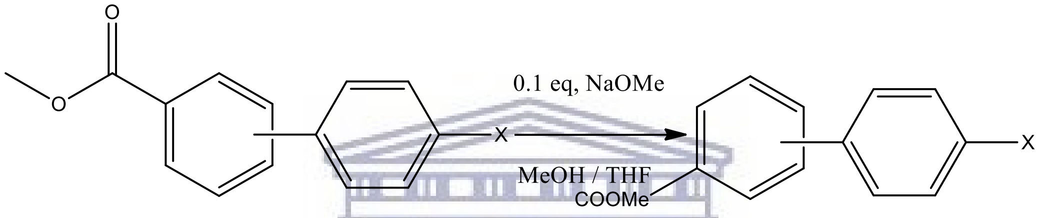

Figure 2-29 Reaction scheme of the use of aryl iodides and aryl bromides bound to Merrifield resin reacts with aryl boronic acids.

The reactivity's of aryl halides and aryl triflates are indicated as follows; Ar-I > Ar-Br > Ar-OTf >> Ar-Cl where the oxidative addition of aryl chloride upon Pd is a slow process. Therefore, in most cases it's been shown that the reaction itself does not proceed to completion, except in cases where aryls are heterocycles or possess electron-withdrawing groups as shown in (Figure 2-29)

In a recent publication by Parker *et al*. the authors reported on supported PdNPs synthesized by living plants as a catalyst for Suzuki-Miyaura reaction. There process eliminates the extraction process of the nanoparticle form the plant and hence decreases the production steps compared to that of the traditional preparation of palladium on carbon (Miyaura and Suzuki, 2002). These heterogeneous plant catalysts have demonstrated high catalytic activity in Suzuki coupling reactions between phenylboronic acid and a range of aryl halides containing iodo-, bromo- and chloro- moieties (Miyaura and Suzuki, 2002).

Wild-type Arabidopsis ecotypes were used to synthesize the PdNPs and the plants remained in a palladium solution (10 mM) for 24 hours. Samples were taken for TEM periodically for 24 hours, then remaining tissue was washed, dried and ground to a powder. Two catalysts were then prepared from the plant material, where the dried plant powder was pyrolised under N_2 and (300 ^{o}C) (Pd-P-300) and

(800 °C) (Pd-P-800) respectively.The Suzuki-Miyaura synthetic procedure employed by the authors is shown in (Figure 2-30)

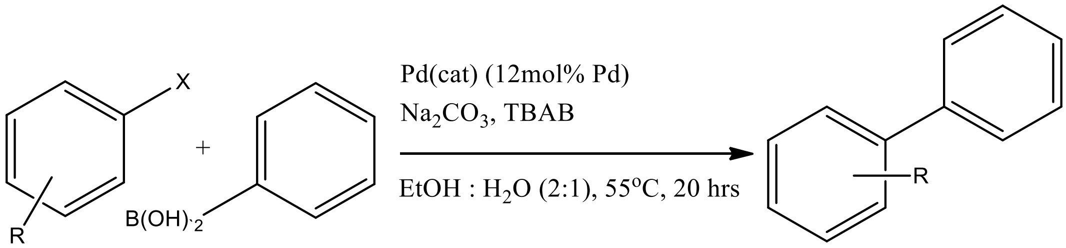

Figure 2-30 Reaction scheme used in the study of utilizing PdNPs supported on an Arabidopsis seaweed support as a catalyst in the Suzuki-Miyaura cross-coupling reaction (Parker et *al*., 2014)

These examples demonstrates that, the Suzuki-Miyaura Cross Coupling Reaction is by far one of the most powerful methods used in organic and organo-metallic for the formation of C-C bonds, but it is also an extremely useful procedure in the construction and synthesis of the carbon skeletons of many biologically important compounds (N. Miyaura and A Suzuki., 2002).

Chapter 3

3.1 Outline

The chapter reports the synthesis of PdNPs using the live marine seaweed *U. armoricana* and the characterization of the resultant NPs produced using various techniques such as UV-Vis, HRTEM, ICP-AES, XRD, SEM, DLS, TGA, FT-IR and zeta potential.

3.2 Introduction

The properties of NPs are different to those of bulk materials due to their small size and large surface to volume ratio. Among the nanoparticles, transition metal nanoparticles have received a large amount of attention as catalysts for a wide range of chemical reactions. Without a doubt, palladium is the most broadly used catalyst for the synthesis of fine chemicals in preparative chemistry and on an industrial scale, as both a homogeneous and heterogeneous catalyst due to its high reactivity and selectivity. Support of Pd on natural substrates has gained a lot of interest and has recently been reviewed. However, aggregation of naked Pd(0) nanoparticles is a very common problem due to the high reactivity of the NPs and the high surface/core atomic ratio. As a result, catalyst activity and selectivity is hindered and decreases as the aggregation increases. The use of capping agents can reduce or prevent aggregation, but such agents tend to reduce the reactivity of the surface, thereby reducing the catalytic activity of the stabilized nanoparticles, since the catalytic activity takes place on the surface. Thus new alternative methods are a needed naturally occurring capping agents found in marine seaweed and algae known as green nanotechnology. Supported palladium nanoparticles have recently been studied as catalysts for a range of reactions such as the catalytic hydrogenolysis of C-OH bonds, Suzuki−Miyaura and Mizoroki−Heck cross-coupling reactions. The commonly used synthetic methods for the preparation of metal nanoparticles include thermal decomposition or chemical reduction.

To maximize the sustainability of green nanoparticle production, the following points are considered during the synthesis of the nanoparticles:

- A renewable or easily recyclable reducing agent.
- A renewable material for the stabilization of the nanoparticles.
- An environmentally benign reaction medium.
- Minimization of energy consumption.
- Ease of nanoparticle recovery after synthesis should also be taken into account.

Combining these elements, “green” and eco-friendly methods are developed to ultimately produce eco-friendly nanoparticles. Biomaterials that have been used to synthesize NPs include marine algae which is listed in (Table 3-1), (Asmathunisha and Kathiresan, 2013; Singaravelu *et al*., 2007) and whole plants (Makarov *et al*., 2014). However, there seems to be only one report in the literature in the use of live marine algae in the synthesis of AuNPs (Mukhoro *et al*., 2017).

Table 3-1 Biomaterials which have been used to synthesis NPs including marine alga.

NPs produced	**Size (nm) & shape**	**Marine algal extract and alga**
Ag	3 to 44, spherical and cubic	Codium capitatum
Ag	30, spherical	*Spirogyra insignis*
Ag	5 to 35, spherical	*Padina tetrastromatica*
Au	8 to 15, spherical	*Sargassum wightii* Greville
Au	6 to 10, spherical and triangular	*Turbinaria conoides*
Au	18.7 to 93.7, spherical	*Stoechospermum marginatum*
Pd	2 to 15, spherical	*Chlorella vulgaris*
Pd	4 to 6, spherical	*Laminaria digitata*

3.3 Methodology

3.3.1 Collection of seaweed

The green seaweed and sea water were collected from the Marine Research Aquarium at Sea Point in Cape Town and identified as *Ulva armoricana* by Prof John Bolton from the department of Biological Sciences at the University Of Cape Town, South Africa. Collected *U. armoricana* samples were washed with distilled water and suspended in a fish tank filled with seawater and equipped with a fish tank pump to keep the organisms alive.

3.3.2 Materials

Potassium tetrachloropalladate (K_2PdCl_4) was purchased and used as received from Sigma Aldrich.

3.3.3 Equipment

3.3.3.1 UV-Vis spectroscopy

The reaction using the live *Ulva* organism steeped in a potassium tetrachloropalladate solution was measured optically by adding 3 mL of the into a 1cm path length UV quartz cuvette and subsequently measured using an Agilent Cary 60 UV-Vis Spectrophotometer (Agilent Technologies, USA) in the wavelength range of 190 nm to 800 nm.

3.3.3.2 Zeta-potential measurements

The stability and the size of the PdNPs was determined by using a Malvern Zetasizer using the Zetasizer software.

3.3.3.3 Inductively Coupled Plasma - Atomic Emission Spectroscopy (ICP-AES)

The determination of the percentage of Pd on the *Ulva* was accomplished through the use of a Thermo ICap 6200 ICP-AES. The instrument was calibrated and validated using NIST (National Institute of Standards and Technology, Gaithersburg MD, USA) traceable standards in order to quantify the palladium in solution.

3.3.3.4 Transmission electron microscopy (HR-TEM)

The size, shape, crystallinity and elemental composition of the PdNPs produced in the solution in which the *Ulva* were steeped were determined using HR-TEM coupled with EDX detectors. The HRTEM images, EDX data and patterns were obtained using an HRTEM Tecnai F20 with a field-emission gun (FEG) operating in bright field mode at 200 kV. The PdNPs samples were prepared by drying a single drop of undiluted solution on a lacy carbon mesh on top of a copper grid and dried under electric bulb. A drop of PdNPs was placed on the carbon-coated copper grid, making a thin film of sample on the grid which was allowed to dry. The ImageJ software was used to measure the NP size in the TEM images. Prior to the steps the sample was dissolved in 3 ml of ethanol.

3.3.3.5 X-ray powder diffraction (XRD)

The XRD patterns for the lyophilized samples of the powdered *Ulva* were acquired on a Bruker AXS (Germany) D8 Advance diffractometer (voltage 40 kV; current 40 mA). The XRD spectra were recorded in the range 2ϴ 30-90º using a CuKα (λ = 0.154nm) monochromatic radiation X-ray source. The size of the NPs was calculated using the Debye-Scherrer equation.

3.3.3.6 FT-IR spectroscopy

IR spectra of the air-dried and ashed, powdered samples were recorded on a Perkin Elmer Spectrum 400 FT-IR/FT-NIR spectrophotometer equipped with an ATR accessory using the Spectrum software.

3.3.3.7 Thermal Analysis

Thermogravimetric analyses of the furnace-dried, powdered PdNPs supported on *Ulva armoricana* were carried out using a TGA Analyser 4000 (Perkin Elmer) under a nitrogen atmosphere in the temperature range of 50 – 900 ºC at a rate of 10 ºC/min.

3.3.3.8 NMR spectroscopy

NMR spectra (1D and 2D) were acquired on a Bruker 400 MHz Avance IIIHD Nanobay spectrometer equipped with a 5 mm BBO probe at 333K using standard 1D and 2D NMR pulse sequences. All spectra were referenced to residual undeuterated solvent peaks.

3.3.3.9 Inductively Coupled Plasma - Atomic Emission Spectroscopy (ICP-AES)

In order to determine the percentage Pd loading on the *Ulva* support, the samples were prepared for ICP-AES as follows ~45mg of the *Ulva* supported PdNPs was subjected to digestion in nitric acid at 60 ^{o}C. The sample was then diluted to 50ml using distilled water.

3.4 Synthesis of PdNPs using live *Ulva armoricana*

In a typical synthetic process, the palladium nanoparticles were produced by steeping the live *Ulva armoricana* (1g) in a solution of K_2PdCl_4 for 2 days in a conical flask. Two concentration were used in the formation of the PdNPs namely 0.25 mM and 0.5 mM solutions of Pd complex. The seaweed was then air dried in a fume hood and finally subjected to calcination at a heating rate of 300 ^{o}C at 1^{o}/min. The formation of the PdNPs was also monitored using a Cary 60 UV-Vis spectrophotometer (Agilent Technologies) by observing the take up of the Pd by the *Ulva*. Where dry samples were required (e.g. for FT-IR, TGA and XRD analysis), the *Ulva* seaweed were allowed to dry in the fume hood at room temperature this is graphically illustrated in (Figure 3-1).

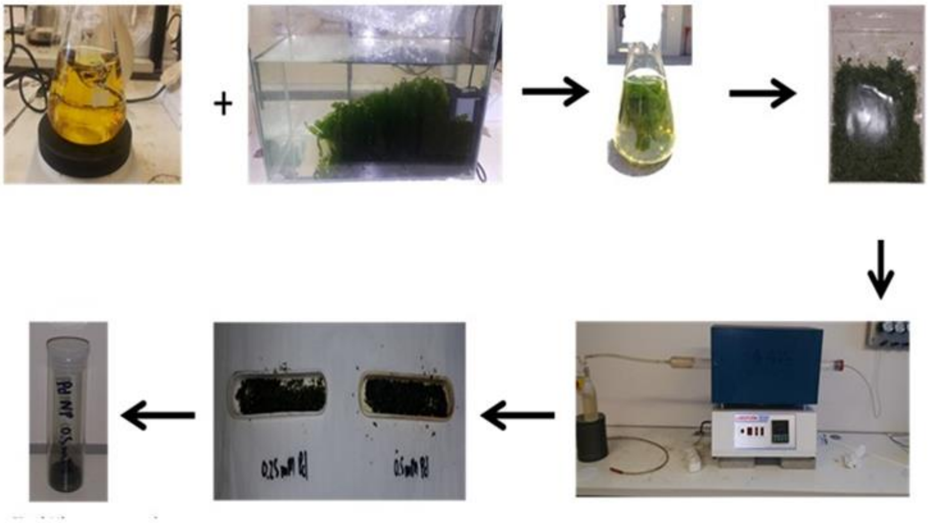

Figure 3-1 Graphic representation of the synthesis of PdNPs supporter on Ulva armoricana.

UV-Vis spectroscopic measurements were performed over the wavelength range of 190 nm to 800 nm by adding 1 mL of the solution that was steeped with the *Ulva armoricana* and diluting this volume in 17 ml MilliQ water and adding it to a quartz cuvette. The steeping process was allowed to proceed for 2 days and the absorbance measured every 5 mins for 1 hour and then every 20 mins for another hour, and then readings every hour for 8 hours. This data was collected and used to indirectly determine the rate at which the PdNPs were formed.

3.5 Results and discussion

3.5.1 UV-Vis spectroscopy

Preparation of the PdNPs resulted in a colour change from the bright yellow K_2PdCl_4 (Pd (II)) solution to a less intense yellow and later a brown solution as seen in the **(Figure 3-2)**. This colour difference initially could be explained by the ability of the seaweed to absorb metals that are in solution. Unfortunately there is no definitive visual observation such as a major colour change that can be possible evidence for PdNPs (such as the pink colour associated with production of AuNPs) formation at this stage. Evidence of nanoparticle formation was later established using XRD, UV-Vis and TEM analysis.

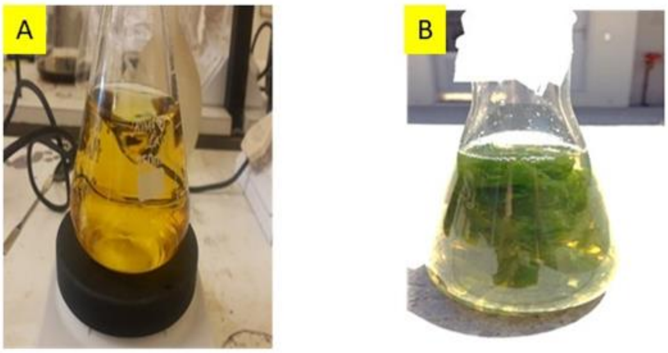

Figure 3-2 Colour change resulting in the change of a K_2PdCl_4 solution when steeped in 1g of *Ulva armoricana* (A) K_2PdCl_4 solution with no palladium, (B) *Ulva armoricana* with K_2PdCl_4 (0.5 mM) solution.

To provide a better understanding of the PdNP formation process, a baseline absorption for the K_2PdCl_4 solution was first established which is shown in (Figure 3-3).Absorption bands for the Pd salt are observed at ~242 nm and 207 nm in (Figure 3-3). Literature shows that the UV-Vis spectrum of a fresh K_2PdCl_4 solution shows absorption maxima at 310 nm and 420 nm that are typical of ligand-to-metal charge transfer bands of $[PdCl_3H_2O]^-$ in water (Rasmussen *et al*., 1968). For the time dependant studies 1 ml of the Pd solution with the steeped *Ulva armoricana* was steeped and the reading was taken up to 6 hours since a plateau was reached at a 4 hours as shown in (
Figure 3-4).

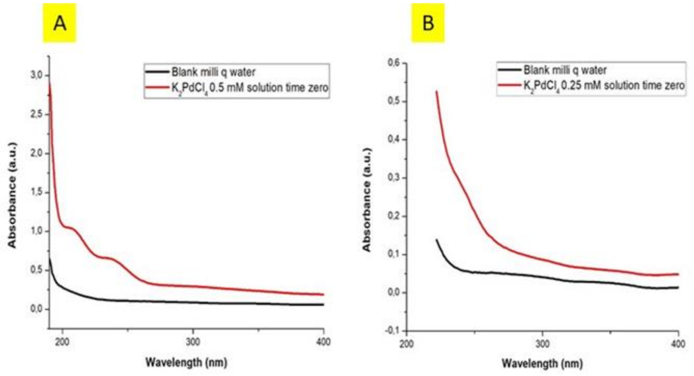

Figure 3-3 UV-Vis spectrum of blank MilliQ water and 0.5mM K_2PdCl_4 solution. (B) UV-Vis spectrum of blank MilliQ water and 0.25mM K_2PdCl_4 solution.

Figure 3-4) and (Figure 3-5) it is evident that the absorbance peak at 242 nm decreases in intensity. This reduction in this peak occurs within 5 mins of starting the reaction with the Pd(II) salt and live Ulva. The absorbance peak at 207 nm increases in intensity with time which may be due to the reduction of the Pd(II) salt to Pd(0) as seen in (Figure 3 4).There is only a shift to a higher wavelength for the reference peak evident at 242 nm from 0.25 mM and 0.5 mM.

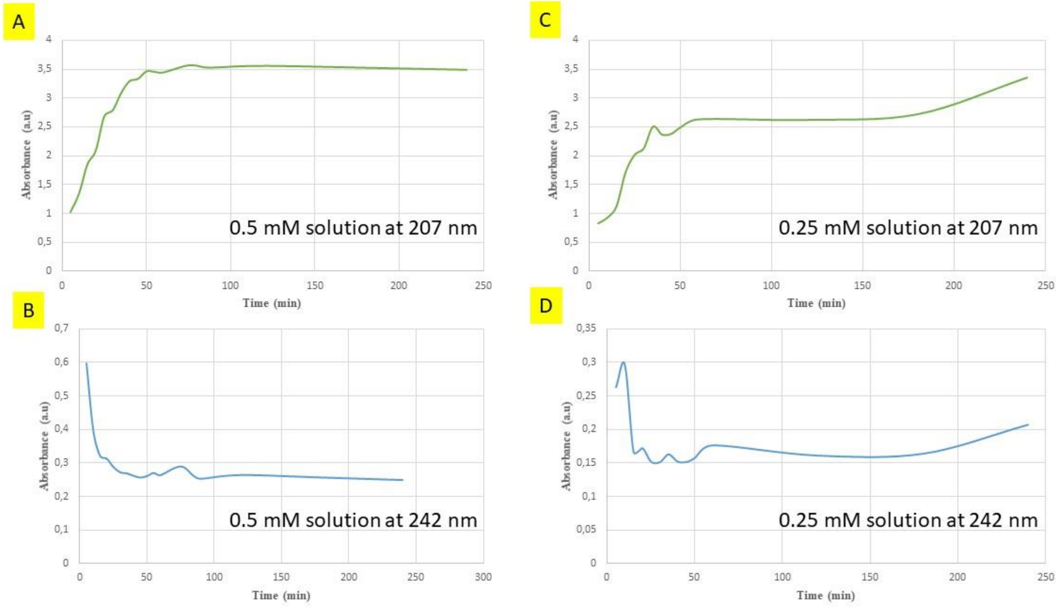

Figure 3-4 Change in the absorbance with respect to time of Pd^{2+} peaks 207 nm and 242. ((A) 0.5 mM at 207 nm, (B) 0.5 mM at 242 nm, (C) 0.25 mM at 207 nm, (D) 0.5 mM at 242 nm).

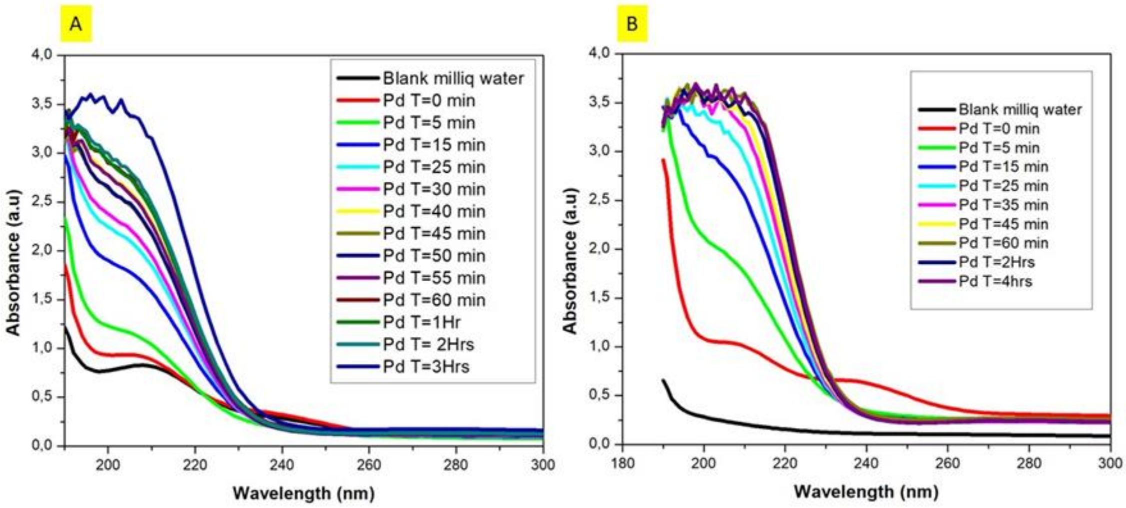

Figure 3-5 Absorbance of (A) 0.25 mM and (B) 0.5 mM K_2PdCl_4 measured over 3 hours.

3.5.2 HR-TEM and EDX analysis

HR-TEM analyses provided some insight into the morphology and sizes of the PdNPs synthesized using live *Ulva armoricana*, which were subsequently ashed at 300 ^{o}C at 1 ^{o}C/min. It is important to mention that the 0.5 mM Pd solution containing the live *Ulva armoricana* was chosen as this showed promising results in trial experiments for use in the Suzuki coupling reactions.

An *Ulva armoricana* sample containing no Pd was also ashed which was ashed at 300 ^{o}C at 1^{o}/min and subjected to HR-TEM analysis. We can conclude the *Ulva* sample has zero trace of palladium nano particle. Another characteristic feature is the evident nuclei that can be seen in (Figure 3-6).

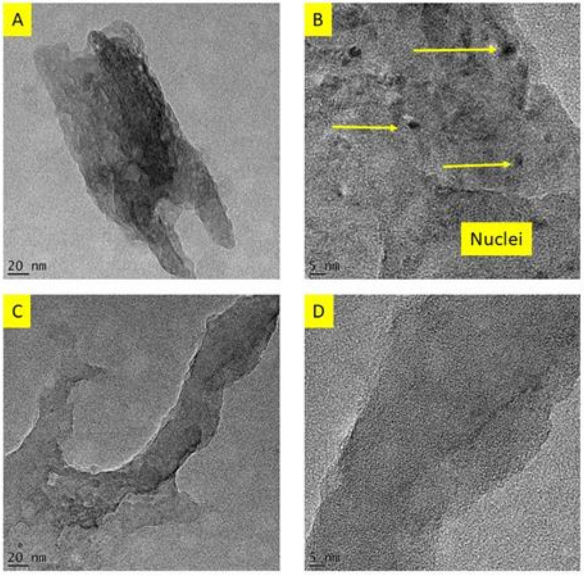

Figure 3-6 TEM images of *Ulva armoricana* with no palladium present at different magnifications. (A) TEM image of ashed *Ulva armoricana* with no PdNPs at 20 nm. (B) TEM image of *Ulva armoricana* with no palladium with nuclei as indicate with arrow. (C) TEM image of ashed Ulva armoricana with no PdNPs at 20 nm. (D) TEM image of ashed *Ulva armoricana* with no PdNPs at 5 nm.

The EDX spectra (Figure 3-7) obtained showed intensity peaks pertaining to copper and is expected as the sample being drop coated onto the copper grids used for TEM analyses. Trace amounts of magnesium, silica and potassium were also found these could be attributed as components of sea salts. The Ulva sample alone had no trace of palladium as expected. Trace oxygen could be attributed to adsorbed oxygen present on the sample surface.

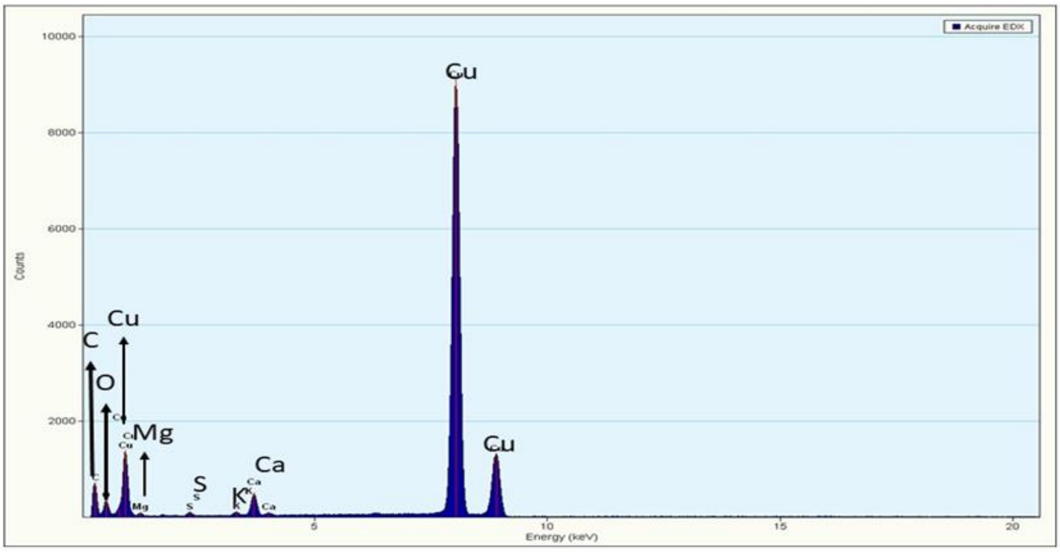

Figure 3-7 EDX spectra ashed Ulva armoricana with no palladium in sample.

TEM images as seen in (Figure 3-8) of the Ulva supported PdNPs confirmed the success of PdNPs synthesised using the 0.5 mM solution. The morphology was easy to distinguish and the NPs were found to be spherical.

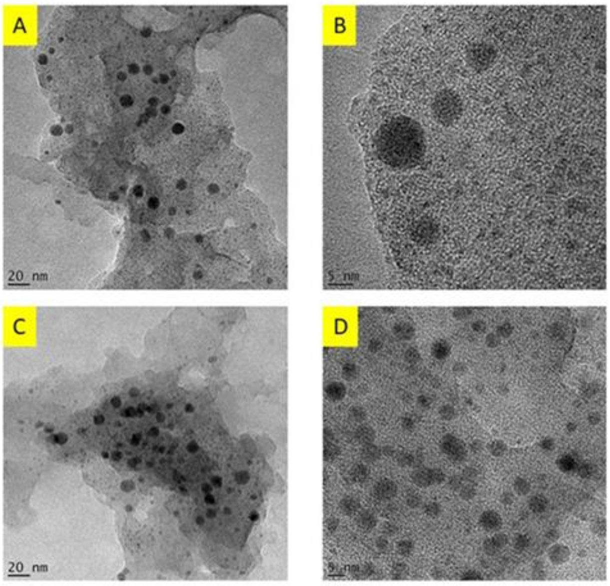

Figure 3-8 TEM images of ashed *Ulva armoricana* with PdNPs at different magnifications. (A) 20 nm, (B) 5 nm, (C) 20 nm, (D) 5 nm.

The EDX spectra obtained (Figure 3-9) showed the presence of PdNPs as determined from the TEM data. The PdNPs were measured to be 7 nm on average using the ImageJ software. The mean, minimum, max and standard deviation is given for the particle data size (Figure 3-10). The shape is characterized as regular spherical particles, once again showed the presence of copper and trace amounts of magnesium, silica, sulfur, chlorine and potassium which was attributed to the copper grid and perhaps residual salt from the reaction.

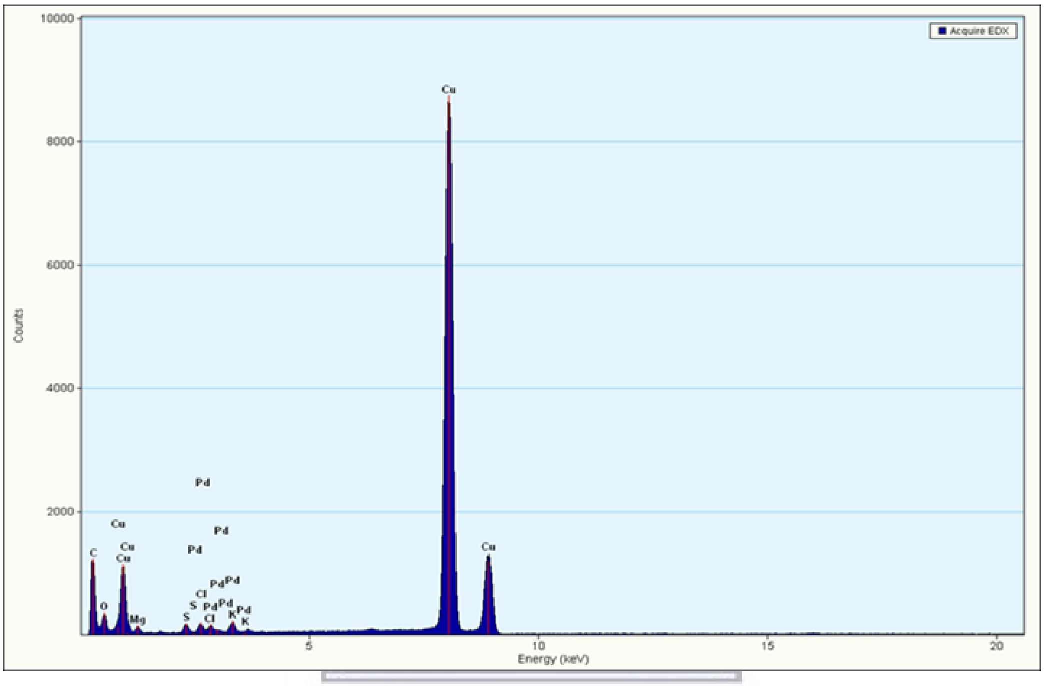

Figure 3-9 EDX spectrum of *Ulva armoricana* with palladium.

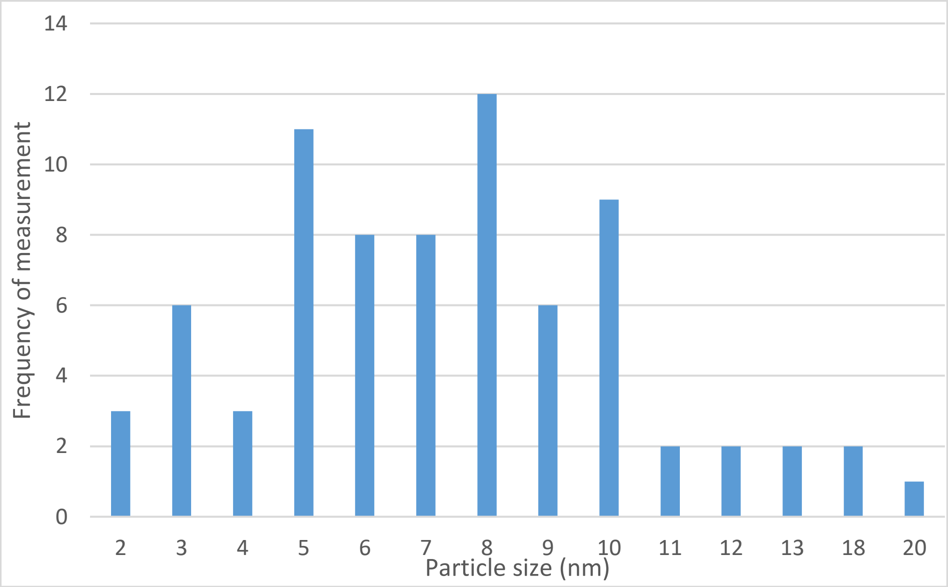

Mean	8.561
SD	3.275
Min	2.438
Max	20.000

Figure 3-10 Histogram displaying frequency of particle size measurements generated from TEM images

PdNPs can easily be distinguished from nuclei and other particles due to palladium having a higher atomic mass thus, the NPs therefore appear darker. The simple model of elastic scattering by Coulomb interaction of electrons with the atoms in a material is sufficient to explain basic contrast mechanisms in electron microscopy (Krumeich *et al*., 2016). The likelihood that an electron is deviated from its direct path by an interaction with an atom increases with the number of charges that the atom carries. Therefore, heavier elements represent more powerful scattering centres than a light element. Due to this increase in the Coulomb force with increasing atomic number, the contrast of areas in which heavy atoms are localized will appear darker than of such comprising light atoms (Krumeich *et al*., 2016).

3.5.3 Zeta-potential and DLS measurements

The zeta potential measurements and nanoparticle size for the synthesized PdNPs was determined using a Malvern Zetasizer after 1 week following the synthesis. For the NPs to be regarded as stable, their zeta potential values should be greater than +30 mV or lower than -30 mV (Koteswari *et al*., 2011). The zeta potential and size distribution was accomplished by adding the *Ulva* supported PdNPs to two solvents ethylene glycol and ethyl acetate these were finely chosen based on the solubility of the PdNPs in these solvents where they exhibited better solubility than other tested solvents. The zeta potential values determined for the PdNPs in ethylene glycol and ethyl acetate are -36.4 mV and -16.9 mV respectively showing that they are stable in ethylene glycol solutions. A notable change is the pH of the solvent used to dissolve the samples, ethylene glycol has a pH range of 5.5 - 7.0 while ethyl acetate has a pH of 2.1. Adsorption of H^+ and OH^- ions on the surface of material change the surface charge of the material i.e. the zeta potential value. In acidic solutions, is expected the zeta potential value increases and *vice versa*. The mean particle size using ethyl acetate as the solvent was determined to be 103 nm while the NPs were determined to be 1696 nm in ethylene glycol.

3.5.4 X-Ray powder Diffraction

The diffraction patterns for the “green” synthesized PdNPs supported on *Ulva* revealing crystallinity of the synthesized PdNPs.

(Figure 3-11) shows that the sample prepared using a 1 mM Pd(II) salt solution at 800 ºC contained. with reflections at 33.6°(002), 34.0° (101), 42.0° (110), 54.9° (112), 60.3° (103), and 71.7° (211). No further studies were conducted on these NPs as this result was not for seen. This was however observed in a study by (Parker *et al*., 2014). The presence of PdO could be attributed to interaction between the $Pd^{(2+)}$ and oxygen that is given off during heating (Parker *et al*., 2014).

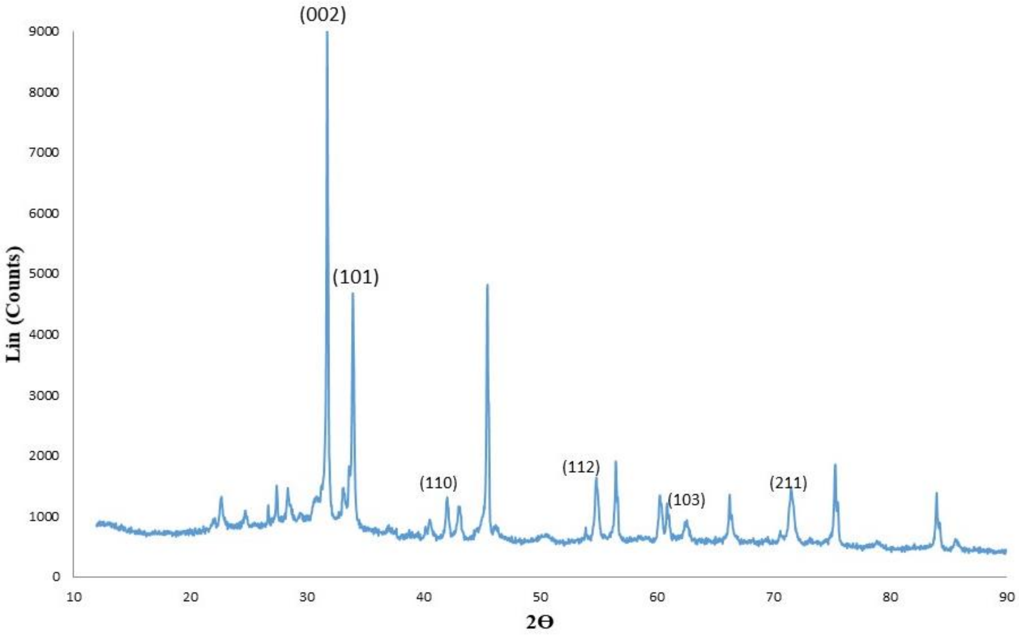

Figure 3-11 XRD diffraction pattern of PdO produced when *Ulva armoricana* was calcined at 800 ^{o}C.

Figure 3-12 reveals the PdNPs to have five reflections corresponding to 2θ at 40.10^{o}, 46.49^{o}, 68.12^{o}, 81.60^{o} and 86.19^{o} can be attributed to the (111), (200), (220), (311) and (222) crystalline planes of the face-centred cubic (fcc) crystalline structure of Pd, respectively (as per JCPDS file no. 00-043-1024**)**. The Pd nanoparticle size was also determined using the Debye-Scherer equation (Equation 2-4). The crystallite size of the synthesized PdNPs was found to be 2.7 nm. The PdNPs synthesised using 0.5 mM solution was subsequently used as the catalyst for several Suzuki coupling reactions.

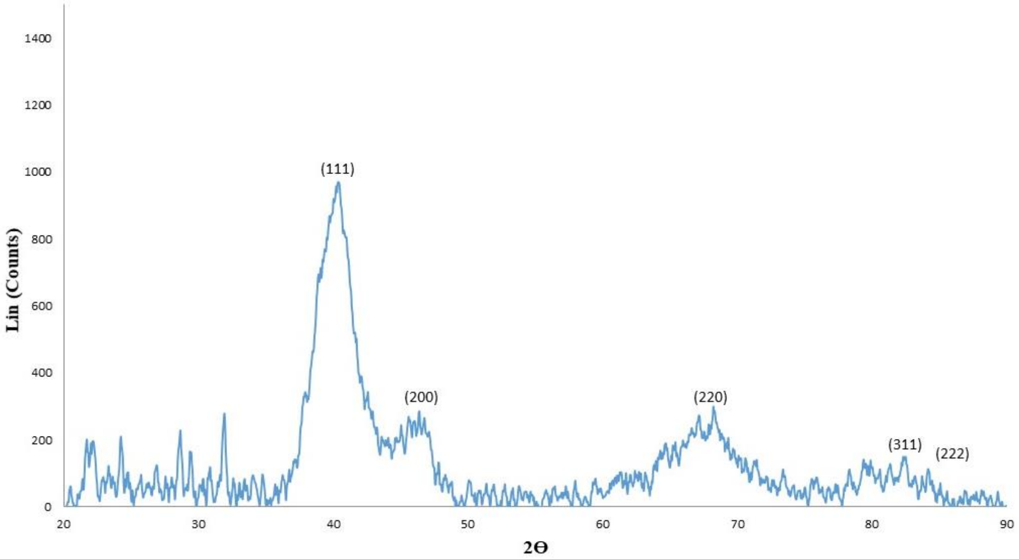

Figure 3-12 XRD diffraction pattern of the PdNPs supported on *Ulva armoricana* that was steeped in the 0.5 mM K_2PdCl_4.

3.5.5 FT-IR spectroscopy

FT-IR was used to determine the primary functional groups present in the *Ulva* sample which could act as a capping agent and a reducing agent and also to gain possible information on any possible palladium co-ordination that might be observed. The capping agent plays a crucial role in the stabilization of the PdNPs. The FT-IR spectrum of the aqueous extract of *Ulva*, as well as the FT-IR spectra of the *Ulva* dried sample with no palladium and that of the biosynthesized PdNPs supported on *Ulva* were acquired. Furthermore, the FT-IR of 10% wt Pd/C is also shown. This was carried out to determine whether any change in functional groups took place during the bioreduction processes.

In Figure 3-13 a broad peak at 3202 cm^{-1} corresponds to a hydroxy functional group and may in part be due to water. The broad peak at 1634 cm^{-1} is indicative of a C=C stretch and a sharp signal 1402 cm^{-1} is typical of a C-C skeletal vibration. A sharp methyne, secondary alcohol or C-O stretch could account for the signal observed at 1082 cm^{-1}. A stretch at 738 cm^{-1} which could be indicative of an alcohol out of plane stretch and a mono substituted (phenyl) group for the *Ulva* sample.

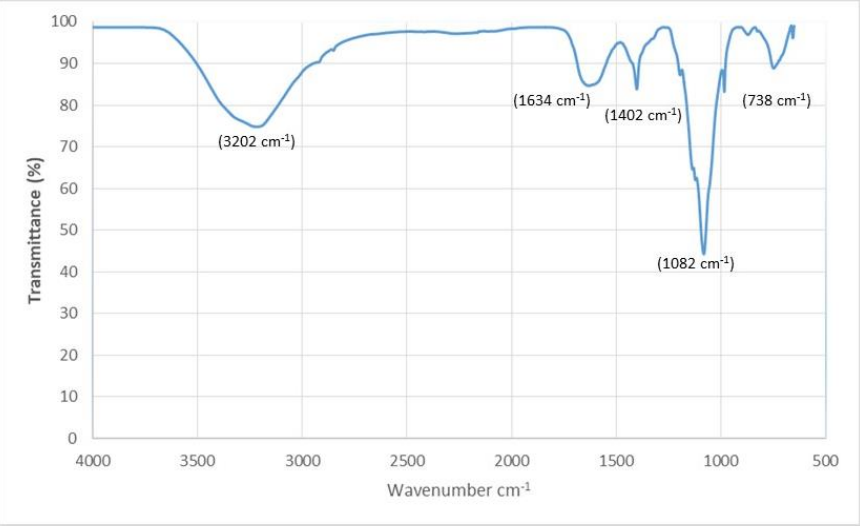

Figure 3-13 FT-IR spectrum of Ulva armoricana aqueous extract.

The FT-IR spectrum of *Ulva* ashed with but no palladium present exhibits a similar spectrum and the following characteristics were observed. There was a sharp peak at 880 cm^{-1} which indicates presence of an aromatic C-H out of plane bend. A high intensity, sharp peak at 1067 cm^{-1} shows presence of an in-plane aromatic C-H, bend where sharp peaks at 1251 cm^{-1} and 1394 cm^{-1} indicate a vinylidene C-H in plane bend and methylene C-H asymmetric/symmetric stretch, respectively (Mukhoro *et al*., 2017). A signal at 2973 cm^{-1} and 2901 cm^{-1} shows a possible asymmetric C-H methyl or methylene stretch. The fact that the sample does not show a broad OH peak is due to the fact that the sample was ashed at 300 ^{o}C. The OH peak in (Figure 3-13) may also be responsible for masking the strong signals at 2900 cm^{-1} as apparent in (Figure 3-14).

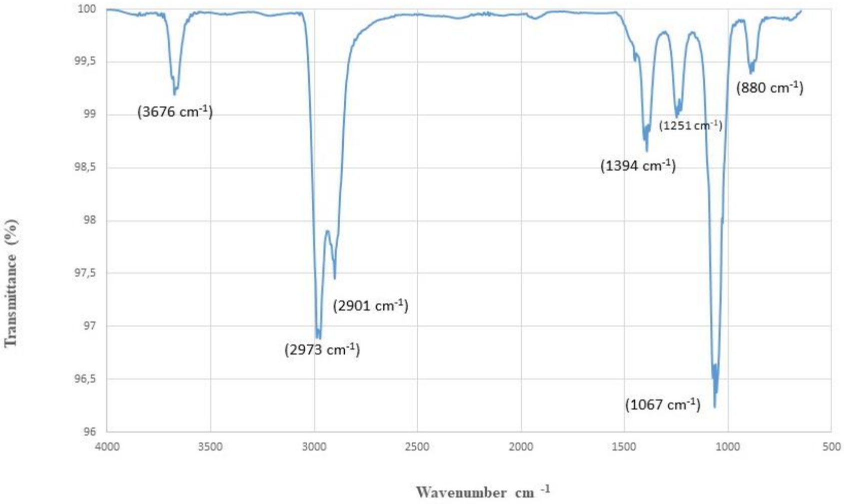

Figure 3-14 FT-IR spectrum of ashed *Ulva armoricana* containing no palladium.

The ashed Ulva armoricana containing PdNPs (Figure 3-15) FT-IR spectrum, is an exact overlay of the FT-IR spectrum of ashed Ulva armoricana sample containing no palladium. No apparent shifts in the peaks were noted.

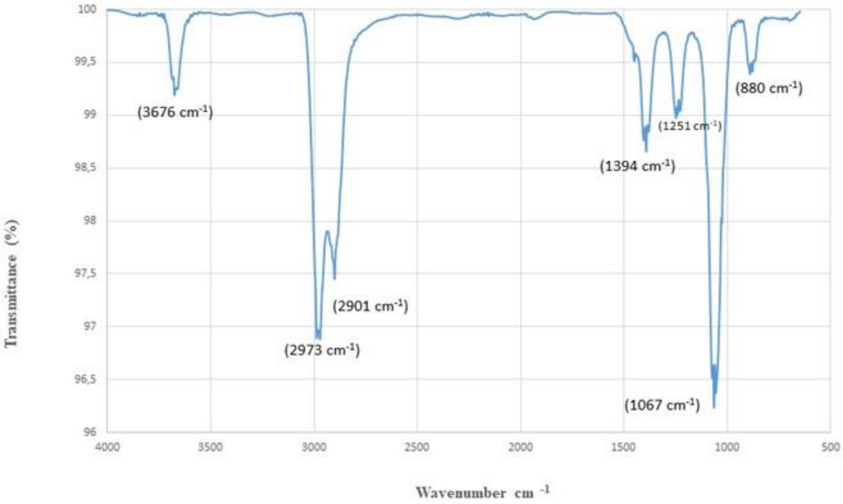

Figure 3-15 FT-IR spectrum of *Ulva armoricana* containing palladium.

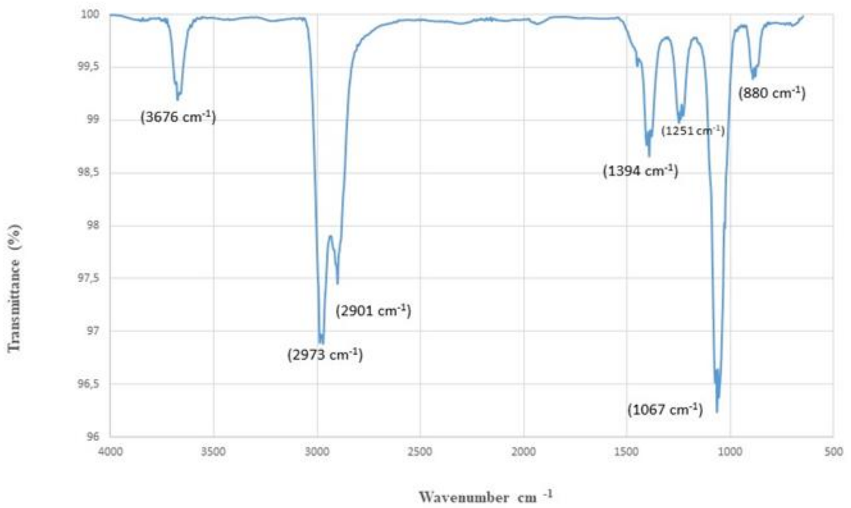

Figure 3-16 FT-IR spectrum of commercial 10% wt Pd/C.

Unfortunately the 10% wt Pd/C yields similar results as seen in (Figure 3-16), thus no differentiation can be made regarding the 3 different samples.

3.5.6 Inductively Coupled Plasma - Atomic Emission Spectroscopy (ICP-AES)

The Pd sample loading was determined to be 8% Pd loading on carbon. This sample was then employed as the Pd catalyst in the Suzuki carbon-carbon coupling reactions. The activity of this catalyst was compared to the commercially available 10 % Pd/C catalyst.

3.5.7 Thermal Analysis

The TGA curves for the *Ulva armoricana* air dried sample, *Ulva armoricana* ashed with no palladium and that of the *Ulva* supported PdNPs are shown in Figure 3-17. Four major events of mass loss were observed in the TGA curves. The first two stages of mass loss were observed in the region of 30 to 120 °C with the second stage seen between 120 and 250 °C. The first stage may be attributed to the loss of volatile and water components (Martins *et al*., 2015). The air dried sample has a major mass loss form 250-400 °C then a steady decrease in mass to 32% at 750 °C. Both samples without Pd have a mass loss of over 70%. The gradient of the ashed *Ulva* sample is also not as steep as that of the air dried *Ulva* which may be attributed to the degradation of some organic material during ashing at 300 °C (Martins *et al*., 2015).

It is noted that at this stage the mass of *Ulva* supported PdNPs at 750 °C is slightly less than that of the *Ulva* ashed with no Pd present. The mass of the *Ulva* supported PdNPs does not reach zero which is attributed to the PdNPs as well as some inorganic materials found in seaweeds. Thus it was necessary to compare the ashed *Ulva* sample without Pd to the sample with Pd to get a true indication of the Pd content. The difference in the mass between these samples is not a true reflection of the Pd present in the *Ulva* sample. Carbon is expected to decompose at approximately 500 ^{o}C, and thus it was assumed that all of the seaweed would have been consumed at this stage. A 100% mass loss was not observed and could be due to the presence of sea salt (NaCl and KCl) in the seaweed sample but the XRD data did not show this.

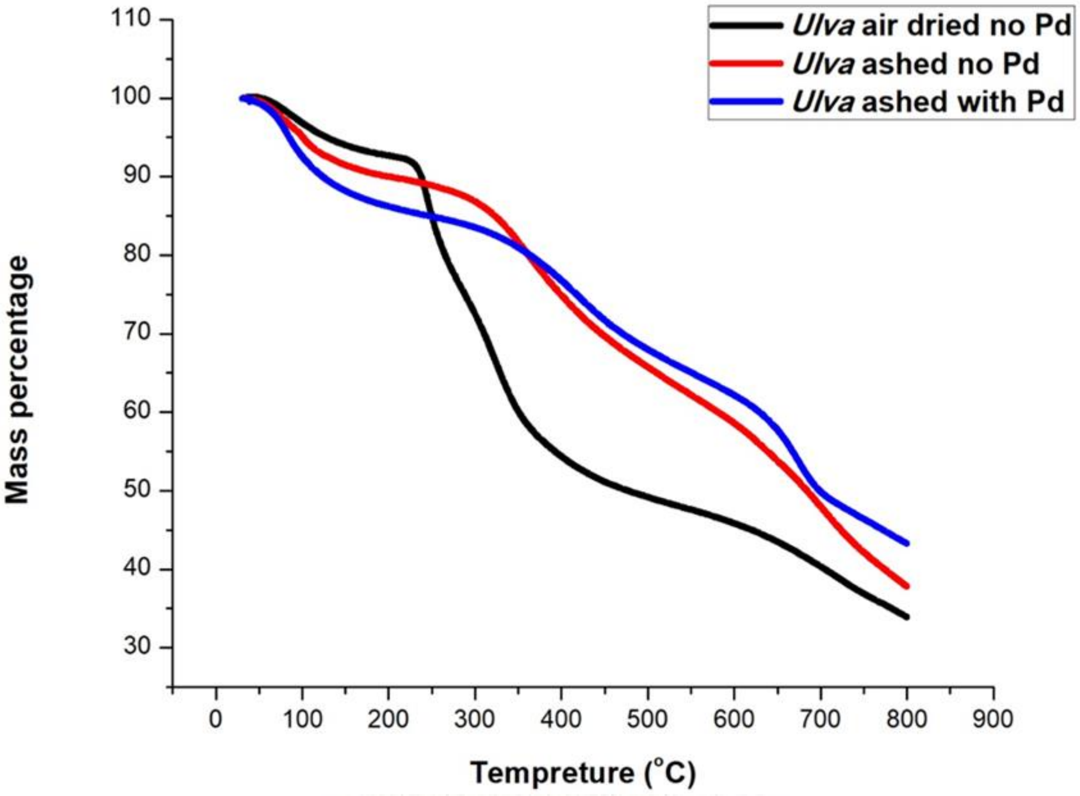

Figure 3-17 TGA curves of *Ulva armoricana* air dried sample, *Ulva armoricana* ashed with no palladium present and that of the Ulva supported PdNPs form 50 ^{o}C to 800 ^{o}C.

3.6 Conclusion

It can be stated that live *Ulva armoricana* was able to reduce Pd^{2+} to Pd^{0} (zero valent state) and act as a support for PdNPs. The *Ulva armoricana* was able to reduce the 0.25 mM and the 0.5 mM concentration solutions. Baseline absorbance peaks for the Pd^{2+} solution was established at 207 nm and 242 nm. These absorbance values and their changes were measured with respect to time in order verify with the use of UV-Vis if there are changes in these values. It was observed that the absorbance peak at 242 nm decreased with respect and the absorbance peak at 207 nm increased. TEM images were obtained for the sample containing the 0.5 mM solution and ashed at 300 ^{o}C at 1 ^{o}C/min to produce the *Ulva* supported PdNPs. HR-TEM images of this sample revealed spherical PdNPs with an average size of 7 nm. The EDX spectrum were also was recorded, confirming the presence of Pd in the sample. Zeta potential readings were calculated to be -36.4 mV and 16.9 mV, using ethylene glycol and ethyl acetate, respectively. These dispersants provided the best solubility for the PdNPs. DLS analyses revealed the mean particle size to 103 nm in ethyl acetate and 1696 nm for ethylene glycol. XRD diffraction patterns were also obtained and 2Ө characteristic Miller indices in line with reported values in literature, was reported. Unexpected observation was made, that the *Ulva armoricana* produced PdO NPs when the seaweeds were ashed at a temperature of 800 °C under air. It is important to note that the characterisation TEM, XRD and DLS have different measuring parameters. TEM is a characterisation tool for directly imaging nanomaterial to obtain a qualitative measure and quantitative average of particle and/or grain size, size distribution, and morphology but it is limited as one only observe the section which has been selected. XRD is a technique used for determining the atomic and molecular structure of a crystal, in which the crystalline atoms cause a beam of incident X-rays to diffract into many specific directions, moreover this techniques gives a better distribution and average of the particle size. DLS measures hydrodynamic size and is the hypothetical hard sphere that diffuses in the same fashion as that of the particle being measured hence termed the hydrodynamic diameter and not the particle size being measured. ICP-AES indicated that the amount of Pd loading was 8% for Pd supported on *Ulva armoricana*. TGA analyses revealed that the mass percentage of the sample containing either no Pd or Pd did not reach zero percent, however, overall the PdNP supported on *Ulva* had the highest mass percentage retained after the TGA analysis indicating increased stability.

Chapter 4

4.1 Overview

This chapter reports on the synthesis of several biaryl compounds using commercially available 10% wt Pd/C as a standard catalyst and the Ulva supported PdNPs prepared as described in chapter 3. The characterization of these bi-aryl compounds was accomplished using both 1D and 2D NMR, TLC, FT-IR and GC-EIMS.

4.2 Introduction

Cross-coupling reactions have been an impressive tool for organic chemists for much of the past century. It has only been in the last half century that great advances have been made, all of which take advantage of organometallic chemistry. The most widely explored reactions use palladium or nickel complexes to promote the cross-coupling of a wide variety of functionalized aryl groups and substituted biphenyl compounds (Beccalli *et al*., 2007).

The cross-coupling of alkyl aryl boronic acids with alkyl halides, known as the Suzuki-Miyaura reaction, has found use as an efficient and less toxic method to form direct carbon-carbon bonds (Suzuki and Miyaura, 1995). The reaction can be used with a variety of functional groups and the presence of water and other organic solvents that usually do not adversely affect it (Buchwald *et al*., 2006). The first evidence of this was published in 1979 by Suzuki and Miyaura who showed the cross-coupling of 1-alkenylboranes with 1-alkenyl halides, 1-alkynyl halides and with aryl halides (Negishi *et al*., 2003). One of the key requirements of the reaction was the need for a base to facilitate the activation of the boronic acid during transmetallation step (Negishi *et al*., 2003). These findings opened a new pathway for the synthesis of sp^2-sp^2 and sp^2-sp carbon-carbon bonds in a highly selective manner.

The mechanistic pathway of the Suzuki-Miyaura cross-coupling is similar to that of the Kumada coupling, however, the exact transmetallation process is unclear. The transmetallation under the Suzuki-Miyaura conditions concerns the transfer of an organic group from a borane, boronic acid, or boronic ester.

Miyaura and Suzuki postulated that due to the presence of a base, a hydroxide moiety adds to the boronic acid to form tetrahedral anion, which is more reactive than the neutral boron. They also completed kinetic studies on the use of water and base and found that both were required to activate the boronic acid to the salt (Negishi *et al*., 2003).

More evidence was generated using electrospray ionization mass spectroscopy which supports the use of the activated boronic acid as the key intermediate for the transmetallation intermediate (Suzuki and Miyaura, 1995). Another method of activation using the base was put forth by Suzuki who theorized that prior to the transmetallation, the replacement of the halogen with a base on the palladium was the key intermediate that promoted the addition of the organo boronic acid (Suzuki and Miyaura, 1995). Overall, the mechanistic cycle requires a base to perform the transmetallation, regardless of the pathway taken.

Many of the early examples of the Suzuki-Miyaura cross-coupling reactions used various phosphine ligands, the most common being triphenylphosphine (PPh_3). An advance came in 1994 when Novak *et al* (1998) developed a phosphine-free palladium sources, who used palladium acetate, [(ŋ^3-C_3H_5) PdCl]$_2$, and Pd_2 (dba)$_3$.C_6H_6 and found that all three showed higher reactivity than Pd(PPh_3)$_4$ (Novak *et al*., 1998). It was also found that the addition of excess PPh_3 to the catalyst system slowed the rate of reaction. One final observation made by Novak was the influence the pH had on the rate. When K_2CO_3 was used as the base rather than $KHCO_3$, the reaction rate and yield increased.

A new, novel reaction to the synthesis of complex molecules is often a true test to the significance of a reaction. Such an application for the Suzuki-Miyaura cross-coupling reaction was in the synthesis of palytoxin carboxylic acid and palytoxin amide; toxins which were isolated from a marine organism by Kishi in 1989 as seen in

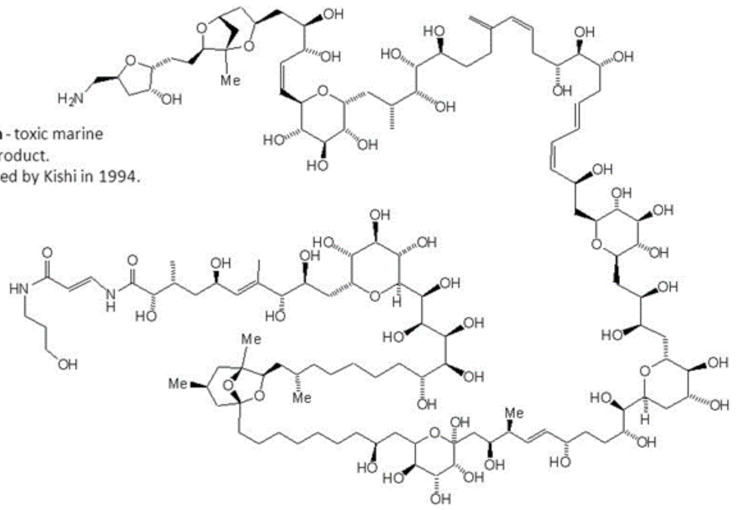

Figure 4-1 Structure of Polytoxin (Suh and Kishil, 1989).

4.3 Experimental procedures

4.3.1 Materials used

Table 4-1 Materials used in synthesis of bi-arly products.

2-iodoanisole	Preparative TLC plates 1000 µm
3-iodoanisole	N,N-dimethylformamide
4-iodoanisole	$MgSO_4$
Phenylboronic-acid	NaCl
4-(hydroxymethyl) phenylboronic acid	Ethyl acetate
Diethyl ether	Hexane Celite
1M NaOH	10%wt Pd/C
TLC Silica gel 60 F_{254}	

The starting materials where purchased from Sigma Aldrich and used as received.

4.3.2 Equipment and general experimental procedures used

NMR spectra (^{1}H, ^{13}C and HSQC) were acquired on a Bruker 400 MHz Avance IIIHD Nanobay spectrometer equipped with a 5 mm BBO probe at 333K using standard 1D and 2D NMR pulse sequences. All spectra were referenced to residual undeuterated solvent peaks. NMR spectra are values are reported in ppm relative to $CDCl_3$ calibrated to 7.26 ppm in the ^{1}H NMR and 77.00 in the ^{13}C NMR. Splitting patterns are abbreviated as follows: singlet (s), doublet (d), triplet (t), quartet (q), multiplet (m), doublet of doublet (dd), triplet of doublet (td), doublet of triplet (dt).

GC-EIMS analysis were performed using Agilent Technologies 7820A GC coupled to an Agilent 5977E MS with a HP5 MS column (5% phenyl methyl silox). The initial temperature was 40 °C and final temperature was raised to 325 °C at a heating rate of 20 °C/min. The total run time was 30 min per compound. The carrier gas was Helium with a flow rate of 1.5 ml/min. Sample volume was 1 µl.

Air-sensitive reactions were performed under an inert atmosphere of nitrogen using double necked round bottom flasks. The reactions was monitored using TLC Silica gel 60 F_{254} aluminium sheets, which were also used in the preparative TLC steps for the purification of selected compounds. The final products was worked up by as follows the solution was a triphasic mixture with copious amounts of palladium black floating between the layers. The reaction was transferred to a 250 ml separating funnel and extracted into diethyl ether (2 × 10 mL). To this mixture 5 ml of 1M NaOH was added. The organic layers were combined, washed with water (1 × 100 mL) saturated with sodium chloride and dried over magnesium sulfate and filtered through a 2 cm celite cake. Solvent was then removed with a rotary evaporator to yield the product. The products was then purified using preparative TLC method where an ethyl acetate: hexane (1: 9) solvent system was used. The samples was then stored in a desiccator to avoid any moisture from entering the compounds.

For the general synthesis of the biaryl products, to a two neck round bottom flask equipped with a reflux condenser was added K_2CO_3 (3mmol) in 5 mL of dry DMF. The boronic acid (1mmol) and aryl halide (1mmol) was added and the mixture was stirred for 5 mins. To this mixture Pd/C 10% wt or *Ulva* supported PdNPs was added (15mg) to 1 ml of DMF and allowed to react for 8 hours at 130 ^oC with constant reaction monitoring using TLC. Observations include a colour change from black solution to a dark purple after the first hour, which kept constant for at least 3 hours. A second colour change back to a black solution after reaction was observed upon completion of the synthesised compounds which had a variety of textures and colours. The reaction scheme of this synthetic method is proposed in (Figure 4-2).

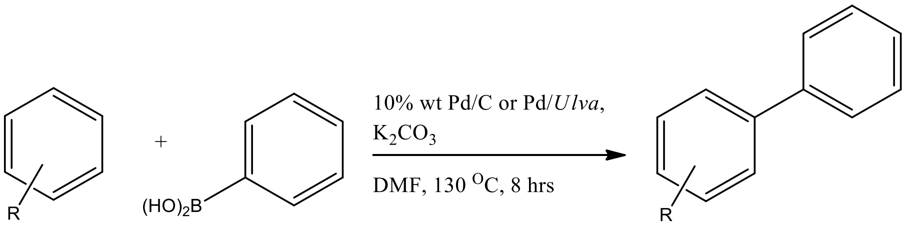

Figure 4-2 Reaction scheme for the synthesis of biaryl compounds using *Ulva* supported PdNPs and commercially available 10% wt Pd/C.

An important note for the reaction scheme is the temperature of the reaction was kept between 100 ^oC to a maximum temperature of 130 ^oC, and the use of DMF as a solvent should be kept to a minimum volume. A base K_2CO_3 was employed.

4.3.3 General synthetic methods employed for the Suzuki carbon-carbon cross coupling reactions

To study the cross-coupling reaction between aryl halides and phenylboronic acids, selective starting materials were chosen. For the aryl halides: 2-iodoanisole, 3-iodoanosle, 4-iodoanisole and 3-fluoro-2-iodoanaisole were chosen. Phenylboronic acid was chosen as well as 4(hydroxymethyl) phenylboronic acid were used. Aryl halides containing iodine was chosen as iodine is a good leaving group and well suited for the highly selective carbon-carbon coupling reactions. The reaction conditions were optimised several times to find the “greenest” conditions. In total 8 products were synthesized using the commercially available catalyst 10% wt Pd/C and *Ulva* supported PdNPs making a total of 16 compounds synthesized. 1D and 2D NMR spectra were acquired where necessary, and additional conformation of these products was provided using GC-EIMS.

Table 4-2 depicts the starting reagents (aryl halide and aryl boronic acid), expected product and the yield of the product using the commercially available 10 % wt Pd/C and PdNPs supported on Ulva.

Table 4-2 Summary of reactions performed using the commercially available 10% Pd/C catalyst and the *Ulva* supported PdNPs.

Entry	**Aryl halide**	**Aryl boronic acid**	**Expected product**	**Yield%**	
				Pd/C	***Ulva*/PdNPs**
1	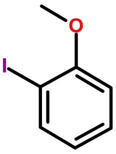	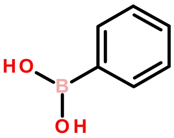	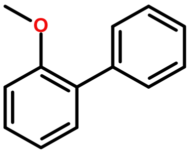 **4-a** **1-methoxy-4-phenyl-benzene**	75%	68%
2	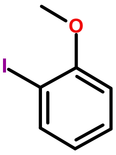	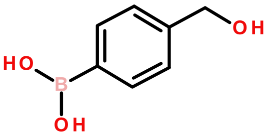	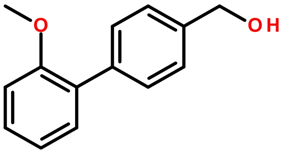 **4-b** **[4-(2-methoxyphenyl)phenyl]methanol**	65%	55%
3	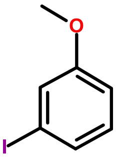	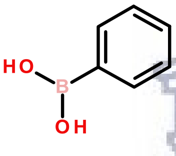	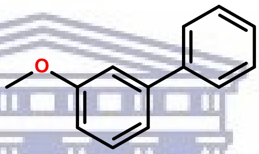 **4-c** **1-methoxy-3-phenyl-benzene**	75%	70%
4	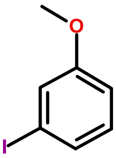	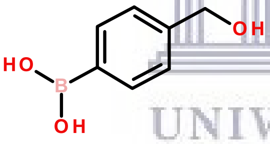	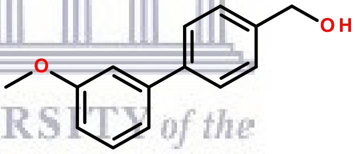 **4-d** **[4-(2-methoxyphenyl)phenyl]methanol**	70%	68%
5	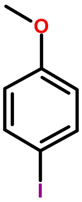	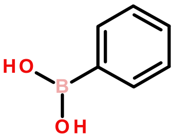	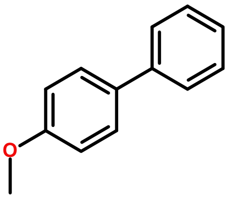 **4-e** **1-methoxy-3-phenyl-benzene**	75%	75%
6	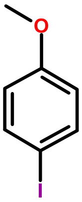	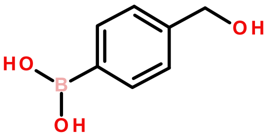	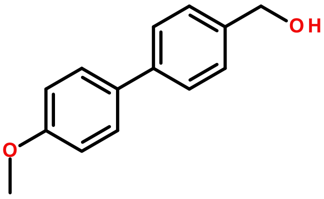 **4-f** **[4-(2-methoxyphenyl)phenyl]methanol**	70%	70%

An important note: Compounds denoted with no prime (‘) are the compound synthesised using the commercially available 10% wt Pd/C catalyst while compounds denoted with a prime (‘) is compounds synthesised using the *Ulva* supported PdNPs.

4.3.4 Experimental data

4.3.4.1 Compound **4-a** (1-methoxy-2-phenyl-benzene)

The product was purified using preparative thin layer chromatography on silica plate with a mobile phase ethyl acetate/hexane (1:9) and a dark orange oil obtained. ^{1}H NMR (400 MHz, CDCl$_3$): δ 7.69 (dd, *J* = 7.2 Hz/ ^1J = 2.02 Hz, 1H), 7.33 (t, *J* = 7.8 Hz, 2H), 7.24 (m, 1H), 7.45 (d, *J* = 7.3 Hz, 1H), 6.95 (t, *J* = 7.4 Hz, 1H), 6.93 (d, *J* = 8.4 Hz, 2H), 6.63 (t, *J* = 1.1 Hz, 1H), 3.72 (s, 3H). ^{13}C NMR (100MHz, CDCl$_3$): δ 55.6, 111.3, 120.9, 126.9, 128.0, 128.6, 128.7, 130.7, 130.9, 138.6, 156.5. GC-EIMS (70eV) *m/z* (%), retention time: *m/z* ion 184.2 (40%), t_R = 21.61 min, mass of product 0.136 g, % yield = 75%.

4.3.4.2 Compound 4-a’ (1-methoxy-2-phenyl-benzene)

The product was purified using preparative thin layer chromatography on silica plate with a mobile phase ethyl acetate/hexane (1:9) and a dark orange oil obtained. ^{1}H NMR (400 MHz, CDCl$_3$): δ 7.68 (dd, *J* = 7.7 Hz/ ^1J = 2.02 Hz, 1H), 7.32 (t, *J* = 7.76 Hz, 2H), 7.23 (m (1H), 7.44 (d, *J* = 7.2 Hz, 1H), 6.95 (t, *J* = 7.4 Hz, 1H), 6.93 (d, *J* = 8.4 Hz, 2H), 6.63 (t, *J* = 1.1 Hz, 1H), 3.79 (s, 3H). ^{13}C NMR (100MHz, CDCl$_3$): δ 55.5, 111.7, 120.8, 126.9, 127.9, 128.6, 129.5, 130.6, 130.8, 138.5, 156.4. GC-EIMS (70eV) *m/z* (%), retention time: *m/z* 184.2 (42%), t_R = 21.417 min, mass of product 0.124 g, % yield = 68%.

4.3.4.3 Compound **4-b** [4-(2-methoxyphenyl) phenyl] methanol

The product was purified using preparative thin layer chromatography on silica plate with mobile phase ethyl acetate/hexane (1:9) and an orange oil obtained. ^{1}H NMR (400 MHz, CDCl$_3$): δ 7.65 (dd, *J* = 6.0 Hz/ ^1J = 1.5 Hz, 1H), 7.4 (d, *J* = 8 Hz, 2H), 7.29 (d, *J* = 8 Hz, 2H), 7.19 (d, *J* = 7.3 Hz, 1H), 6.91 (t, *J* = 7.46, 1H), 6.87 (m, (1H), 4.58 (s, 2H), 3.73 (s, 3H), 3.67 (s, 1H). ^{13}C NMR (100MHz, CDCl$_3$): δ 55.2, 64.6, 112.6, 112.8, 119.5, 127.1, 127.3, 130.2, 139.9, 140.7, 142.3, 162.8. GC-EIMS (70eV) *m/z* (%), retention time: *m/z* 214.2 (31%), t_R = 23.03 min, mass of product 0.139 g, % yield = 65%.

4.3.4.4 Compound **4-b’** [4-(2-methoxyphenyl) phenyl] methanol

The product was purified using preparative thin layer chromatography on silica plate with mobile phase ethyl acetate/hexane (1:9) and an orange oil obtained. ^{1}H NMR (400 MHz, CDCl$_3$): δ 7.67 (dd, *J* = 6.0 Hz/ ^1J = 1.5 Hz, 1H), 7.43 (d, *J* = 8 Hz, 2H), 7.30 (d, *J* = 8 Hz, 2H), 7.22 (d, *J* = 7.3 Hz, 1H), 6.93 (t, *J* = 7.46, 1H), 6.88 (m, (1H), 4.61 (s, 2H), 3.77 (s, 3H), 3.70 (s, 1H). ^{13}C NMR (100MHz, CDCl$_3$): δ 55.5, 65.1, 114.9, 120.9, 127.2, 127.7, 128.7, 130.4, 130.8, 137.8, 139.7, 156.5. GC-EIMS (70eV) *m/z* (%), retention time: *m/z* ion 214.2 (62%), t_R = 23.04 min, mass of product 0.119 g, % yield = 55%.

4.3.4.5 Compound **4-c** (1-methoxy-3-phenyl-benzene)

The product was purified using preparative thin layer chromatography on silica plate with mobile phase ethyl acetate/hexane (1:9) and a yellow oil obtained. ^{1}H NMR (400 MHz, $CDCl_3$): δ 7.51 (d, J = 7.2 Hz, 2H), 7.36 (t, J = 7.8 Hz, 1H), 7.30–7.26 (m, 1H), 7.1 (d, J = 7.2 Hz, 1H), 7.06–7.04 (m, 2H), 7.18 (s,1H), 6.83 (dd, J = 8.7 Hz/ ^{1}J = 1.9 Hz, 1H), 3.80 ppm (s, 3H). ^{13}C NMR (100MHz, CDCl3): δ 55.3, 112.9, 119.7, 127.2, 127.4, 128.8, 129.8, 141.1, 142.8, 160.0 ppm. GC-EIMS (70eV) *m/z* (%), retention time: *m/z* ion 184.2 (49%), t_R = 22.53 min, mass of product 0.134 g, % yield = 75%.

4.3.4.6 Compound **4-c’** (1-methoxy-3-phenyl-benzene)

The product was purified using preparative thin layer chromatography on silica plate with mobile phase ethyl acetate/hexane (1:9) and a yellow oil obtained. ^{1}H NMR (400 MHz, $CDCl_3$): δ 7.51 (d, J = 7.2 Hz, 2H), 7.36 (t, J = 7.8 Hz, 1H), 7.30 – 7.26 (m, 1H), 7.1 (d, J = 7.2 Hz, 1H), 7.06 – 7.04 (m, 2H), 7.18 (s,1H), 6.83 (dd, J = 8.7 Hz/^{1}J = 1.9 Hz, 1H), 3.80 ppm (s, 3H). ^{13}C NMR (100MHz, $CDCl_3$): δ 55.3, 112.7, 113.0, 119.7, 123.0, 127.2, 128.2, 129.8, 141.1, 142.8, 160.0 ppm. GC-EIMS (70eV) *m/z* (%), retention time: *m/z* ion 184.2 (55%), t_R = 21.63 min, mass of product 0.127 g, % yield = 70%.

4.3.4.7 Compound 4-d [4-(3-methoxyphenyl) phenyl] methanol

The product was purified using preparative thin layer chromatography on silica plate with mobile phase ethyl acetate/hexane (1:9) and a pale yellow oil obtained. ^{1}H NMR (400 MHz, $CDCl_3$): δ 7.45 (d, J = 8 Hz, 2H), 7.3 (d, J = 8 Hz, 2H), 7.22 (t, J = 8 Hz, 1H), 7.1 (d, J = 7.72 Hz, 1H), 7.00 (s, 1H), 6.77 (m (d), J = 5.7 Hz), 4.59 (s, 2H), 3.72 (s, 3H), 3.63 (s, 1H). ^{13}C NMR (100MHz, $CDCl_3$): δ 55.2, 64.6, 112.6, 112.8, 119.5, 127.1, 127.3, 130.2, 139.9, 140.7, 142.3, 162.8. GC-EIMS (70eV) *m/z* (%), retention time: *m/z* ion 214.2 (37%), t_R = 25.24 min, mass of product 0.138 g, % yield = 70%.

4.3.4.8 Compound **4-d’** [4-(3-methoxyphenyl) phenyl] methanol

The product was purified using preparative thin layer chromatography on silica plate with mobile phase ethyl acetate/hexane (1:9) and a pale yellow oil obtained. ^{1}H NMR (400 MHz, $CDCl_3$): δ 7.45 (d, J = 8 Hz, 2H), 7.3 (d, J = 8 Hz, 2H), 7.23 (t, J = 8 Hz, 1H), 7.1 (d, J = 7.72 Hz, 1H), 7.00 (s, 1H), 6.77 ((dd), J = 5.7 Hz, 1H), 4.59 (s, 2H), 3.73 (s, 3H), 3.64 (s, 1H). ^{13}C NMR (400MHz, $CDCl_3$): δ 55.3, 64.6, 112.6, 112.8, 119.6, 127.2, 127.4, 130.8, 140.1, 140.6, 142.4, 162.8. GC-EIMS (70eV) *m/z* (%), retention time: *m/z* 214.2 (55%), t_R = 25.17 min, mass of product 0.130 g, % yield = 68%.

4.3.4.9 Compound **4-e** (1-methoxy-4-phenyl-benzene)

The product was purified using preparative thin layer chromatography on silica plate with mobile phase ethyl acetate/hexane (1:9) and a white powder obtained. ^{1}H NMR (400 MHz, $CDCl_3$): δ 7.50–7.56 (m, 4H), 7.41 (t, J = 7.6 Hz, 2H), 7.30 (t, J = 7.4 Hz, 1H), 6.98 (d, J = 8.8 Hz, 2H), 3.85 ppm (s, 3H). ^{13}C NMR (100 MHz, $CDCl_3$): δ 159.1, 141.0, 133.8, 128.7, 128.2, 126.8, 126.7, 114.2, 55.4 ppm. GC-EIMS (70eV) *m/z* (%), retention time: *m/z* 184.2 (49%), t_R = 22.66 min, mass of product 0.135 g, % yield = 75%.

4.3.4.10 Compound **4-e’** (1-methoxy-4-phenyl-benzene)

The product was purified using preparative thin layer chromatography on silica plate with mobile phase ethyl acetate/hexane (1:9) and obtained a white powder. ^{1}H NMR (400 MHz, $CDCl_3$): δ 7.48–7.43 (m, 4H), 7.33 (t, *J* = 7.6 Hz, 2H), 7.21 (t, *J* = 7.4 Hz, 1H), 6.90 (d, *J* = 8.8 Hz, 2H), 3.76ppm (s, 3H). ^{13}C NMR (100 MHz, $CDCl_3$): δ 159.1, 140.9, 133.8, 128.8, 128.2, 126.8, 126.7, 114.2, 55.4 ppm. GC-EIMS (70eV) *m/z* (%), retention time: *m/z* 184.2 (49%), t_R = 22.75 min, mass of product 0.133 g, % yield = 75%.

4.3.4.11 Compound **4-f** [4-(4-methoxyphenyl) phenyl] methanol

The product was purified using preparative thin layer chromatography on silica plate with mobile phase ethyl acetate/hexane (1:9) and a colourless oil obtained. ^{1}H NMR (400 MHz, $CDCl_3$): δ 7.83 (d, *J* = 7.26 Hz, 2H), 7.62 (d, *J* = 7.62 Hz, 2H), 7.38 (d, *J* = 8.0 Hz, 2H), 7.32 (d, *J* = 8.0 Hz), 4.62 (s, 1H), 3.76 (s, 3H), 3.75 (s, 1H). ^{13}C NMR (100MHz, $CDCl_3$): δ 55.3, 64.9, 114.2, 126.8, 127.5, 128.5, 130.3, 139.5, 140.0, 158.7. GC-EIMS (70eV) *m/z* (%), retention time. *m/z*: 214.2 (39%), t_R = 25.56 min, mass of product 0.139 g, % yield = 70%.

4.3.4.12 Compound 4-f’ [4-(4-methoxyphenyl) phenyl] methanol

The product was purified using preparative thin layer chromatography on silica plate with mobile phase ethyl acetate/hexane (1:9) and a colourless oil obtained. ^{1}H NMR (400 MHz, $CDCl_3$): δ 7.86 (d, *J* = 7.26 Hz, 2H), 7.65(d, *J* = 7.62 Hz, 2H), 7.42-7.39 (m (d), *J* = 8 Hz, 2H), 7.37 (d, *J* = 8.04 Hz), 4.66 (s, 1H), 3.78 (s, 3H), 3.77 (s, 1H). ^{13}C NMR (100MHz, $CDCl_3$): δ 54.3, 64.1, 113.2, 125.8, 126.5, 127.1, 132.4, 138.3, 139.2, 161.6. GC-EIMS (70eV) *m/z* (%), retention time. *m/z:* 214.2 (35%), t_R = 25.57 min, mass of product 0.138 g, % yield = 70%.

4.4 PdNPs synthesized by living Ulva as catalysts for Suzuki-Miyaura

4.4.1 Suzuki-Miyaura cross coupling model reaction

This section describes the model reaction used as the basis for successful Suzuki-Miyaura cross-coupling reactions. The 10% Pd/C catalyst was used, together with 4-iodoanisole and phenyl boronic acid as the starting materials to generate the 1-methoxy-4-phenyl benzene (4e) product. Subsequent to this, the reaction was repeated using the same starting materials but employing Ulva supported PdNP catalyst instead to produce the same 1-methoxy-4-phenyl benzene (4e’) product. The products synthesized using the Pd/C catalyst is denoted e.g. 4e, while that obtained using the Ulva supported PdNPs are denoted 4e’.

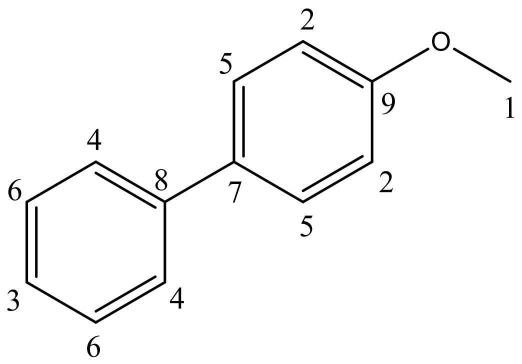

1-methoxy-4-phenyl-benzene, **(4-e)/(4-e')**

For ease of comparison and to distinguish those signals attributed to the starting materials, the ^{1}H NMR spectra acquired in $CDCl_3$ for the starting materials as well as the products **4e** and **4e'** are shown in Figure 4-3, while the ^{13}C spectra are shown in Figure 4-4.

The products **4e** and **4e'** were obtained as white powders and the NMR spectra both show the characteristic deshielded methoxy singlet at δ_H 3.82 (H-1) integrating to 3 protons. In addition, four sets of aromatic protons are observed at δ_H 7.05 (2H, d), 7.33 (1H, t, H-3), 7.45 (2H, t, H-6), and a multiplet at 7.63 integrating to 4 protons, indicating the presence of overlapped signals, as well as chemically equivalent protons, accounting for all 12 protons required for the structure. These spectra may also be found in the Appendix (compound **4e** and **4e'**). The chemical shift, multiplicity and the integration allowed us to assign the positions of H-1, H-3 and H-4 on the structure with relative ease. The overlapped signals at δ_H 7.63 were however resolved using HSQC and HMBC experiments, since the data is now separated over 2 dimensions. This is discussed later in this section. The disappearance of the doublet at δ_H 6.67 in particular for 4-iodoanisole for both the products **4e** and **4e'** indicates successful formation of the product, as well as purity. Phenyl boronic acid is not as soluble in chloroform as the anisole and thus it is not used as a measure of purity.

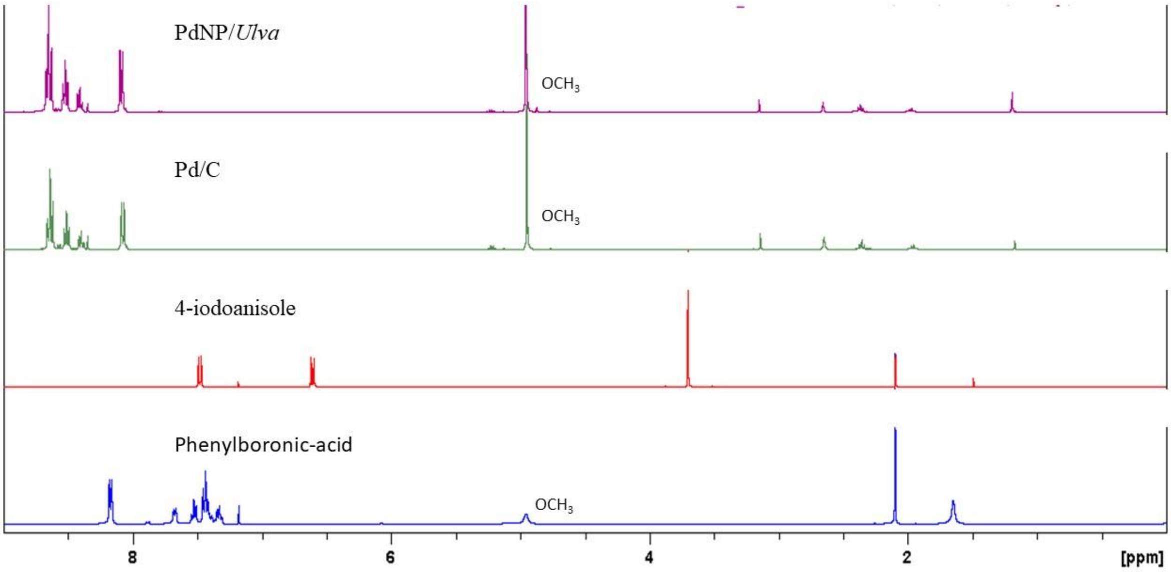

Figure 4-3 ^{1}H spectra ($CDCl_3$, 400 MHz) of 4-iodoanisole, phenylboronic acid and the 1-methoxy-4-phenyl-benzene product for *Ulva* supported PdNPs and the commercially available 10% wt Pd/C catalyst.

Figure 4-4 shows the ^{13}C spectra obtained for the starting materials (4-iodoanisole and phenylboronic acid), as well as the products obtained with the two catalysts, i.e. **4e** and **4e'**. All 9 signals expected for the 1-methoxy-4-phenyl benzene structure are accounted for, with 1 methoxy signal, 5 aromatic methine signals, and 3 quaternary carbon signals (taking into account chemical equivalence). The characteristic signals attributed to the methoxy carbon (C-3) and the aromatic =*C*-O carbon (C-9) are observed at δ_C 55.4 and 159.2 respectively. These are the typical chemical shifts expected for these moieties. The disappearance of the characteristic signal attributed to the aromatic iodo carbon (=*C*-I) observed at δ_C 82.7 has disappeared for both **4e** and **4e'** indicating successful formation of the C-C bond between the boronic acid the anisole. This together with the presence of two additional quaternary carbon resonances at δ_C 140.9 (C-8) and 133.8 (C-7) indicates successful formation of the C-C bond between the starting materials.

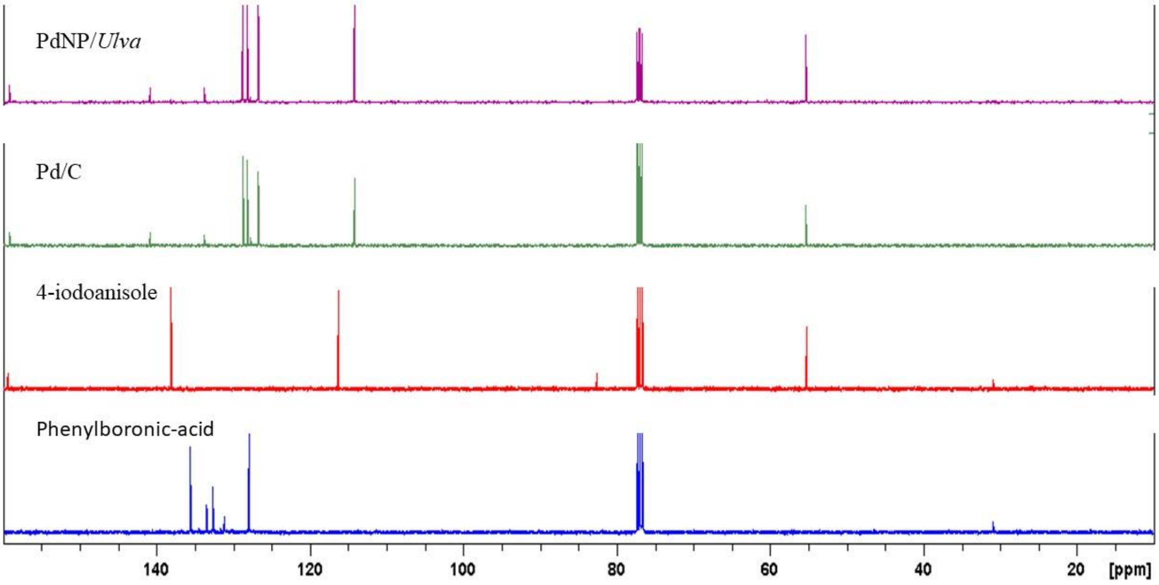

Figure 4-4 ^{13}C NMR spectra (CDCl3, 400 MHz) of product 1-methoxy-4-phenyl-benzene using *Ulva* supported PdNPs catalyst and the commercially available 10%wt Pd/C, 4-iodoanisole and phenylboronic acid.

The HSQC experiment was used to unmask the overlapping multiplet integrating to 4 protons resonating at δ_H 7.63 alluded to earlier. Since the data acquired for an HSQC spectrum is dispersed over two dimensions, overlapping signals are often clearly resolved and the data obtained is shown in Figure 4-5. It becomes quickly apparent that the multiplet at δ_H 7.63 is in fact two sets of doublets. On further inspection of the HSQC and data as well as the HMBC spectrum acquired (data not shown), it becomes apparent that the doublet residing at δ_H 7.05 and this signal at δ_H 7.63 are part of the same ring system. The data obtained from the 2D NMR spectra along with the 1D data, together with the assignments are given in Table 4-3.

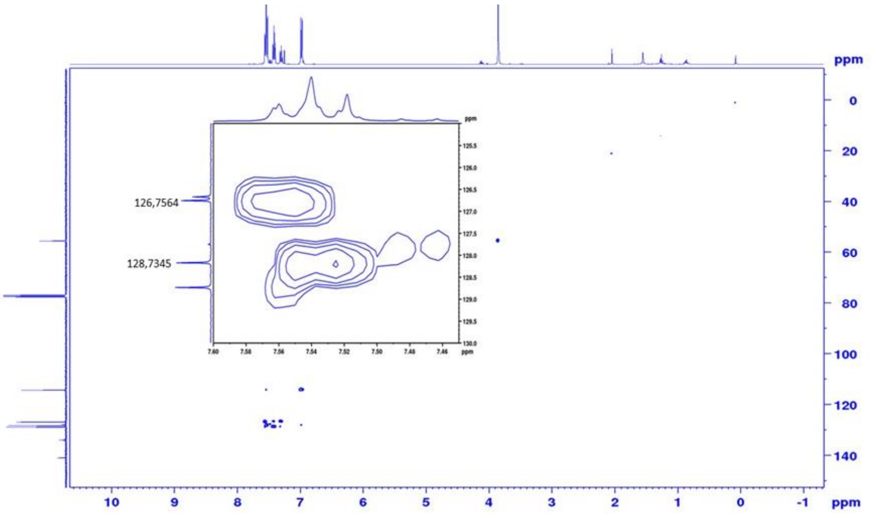

Figure 4-5 HSQC data ($CDCl_3$, 400 MHz) of 1-methoxy-4-phenyl-benzene depicting the overlapped C signals, the doublets and the triplet.

Table 4-3 Full ^1H and ^{13}C assignments for 1-methoxy-4-phenyl-benzene, which is accompanied by the HMBC assignment

Atom number	**δ_C**	**δ_H (multi , int , *J* in Hz)**	**HMBC**
1	55.4	3.85 (s , 3H)	C9
2	114.2	6.98 (d , 2H , *J* = 8.8 Hz)	C7 , C9
3	126.7	7.30 (t , 1H , *J* = 7.4 Hz)	C4 , C8
4	126.8	7.56 (d , 2H , *J* = 7.3 Hz)	C3 , C7
5	128.2	7.53 (d , 2H , *J* = 7.3 Hz)	C8 , C9
6	128.7	7.41 (t , 2H , *J* = 7.9 Hz)	C4 , C7 , C8
7	133.8	-	-
8	141.0	-	-
9	159.1	-	-

Further confirmation of the data was provided by GC-EIMS. The total ion chromatogram (TIC) obtained for the GC trace is shown in Figure 4-5, while the mass spectrum collected for the main peak eluting at 22.6 min which is attributed to the product 4e' is shown in Figure 4.7. A number of small peaks are seen in the GC trace shown in Figure 4.6, though the peak at 22.6 min is found to be the main compound in the reaction.

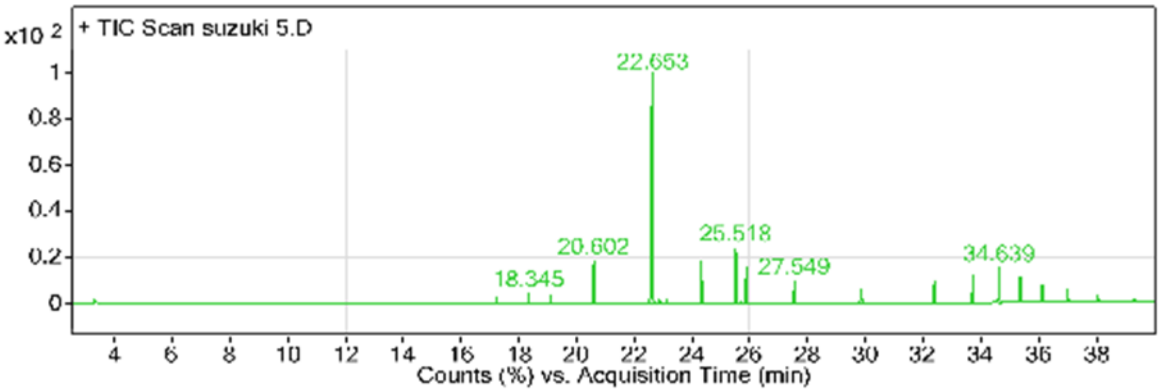

Figure 4-6 TIC chromatogram of 1-methoxy-4-phenyl-benzene synthesised using *Ulva* supported PdNPs.

The mass spectrum for compound 4e' is shown in Figure 4-7 with a base molecular ion at 184.2 amu which corresponds to the molecular mass expected for compound 4e'. Since EI-MS is not a soft ionization technique as the name implies (EI - electron impact), fragments are expected. The fact that the molecular ion is also the base peak indicates the stability of the compound.

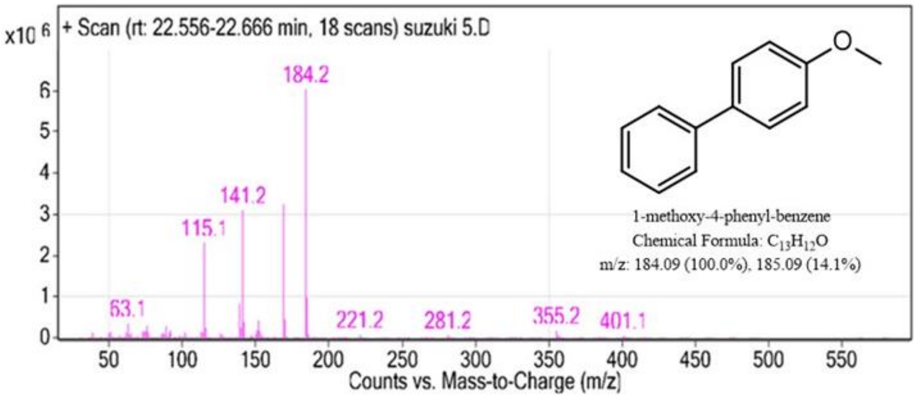

Figure 4-7 EI-MS spectrum of 1-methoxy-4-phenyl-benzene synthesised using *Ulva* supported PdNPs.

It is interesting to note that, under identical reaction conditions, both catalysts gave the product in a 75% yield Table 4-2. Thus, the successful formation of the compound in good yields was confirmed using NMR and GC-EIMS. This established the baseline for the remainder of the starting materials used Table 4-1 and the results obtained will be discussed in the following section.

4.4.2 Synthesis of a range of Suzuki-Miyaura products using the Ulva supported PdNPs and Pd/C catalysts

This section then focuses on the remaining substrates listed in Table 4.1 where two boronic acids (namely phenyl boronic acid and (4-hydroxymethylphenyl) boronic acid) and 2-iodo, 3-iodo and 4-iodoanisole as the aryl halides were used.

A observations in the NMR data that is of importance is the formation of a new carbon-carbon bond formed as well as the chemical shift for these carbons which are in the range of 130 ppm – 140 ppm for the ^{13}C data which is characteristic of quaternary carbons. One of the problems encountered in the structural elucidation of the compounds is the assignment of protons and carbons for the biaryl compounds 4-a, 4-a', 4-c, 4-c', 4-5e and 4-5e' as these are the compounds that do not contain the hydroxyl substituent group that is located at the para position relative to the new carbon-carbon coupling bond (as denoted by an (*) in . The signals that were difficult to differentiate are also shown.

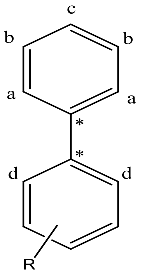

Figure 4-8 Biaryl compound consisting of proton and carbon signals that were problematic in assigning denoted (a, b, c, d and e) where R = C-O-CH3 (methoxy group).

The most important aid is the effect of the methoxy group on the aromatic ring system chemical shifts when the position is shifted relative to the new sp^2 hybridized carbon formed during the carbon-carbon coupling as denoted by a (*) in Figure 4-9 . The methoxy group has an electron donating mesomeric effect to the aromatic ring, where the methoxy moiety donates electrons into the benzene ring by resonance. This results in deshielded chemical shifts for the atoms ortho and para to the methoxy group .The methoxy groups' proton shift is relatively easy to differentiate and it is in the region of 1 ppm – 5 ppm, while carbon chemical shift is in the region of 50 ppm – 60 ppm for the para and ortho positions. Thus it was used as a starting point for all proton and carbon assignments since the methoxy group would be placed at either the para, meta and ortho position relative to the new carbon-carbon coupling bond.

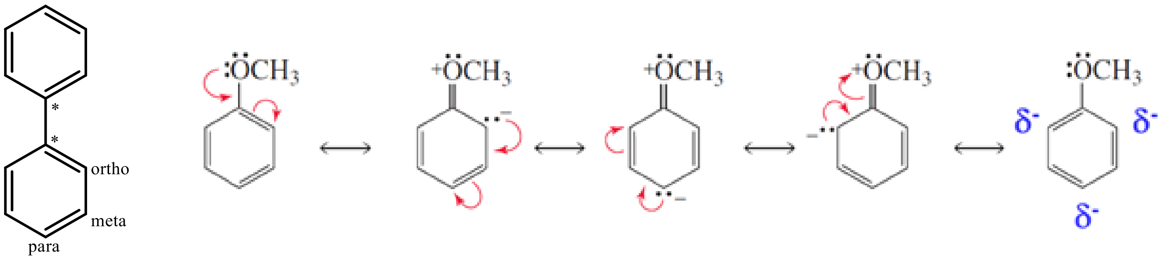

Figure 4-9 Structure of biaryl compound depicting substituent position relative to the carbon-carbon coupling bond and the electron donating resonance structures that the methoxy group possess.

The boronic acid ring system will be referred to as ring A, while the anisole contribution is referred to as ring B. To identify if the biaryl compounds where synthesised, the appearance of two new doublet signals in the proton spectrum of compound **4-e** and **4-e'** (1-methoxy-4-phenyl-benzene), the appearance of two new doublet and triplet signals in the proton spectrum of compound **4-a** and **4-a’** (1-methoxy-2-phenyl-benzene) and the appearance of a new singlet, two doublets and one triplet proton for compound **4-c** and **4-c’** (1-methoxy-3-phenyl-benzene) in ring B will confirm if the compounds were synthesised successfully. This is in addition to the characteristic methoxy singlet at ~3.8 ppm (ring B), as well as a doublet and a triplet signal which integrate to 2 protons and finally a triplet which integrates to 1H for (ring A). The latter signals for ring A is not expected to differ much to that of the model compound **4-e** and **4-e’** which was fully characterised in section 4.1.3.

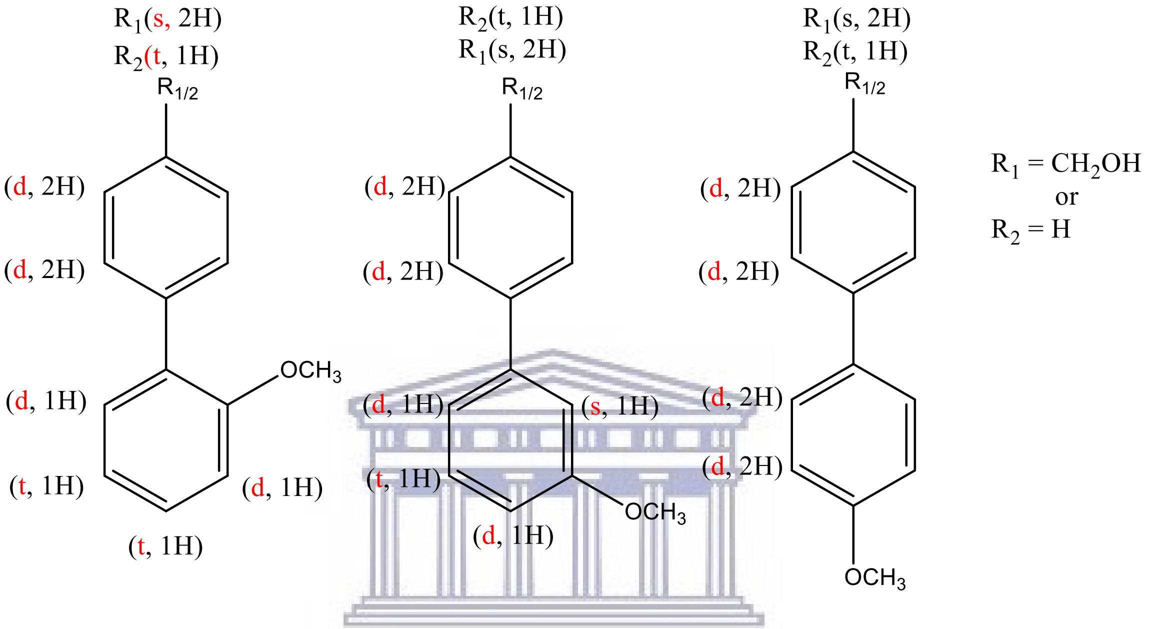

Compound:**4-a/4-a'** and **4-b/4-b'** Compound: **4-c/4-c'** and **4-d/4d'** Compound: **4-e/4-e'** and **4-f/4-f'**

Figure 4-10 The expected multiplicity and integration values of synthesised bi-aryl product.

For the hydroxylated compounds **4-b**, **4-b’**, **4-d**, **4-d’**, **4-f** and **4-f’** ([4-(2-methoxyphenyl) phenyl] methanol, [4-(3-methoxyphenyl) phenyl] methanol] and [4-(4-methoxyphenyl) phenyl]) this was not the case as there protons were clearly differentiated as little to no overlap was presented in the proton spectra.

DMF (dimethylformamide) and diethyl ether peaks are also observed in the ^{1}H and ^{13}C spectra. DMF has a δ_C at 31.5 ppm, 36.5 ppm and 162.6 ppm respectively. And δ_H at 2.76 (s), 2.88 (s) and 7.91 (s). Diethyl ether has δ_C shifts at 15.28 and 65.91 and δ_H at 1.21 (t) and 3.48 (q).

4.4.3 Conclusion

The NMR data for these compounds agreed with the expected product structures, where the requisite number of proton and carbon signals in the NMR spectra were accounted for as expected. In addition to this, characteristic signals for the methoxy carbon at δ_C ~55 were observed for all compounds, the CH_2OH moieties for compounds **4b/b’**, **4d/d’**, **4f/f’** in the proton and carbon spectra were observed at δ_H ~4.6-5.0 and δ_C 65, respectively. The disappearance of the =C-I signal in the ^{13}C spectra at approximately δ_C 85 – 100, is either significantly diminished (if there is some starting material remaining) or it has disappeared completely. The spectra for all these compounds are given in the Appendix and indexed alphabetically.

The spectra for compounds **4a** and **4a'** (Entry 1, Table 4.1) are very similar and it appears that there isomers may be present since some signals appear in duplicate e.g. the $O\underline{C}H_3$ signal at δ_C ~55 and the aromatic $=\underline{C}$-O signal at δ_C ~156. Bearing this in mind, the expected number of carbon signals (11) is present in the ^{13}C spectra of **4a** and **4a'**, with 3 quaternary, 7 aromatic methine and 1 methoxy carbons signals. A small amount of the aromatic $=\underline{C}$-I is however observed in the ^{13}C spectra at $\delta_{C\,\sim}$85 for both compounds. The ^1H NMR spectra for these compounds are also very similar, and these also show the possibility of isomers with the methoxy signal at δ_H 3.7. Nine aromatic protons are observed, with the methoxy signal integrating to 3 protons. The mass spectra obtained for these compounds **4.a/a'** using both the Pd/C commercial catalyst, as well as the *Ulva* supported PdNP catalyst, confirmed the successful formation of the expected products (experimental section 4.2.4), giving the expected molecular ions at *m/z* 184.2 for both compounds.

Compounds **4c** and **4c'** (Entry 3, Table 4.1) are very similar, with **4c** appearing slightly cleaner. The ^{13}C spectra reveal 11 carbon signals for **4c** and **4c'**, with 3 quaternary, 7 aromatic methines and 1 methoxy carbon signals. A small amount of the aromatic $=\underline{C}$-I is however observed in the ^{13}C spectra of compound **4c'** at $\delta_{C\,\sim}$85. The ^1H NMR spectra for these compounds are also very similar, with the characteristic methoxy signal resonating at δ_H 3.8. Nine aromatic protons are observed, with the methoxy signal integrating to 3 protons. The mass spectra obtained for these compounds **4c/c'** confirmed the successful formation of the products (experimental section 4.2.4), giving the expected molecular ions at *m/z* 184.2 for both compounds.

For the methanol substituted compounds **4b/b'**, **4d/4d'** and **4f/f'** (Entries 2, 4 and 6 respectively in Table 4.1), the ^1H and ^{13}C spectra are very similar, in that the only differences observed is due to the purity of the samples.

Some solvent signals are observed in the spectra of compounds **4b/b'** (Entry 2, Table 4.1) with the latter appearing slightly cleaner. The ^{13}C spectra reveal 12 carbon signals for **4b** and **4b'**, with 4 quarternary, 6 aromatic methine, 1 methylene and 1 methoxy carbon signals. The characteristic methoxy, methylene ($\underline{C}H_2OH$) and aromatic =C-O carbon signals are observed at δ_C 55, 65 and 156, respectively. A small amount of the aromatic $=\underline{C}$-I signal pertaining to the starting material is however observed in the ^{13}C spectra of both compounds at $\delta_{C\,\sim}$85. The ^1H NMR spectra for these compounds are also very similar, with the characteristic methoxy signal resonating at δ_H 3.8 and the characteristic methylene ($C\underline{H}_2OH$) signal residing at δ_H 4.6. Eight aromatic protons are observed, with the methoxy and methylene signals integrating to 3 and 2 protons. The mass spectra obtained for these compounds **4b/b'** confirmed the successful formation of the products (experimental section 4.2.4), giving the expected molecular ions at *m/z* 214.2 for both compounds.

The spectra of compounds **4d/d'** (Entry 4, Table 4.2) reveal the expected number of ^{1}H and ^{13}C signals. However, some starting material signals, together with solvent signals result in unnecessarily complicated spectra particularly with this compound set. Twelve carbon signals are observed in the ^{13}C spectra for **4d** and **4d'**, with 4 quaternary, 6 aromatic methine, 1 methylene and 1 methoxy carbon signals. The characteristic methoxy, methylene ($\underline{C}H_2OH$) and aromatic =C-O carbon signals are observed at δ_C 55, 64 and 160, respectively. A small amount of the aromatic =$\underline{C}$-I signal pertaining to the starting material is however observed in the ^{13}C spectra of both compounds at $\delta_{C\sim}$85. The ^{1}H NMR spectra for these compounds are also very similar, with the spectra for **4d** appearing slightly cleaner. The characteristic methoxy signal resonating at δ_H 3.7 and the characteristic methylene ($C\underline{H}_2OH$) signal residing at δ_H 4.6 was once again observed in the ^{1}H NMR spectra for these compounds. Eight aromatic protons are observed, with the methoxy and methylene signals integrating to 3 and 2 protons. The mass spectra obtained for these compounds **4d/d'** confirmed the successful formation of the products (experimental section 4.2.4), giving the expected molecular ions at *m/z* 214.2 for both compounds.

Starting materials and solvent signals again complicated the analyses of the spectra for compounds **4f/f'** (Entry 6, Table 4.2). However, the expected number of ^{1}H and ^{13}C signals is observed. Ten carbon signals are observed in the ^{13}C spectra for **4f** and **4f'**, with 4 quaternary, 4 aromatic methine, 1 methylene and 1 methoxy carbon signals. The characteristic methoxy, methylene ($\underline{C}H_2OH$) and aromatic =C-O carbon signals are observed at δ_C 55, 65 and 158, respectively. The ^{1}H NMR spectra for these compounds are also very similar, with aromatic protons residing in the same region i.e. between δ_H 6.50-7.40 (integrating to 8 protons). This is expected as the molecule is highly symmetrical with 4 chemically equivalent sites. The characteristic methoxy signal resonating at δ_H 3.8 and the characteristic methylene ($C\underline{H}_2OH$) signal residing at δ_H 4.7 was once again observed in the ^{1}H NMR spectra for these compounds. The methoxy and methylene signals integrate to 3 and 2 protons, respectively. The mass spectra obtained for these compounds **4d/d'** confirmed the successful formation of the products (experimental section 4.2.4), giving the expected molecular ions at *m/z* 214.2 for both compounds.

The % yields obtained for the products varied between 55 and 75%, with the Pd/C catalyst performing slightly better in some instances (Table 4.2.4). These were for the entries 1 – 4, while the remainder were found to be on par. This may be due to the fact that the %Pd loading on the *Ulva* supported catalyst was 8% while that for the commercially available Pd/C catalyst the Pd loading is 10%.

Chapter 5 Conclusion and future work

5.1 Conclusion

As we search for potential materials for the greater tomorrow, it is of utmost importance to do so in a most sustainable method. Therefore we need to employ green synthetic or biomimetic methods in the synthesis of such materials. Terrestrial sources as well marine sources have been used to find potential sources, extracts be it organic or aqueous has been studied extensively, thus an alternative method which utilizes a live seaweed, as presented in this paper is needed. The use of live *Ulva armoricana* were used to produce PdNPs which was used in a series of Suzuki-Miyaura carbon-carbon coupling reaction.

Live *Ulva armoricana* was able to reduce Pd^{2+} to Pd^{0}. The production and characterization of PdNPs followed by the application of these nanoparticles in a series of Suzuki-Miyaura carbon-carbon coupling reactions was demonstrated. To obtain the UV-Vis data, a baseline for the peaks of a Pd^{2+} solution was first established and was absorbance of 207 nm and 242 nm was established. Unfortunately there was no evident change in color the reduction process of palladium as is typically observed in the reduction of gold. It was observed that the absorbance at 242 nm decreases with time, while the absorbance at 207 nm increases, these changes occurred within the first 5 min after the introduction of *Ulva armoricana* into the K_2PdCl_4 solution. The TEM and HR-TEM images provided insight into the morphology and average nanoparticle size, where the 0.5 mM Pd sample was used as it showed superior consistency in its UV-Vis data. The shape of the nanoparticles was found to be spherical with an average size of 7 nm. The EDX also confirmed the composition of PdNPs showing traces of sea salt; ie magnesium, potassium and chlorine. The zeta potential measurements for the PdNPs was recorded as -34.4 mV and – 16.9 mV in ethylene glycol and diethyl ether solutions respectively, thus the particles was determined to be relatively stable in ethylene glycol. DLS analyses showed that the PdNPs size was 103 nm in diethyl ether and 1696 nm in ethylene glycol. These solvents where chosen based on their ability to dissolve the *Ulva* supported PdNPs. The XRD data yielded an unexpected result, during the first XRD, analyses PdO NPs was produced and this could be due to the interaction between Pd^{2+}/Pd^{o} and oxygen during the ashing step which occurred at 800 ^{o}C at a ramp rate of 1 ^{o}C/min under air. The second set of XRD data showed PdNPs with the characteristic powder diffraction pattern for (fcc) face centred cubic crystal phase. The particle size was calculated using the Debye-Scherrer equation and was found to be 2.7 nm. The FT-IR spectrum of the aqueous extract, *Ulva* supported PdNPs, *Ulva* containing no Pd and commercially available 10% wt Pd/C catalyst. The aqueous extract yielded significant stretches in the FT-IR spectrum a C-O which is indicative of a secondary alcohol above 1600 cm^{-1} and a stretch of 738 cm^{-1} which could be a mono substituted phenyl group. The FT-IR spectrum with no Pd had a stretch at 880 cm^{-1} which indicates a presence of an aromatic C-H stretch. It also displayed numerous aromatic in place and out of plane aromatic stretches. The *Ulva* containing Pd had the exact same spectrum as the *Ulva* containing no Pd. However the 10% Pd/C had numerous stretches in the alkenyl region and a broad 3640 cm^{-1} stretch displaying the hydroscopic nature of the powder. The ICP-AES data revealed the Pd loading on *Ulva armoricana* supported to be 8%. TGA data of air dried *Ulva*, ashed *Ulva* with no Pd and ashed *Ulva* with Pd was obtained. These samples were subjected to a maximum temperature of 800 ^{o}C and a heating rate 20 ^{o}C/min. None of the samples reached zero mass percentage, however, the sample containing the Pd had the highest mass percentage remaining. This could be due to the presence of sea salt, but this was not exhibited in the XRD spectrum.

The next part of the research project was the application of the *Ulva* supported PdNPs on a series of Suzuki-Miyaura carbon-carbon coupling reactions. In total 12 biaryl compounds were synthesised (3 biaryl compounds and 3 methanol substituted biaryl compounds). Six compounds were synthesised using a commercial 10% wt Pd/C and 6 using *Ulva* supported PdNPs. The 10% wt Pd/C was used to compare the capability of the *Ulva* supported PdNPs. The percentage yield of the two catalyst were close though the commercial catalyst had a slightly higher percentage yield overall. The samples was subjected to NMR studies, as well GC-EIMS and fully characterised. All of the compounds were presented as coloured oil except compound **4-e** and **4-e'** which presented themselves as white powders. One of the problems encountered in the structural elucidation of the compounds was the assignment of protons and carbons for the biaryl compounds **4-a**, **4-a'**, **4-c**, **4-c'**, **4-e** and **4-e'** as these are the compounds that do not contain the hydroxyl substituent group that is located at the *para* position relative to the new carbon-carbon coupling bond. They exhibited highly overlapped proton spectra especially in the aromatic region but this was later resolved by purification as well as HSQC NMR experiments. The remaining products ie the methanol substituted compounds **4-b**, **4-b'**, **4-d**, **4-d'**, **4-f** and **4-f'** showed protons that were clearly differentiated, as little to no overlap was presented in the proton spectra. Another important observation in the NMR data that is the formation of a new carbon-carbon bond formed as well as the chemical shift for these carbons which are in the range of 130 ppm – 140 ppm for the ^{13}C data which is characteristic of quaternary carbons. The proton and carbon spectra are given in the Appendix section for these compounds. GC-EIMS analysis was not performed on these compounds.

5.2 Future work

The synthesis of PdNPs was carried out using the live seaweed *Ulva armoricana*, thus bringing about the question of how the nanoparticles are produced by the seaweed and other marine organisms, and whether this is specific to only one type of seaweed. It is clear that the Pd metal salt is taken up by the seaweed since it is toxic and it is therefore reduced to it's the metallic state (PdNPs). It is believed that the PdNPs formed on the *Ulva* thallus surface, in the chloroplasts and cell walls of *Ulva* as shown by (Mukhuro *et al*. 2018 using AuNPs), and it is therefore important to isolate the various cellular components to confirm the mechanism of formation of the PdNPs.

The PdNPs produced using *Ulva armoricana* was also able to match the catalytic ability of the commercial 10% wt Pd/C, thus the study opens the door to the application of bio-synthesised nanoparticles. The PdO produced could also be used as a Lindlar catalyst for the reduction of triple bonds.

A future study would be to do an organic and aqueous extraction and subject these extracts to HPLC and isolate individual compounds to perform numerous NMR techniques to structurally elucidate these compounds and screen the for reducing capability. The nanoparticles produced can be applied to a variety of reactions such as Heck, Stille, Kumada, Negishi, Sonogashira and several other carbon-carbon coupling reactions.

Another question that can be asked is if *Ulva* armoricana is able to reduce other metal salts such as Pt, Cu, Au, Ag, Ni and Rh. These NPs can then be assessed for their applications in catalysis, biological application such as antifungal and antifouling.

The study now provides some insight into the capability of using live seaweed as a potential bio-factory to produce nanoparticles.

References

Adams, N. M. (1994) Seaweeds of New Zealand. An Illustrated Guide. Canterbury University Press, Christchurch, New Zealand.

Astruc D and M.-C. Daniel (2004). “Gold nanoparticles: assembly, supramolecular chemistry, quantum-size-related properties, and applications toward biology, catalysis, and nanotechnology,” *Chem Rev*, **104**:293–346.

Aiken III J. D. and Finke R. G (1999).Catalytically Active Transition-Metal Nanoclusters Prepared in Solution; *J. Mol. Catal*. **145** :(1–2), 1.

Amendola V& Meneghetti M (2009). Size Evaluation of Gold Nanoparticles by UV−vis Spectroscopy; *J. Phys. Chem*; **113**(11):4277–4285.

Anderson, R. J., Levitt. G. J. and Share, A. (1996) Investigations for the mariculture of Gracilaria gracilis at Saldanha Bay, South Africa. *J Appl Phycol*; **8**: 421 -430.

Arockiya Aarthi Rajathi F, Parthiban C, Ganesh Kumar V, and Anantharaman P (2012). “Biosynthesis of antibacterial gold nanoparticles using brown alga, Stoechospermum marginatum (k¨utzing),”. *Spectrochimica Acta - Part A: Molecular and Biomolecular Spectroscopy;* **99**:166–173.

Beach, K. S., Smith, C. M., Michael, T. and Shin, H (1995). Photosynthesis in reproductive unicells of Ulva fasciata and Enteromorpha flexuosa: implications for ecological success. *Mar Ecol Prog Ser*; **125**: 229 – 237.

Beccalli, E. M.; Broggini, G.; Martinelli, M.; Sottocornola (2007). C−C, C−O, C−N Bond Formation on sp2 Carbon by Pd(II)-Catalyzed Reactions Involving Oxidant Agents, S. Chem. Rev; 107:5318–5365.

Biazar J. Ai, E., Jafarpour M *et al* (2012).“Nanotoxicology and nanoparticle safety in biomedical designs,”. *Int J Nanomedicine*; **6**:1117–1127.

Blomster, J. and Stanhope, M. J. (1998) Molecular and morphological analysis of Enteromorpha intestinalis and E. compressa (Chlorophyta) in the British Isles. *J Appl Phycol*; **34**: 319–340.

Bogunia-Kubik K and Sugisaka M (2002).“From molecular biology to nanotechnology and nanomedicine,”. *BioSystems*; **65**:123–138.

Bolton, J.J. (1986) Marine phytogeography of the Benguela upwelling region on the west coast of southern Africa: a temperature dependent approach. *Bot Marina;* **29**: 251–256.

Bolton, J. J., Robertson-Andersson, D. V., Shuuluka, D. and Kandjengo, L. (2008) Growing Ulva (Chlorophyta) in integrated systems as a commercial crop for abalone feed in South Africa: a SWOT analysis. *Journal of Applied Phycology*, DOI 10.1007/s10811-008-9385-6.

Borchert H, Shevchenko EV, Robert A, Mekis I, Kornowski A, Grübel G & Weller H (2005). Determination of nanocrystal sizes: a comparison of TEM, SAXS, and XRD studies of highly monodisperse CoPt3 particles. *Langmuir*; **21**(5):1931-6.

Brar SK & Verma M (2011). Measurement of nanoparticles by light-scattering techniques. *TrAC Trends Anal Chem*; 30:4–17.

Breeman, A. M. (1988). Relative importance of temperature and other factors in determining geographic boundaries of seaweeds: experimental and phonological evidence.*Helgolander Messresuntersuchungen*; **42**: 199 – 241.

Buchwald, S. L.; Mauger, C.; Mignani, G.; Scholz, U (2006). Palladium-Catalyzed Amination of Unprotected Halo-7-azaindoles. *Adv. Synth. Catal*. 348:23–39.

Cantor CR & Schimmel PR (1980). Techniques for the study of biological structure and function. San Francisco: W. H. Freeman.

Centomo P , Corain B, Jerabek K and Canton P (2004). A mild route to solid-supported rhodium nanoparticle catalysts and their application to the selective hydrogenation reaction of substituted arenes , *Angew. Chem. Int. Ed*; **43**(8), 959.

Chauhan A & Chauhan P (2014). Powder XRD Technique and its Applications in Science and Technology. *Anal Bioanal Tech*; **5**(212):1-5.

Chauhan B. P. S, Rathore J. S and Bandoo T J (2004). "Polysiloxane-Pd" nanocomposites as recyclable chemoselective hydrogenation catalysts. *Am.Chem. Soc*; **126**, (27), 8493

Chen W, Davies J. R., Ghosh D, Tong M C, Konopelski J.P and Chen S (2006), Identification of the formation of metal–vinylidene interfacial bonds of alkyne-capped platinum nanoparticles by isotopic labelling. *Chem. Mater*; **18**, (22), 5253.

Coats AW & Redfern JP (1963). Thermogravimetric analysis. A review. *Analyst*; 88: 906-924.

Cookson, B. J. (2012). The Preparation of Palladium. *Platinum Met Rev*; **2**: 83–98.

Darcy-Vrillon B (1993). Nutritional aspects of the developing use of marine macroalgae for the human food industry. *Int J Food Sci Nutr*; **44**:S23–S35.

Davies, K. M. (2004). Plant pigments and their manipulation. *Annual Plant* Reviews Vol 12,ed. Oxford/Boca Raton: Blackwell Publishing/CRC Press, Boca Raton. 352 pp.

Dawes, C. J. (1995). Suspended cultivation of Gracilaria in the sea. *J Appl Phycol*; **7**(3): 303 – 313.

Dickinson, C. I. (1963). British Seaweeds. Frome. Londen.

Dion, P.&le Bozec, S. (1996). The French Atlantic Coasts. In Marine Benthic Vegetation : Recent Changes and the Effects of Eutrophication (Schramm, W. & Nienhuis, P.H., editors), 251±264. *Ecological Studies* 123. Springer- Verlag, Berlin.

Douglas KR & Tyla SF (2010). Transmission electron microscopy of cartilage and bone. *Methods Cell Bio*; **96**:443-473.

El-Rafie, M. H and Zahran M. K (2013).“green synthesis of silver nanoparticles using polysaccharides extracted from marine macro algae,” *Carbohydr Polym*; **96**(2):403–410.

Eroglu E, Chen X, Bradshaw M *et al*. (2013). “Biogenic production of palladium nanocrystals using microalgae and their immobilization on chitosan nanofibers for catalytic applications,” *RSC Advances*; **3**:1009–1012,.

Faraday M, *Phil. Trans. Roy. Soc*., 1857, 147, 145.

Feldheim DL & Colby A Jr (2002). Metal Nanoparticles: Synthesis, Characterization, and Applications. CRC Press, Boca Raton, FL.

El Gamal A.A (2010), “Biological importance of marine algae,” *Saudi Pharm J*; **1**: 1–25.

Ganesan M, Freemantle RG, Obare SO (2007). Monodisperse thioether-stabilized palladium nanoparticles: synthesis, characterization, and reactivity. *Chem Mater*; **19**(14):3464–3471. doi: 10.1021/cm062655q.

Gautam A and Van Veggel F. C. J. M. (2013) , "Synthesis of nanoparticles, their biocompatibility, and toxicity behavior for biomedical applications," *J Materials Chem B*, 1:5186–5200.

Golding CG, Lamboo LL, Beniac DR & Booth TF (2016). The scanning electron microscope in microbiology and diagnosis of infectious disease. *Sci. Rep*; **6**(26516):1-8.

Goldstein JI, Newbury DE, Echlin P, Joy DC, Romig Jr AD, Lyman CE, Fiori C & Lifshin E (1992). Scanning Electron Microscopy and X-ray Microanalysis. 2nd ed, New York: Plenum Pres; 820.

Guzzinati G, Clark L, Béché A, Juchtmans R , Van Boxem R, Mazilu M & Verbeeck J (2015). Prospects for versatile phase manipulation in the TEM: Beyond aberration correction. *Ultramicroscopy*; **151**:85–93.

Hanada N, Hirotoshi E, Chikawa T, Akiba E & Fujii H (2008). SEM and TEM characterization of magnesium hydride catalyzed with Ni nano-particle or Nb2O5. *J. Alloy Comp*; 450:395-399.

Hayden, H. S., Blomster, J., Maggs, C. A., Silva, P. C., Stanhope M. and Waaland J. R. (2003). Linnaeus was right all along: Ulva and Enteromorpha are not distinct genera. *Euro J Phycol*, **38**: 277-294.

Hind AR, Bhargava SK & McKinnon A (2001). At the solid/liquid interface: FTIR/ATR—the tool of choice. *Adv Colloid Interface Sci*; **93**:91–114.

Hoek sema, B. W. and van den Hoek, C. (1983). The taxonomy of Ulva (Chlorophyceae) from the coastal region of Roscoff (Brittany, France). *Bot Marina*; **26**: 65 – 86.

Hou Z, Theyssen N, Brinkmann A and Leitner W (2005), Advanced Fluids for Preparation and Application of Catalytically Active Nanoparticles, *Angew. Chem. Int. Ed.,44*, (9), 1346.

Howe JM, Mori H & Wang ZL (2008). In situ high-resolution transmission electron microscopy in the study of nanomaterials and properties. *Mat Res Bull*; **33**(2):115–121.

Huang X, P. K. Jain, I. H. El-Sayed, and M. A. El-Sayed (2006), "Determination of the minimum temperature required for selective photothermal destruction of cancer cells with the use of immunotargeted gold nanoparticles," *Photochemistry and Photobiology*, **82**:412–417, 2006.

Huc, V., and K. Pelzer (2008): A new specifically designed calix[8]arene for the synthesis of functionalized, nanometric and subnanometric Pd, Pt and Ru nanoparticles. In: *Journal of Colloid and Interface Sci;* **318**(1)1-4.

Hunter RJ (2001). Foundations of colloid science. 2nd ed. Oxford: Clarendon Press.

Huang H & Yang X (2004). Synthesis of polysaccharide-stabilized gold and silver nanoparticles: a green method. *Carbohydr Res*; **339**(15):2627–2631.

Huang X, P. K. Jain, I. H. El-Sayed, and M. A. El-Sayed (2006),"Determination of the minimum temperature required for selective photothermal destruction of cancer cells with the use of immunotargeted gold nanoparticles," *Photochem and Photobiol*; **82**:412–417.

Iravani S (2011), "green synthesis of metal nanoparticles using plants," *green Chem*; **13**:2638–2650,.

Ishizuka H, Tano T, Torigoe K, Esumi K and Meguro K (1992), Preparation of monodispersed colloidal gold by reduction of AuCl−4—cationic surfactant complexes, *Colloids Surf*; 63(3–4):337.

Jiao G, Yu G, Zhang J & Ewart HS (2011). Chemical Structures and Bioactivities of Sulfated Polysaccharides from Marine Algae. *Mar Drugs*; **9**:196-223.

Johal MS (2011). Understanding nanomaterials. Boca Raton: CRC Press

Kannan R. R , Arumugam R, Ramya D, Manivannan K, and Anantharaman P (2013). "green synthesis of silver nanoparticles using marine macroalga Chaetomorpha linum," *Applied Nanoscience*, 3:229–233.

Kathiresan K, Manivannan S, Nabeel M & Dhivya B (2009). Studies on silver nanoparticles synthesized by a marine fungus, Penicillium fellutanum isolated from coastal mangrove sediment. *Colloids Surf B*; **71**(1):133–137.

Kazarian SG & Chan KL (2006). Applications of ATR–FTIR spectroscopic imaging to biomedical samples. *Biochim Biophys Acta*; **1758**:858–867.

Kishi Y (1989). Synthesis of Palytoxin from Palytoxin Carboxylic Acid, *J. Am. Chem. Soc*; 116 (24):11205-11206

Kim SW, Park J, Jang Y, Chung Y, Hwang S, Hyeon T (2003),Synthesis of monodisperse palladium nanoparticles. Nano Lett.;**3**(9):1289–1291. doi: 10.1021/nl0343405.

Kumar P, Senthamil Selvi S, and Govindaraju M (2013), "Seaweed mediated biosynthesis of silver nanoparticles using Gracilaria corticata for its antifungal activity against Candida spp.," *Applied Nanoscience*; **3**:495–500,.

Lahaye M & Ray B (1996). Cell-wall polysaccharides from the marine green alga Ulva rigida (Ulvales, Chlorophyta)-NMR analysis of ulvan oligosaccharides. *Carbohydr Res*; **283**:161–173.

Lahaye M & Ray B (1996). Cell-wall polysaccharides from the marine green alga Ulva rigida (Ulvales, Chlorophyta)-NMR analysis of ulvan oligosaccharides. *Carbohydr Res*; **283**:161–173.

Lahaye M & Robic A (2007). Structure and functional properties of ulvan, a polysaccharide from green seaweeds. *Biomacromol*; **8**:1765–1774.

Lavanya R & Veerappan N (2011). Antibacterial potential of six seaweeds collected from gulf of mannar of southeast coast of India. *Adv Biol Res*; **5**:8-44.

Lee S-Y , Yamada M and Miyake M (2005) Synthesis of carbon nanotubes and carbon nano filaments over palladium supported catalysts, *Sci Tech Adv Mat*, **6**:5, 420-426.16.

Li Z, Gao J, Xing X, Wu S, Shuang S, Dong C, M. C. Paau and M. M. F. Choi, J (2011) Synthesis and Characterization of n-Alkylamine-Stabilized Palladium Nanoparticles for Electrochemical Oxidation of Methane. *Phys. Chem.* C; **2114**(2):723.

Lignell, A., Ekman, P. and Pedersén, M. (1987) Cultivation technique for marine seaweeds allowing controlled and optimized conditions in the laboratory and on a piolet scale. *Botanica Marina*; **30**: 417 – 424.

Liu H & Webster TJ (2007). Nanomedicine for implants: a review of studies and necessary experimental tools. *Biomaterials*; **28**:354–369.

Liu ZL, Deng JC, Deng JJ & Li FF (2008). Materials Science and EngineeringB-Advanced Functional Solid-State Materials; Fabrication and photocatalysis of CuO/ZnO nano-composites via a new method. *Mat Sci Eng B*; **150**:99-104.

Lobban, C. S. and Harrrison, P. J. (eds.) (1997). Seaweed ecology and physiology. Cambridge University Press. Cambridge. 366 pg.

Lu F, Ruiz J and Astruc D (2004). Palladium–dodecanethiolate nanoparticles as stable and recyclable catalysts for the Suzuki–Miyaura reaction of aryl halides under ambient conditions , *Tetrahedron Lett;* **45**(51):9443

Lüning, K., Kadel, P. and Pang, S. (2008). Control of reproduction rhythimicity by environmental and endogenous signals in Ulva pseudocurvata (Chlorophyta). *J Phyco*; **44**(4): 866-873.

Mahdavi M, Namvar F, Ahmad MB & Mohamad R (2013). green biosynthesis and characterization of magnetic iron oxide (Fe_3O_4) nanoparticles using seaweed (Sargassum muticum) aqueous extract. *Molecules*; **18**(5):5954-5964.

Makarov VV, Love AJ, Sinitsyna OV, Makarova SS, Yaminsky IV, Taliansky ME & Kalinina NO (2014). green Nanotechnologies: Synthesis of Metal Nanoparticles Using Plants. *Acta naturae*; **6**(1):35-44.

Manchu N, Melpha Y & James JE (2014). Phytochemical investigation of three species of Ulva from Rasthacaud Coast, Tamil Nadu. *India J Chem and Pharm Res*; **6**(8):570-574.

Martins AF, Facchi SP, Monteiroa JP, Nocchi SR, Silva CT, Nakamura CV, Girotto EM, Rubira AF & Muniz AC (2015). Preparation and cytotoxicity of N,N,N-trimethyl chitosan/alginate beads containing gold nanoparticles. *Int J Biol Macromol*; **72**:466-471.

Mazumder V and Sun S (2009) Oleylamine-Mediated Synthesis of Pd Nanoparticles for Catalytic Formic Acid Oxidation , *J. Am. Chem. Soc*.;131(13):4588.

McClenathan DM, Wetzel WC, Lorgea SE & Hieftje GM (2006). Effect of the plasma operating frequency on the figures of merit of an inductively coupled plasma time-of-flight mass spectrometer. *J Anal At Spectrom*; **21**:160-167.

McDonald KL (2009). A review of high-pressure freezing preparation techniques for correlative light and electron microscopy of the same cells and tissues. *J. Microscopy*; 235:273-281.

Menard LD, Gao SP, Xu H, Twesten RD, Harper AS, Song Y, Wang G, Douglas AD, Yang JC, Frenkel AI, Nuzzo RG & Murray RW (2006). Sub-Nanometer Au Monolayer-Protected Clusters Exhibiting Molecule-like Electronic Behavior: Quantitative High-Angle Annular Dark-Field Scanning Transmission Electron Microscopy and Electrochemical Characterization of Clusters with Precise Atomic Stoichiometry. *J Phys Chem B*; **110**:12874-12883.

Miyaura, N, Suzuki A (1995). Palladium-Catalyzed Cross-Coupling Reactions of Organoboron Compounds . *Chem. Rev*; **95**(7):2457–2483.

Mohanpuria P, N. K. Rana, and S. K. Yadav (2008). "Biosynthesis of nanoparticles: technological concepts and future applications," *J Nanopart Res*; **10**:507–517.

Moores A and Goettmann F (2006). The plasmon band in noble metal nanoparticles: an introduction to theory and applications , *New J. Chem*; **8**:1121

Mukhoro O C , Roos W D , Mohammed Jaffer , Bolton J. J , Stillman M. J , Beukes D , Antunes E.(2018) using green alga Ulva lactuca and evaluation of their catalytic.*Chem-A Euro J;* **24**(7),1657.

Naiwa H. S (2000), Handbook of Nano structural Material and Nanotechnology, Academic Press, New York, NY, USA, 2000.

Negishi, E (2002). Handbook of Organopalladium Chemistry for Organic Synthesis., Ed.; Wiley-Interscience: New York, 2002.

Nikolaisen L, Jensen PD, Bech KS, Dahl J, Busk J, Brødsgaard T, Rasmussen MB, Bruhn A, Bjerre A , Bangsøe Nielsen HB, Albert KR, Ambus P, Kadar Z, Heiske S, Sander B & Schmidt ER (2011). Energy Production from Marine Biomass (Ulva lactuca). PSO Project No. 2008-1-0050. Danish Technological Institute, Denmark.

Orbaek A & Barron AR (2014). ICP-AES analysis of nanoparticles http//cnx.org/content/m22058/1.20.

Pal S, Tak YK & Song JM (2007). Does the antibacterial activity of silver nanoparticles depend on the shape of the nanoparticle? A study of the gram-negative bacterium Escherichia coli. Appl. Environ. Microbiol; **73**(6):1712–1720.

Parker HL, Rylott EL, Hunt AJ, Dodson JR, Taylor AF, Bruce NC & Clark JH (2014). Supported Palladium Nanoparticles Synthesized by Living Plants as a Catalyst for Suzuki-Miyaura Reactions. PLOS One; **9**(1): e87192 (6 pages)

Pons T, Uyeda HT, Medintz IL & Mattoussi H (2006). Hydrodynamic dimensions, electrophoretic mobility, and stability of hydrophilic quantum dots. *J Phys Chem B*; **110**:20308–20316.

Percival E & McDowell RH (1967). Chemistry and Enzymology of Marine Algal Polysaccharides; Academic Press: New York, NY, USA, 219.

Rosenauer A, Krause FF, Müller K, Schowalter M & Mehrtens (2014). Conventional Transmission Electron Microscopy Imaging beyond the Diffraction and Information Limits. *Phys Rev Lett*; **113**:96-101.

Rothman, M. D., Anderson, R. J., Share, A. and Drummond, H. (2006) Harvesting of the kelp Ecklonia maxima in South Africa affects its three obligate, red algal epiphytes. *J Phycol*; **18**: 343 – 349.

Ruska E & Knoll M (1931). Die magnetische Sammelspule für schnelle Elektronenstrahlen. (The magnetic concentrating coil for fast electron beams.). *Z. Tech. Phys*; **12**:389-400.

Tarakeshwar P and Kim N D. (2005), Modulation of the Electronic Structure of Semiconducting Nanotubes Resulting from Different Metal Contacts, *J. Phys. Chem. B*; **109**(16):7601.

Taskin E, Ozturk M, Taskin E & Kurt O (2007). Antibacterial activities of some marine algae from the Aegean Sea (Turkey). *Afr J Biotechnol*; **6**(24):2746-2751.

Tikhonov NA, Arkhangelsky IV, Belyaev SS & Matveev AT (2009). Carbonization of polymeric nonwoven materials. *Thermochimica Acta*; **486**:66–70.

Toshima N and Yonezawa T (1998), Bimetallic nanoparticles—novel materials for chemical and physical applications , *New J. Chem*.,(11), 1179

Troell, M., Robertson-Andersson, D. V., Anderson, R.J., Bolton, J. J., Maneveldt, G.,Halling C. and Probyn, T. (2006) Abalone farming in South Africa: An overview with perspectives on kelp resources, abalone feed, potential for on-farm seaweed production and socio-economic importance. *Aquaculture*; **257**(1-4): 266-281.

Trono Jr GC (1999). Diversity of the seaweed flora of the Philippines and its utilization. *Hydrobiologia*; **398**(399):1-6.

Tsunoyama H, Sakurai H, Ichikuni N, Negishi Y, and Tsukuda T (2004), Colloidal Gold Nanoparticles as Catalyst for Carbon-Carbon Bond Formation: Application to Aerobic Homocoupling of Phenylboronic Acid in Water, *Langmuir (Letters)*, **20**, 11293-11296.

Shah M, Fawcett D, Sharma S, S. K. Tripathy, and G. E. J. Poinern (2015), "green synthesis of metallic nanoparticles via biological entities," *Materials*,**8**:7278–7308.

Salt DE, Blaylcock M, Kumer NPBA, Dushenkov V, Ensley BD, et al. (1995) Pytoremediation: a novel strategy for the removal of toxic metals from the environment using plants. *Nat Biotechnol*; **13** 468–474.

Sangeetha N and Saravanan K (2014), "Biogenic silver nanoparticles using marine seaweed (Ulva lactuca) and evaluation of its antibacterial activity,".*J Nanosci*, 99–102,.

Sapsford KE, Tyner KM, Dair BJ, Deschamps JR & Medintz IL (2011). Analyzing nanomaterial bioconjugates: a review of current and emerging purification and characterization techniques. *Anal Chem*; 83:4453–4488.

Saritha K, Mani AE, Priyalaxmi M & Patterson J (2013). Antibacterial Activity and Biochemical Constituents of Seaweed Ulva lactuca.*J Pharmacol*; **7**(3):276-282.

Scheuer PJ (1990). Some marine ecological phenomena: chemical basis and biomedical potential. *Science*; **248**:173-177.

Scarano G and Morelli E (2003), "Properties of phytochelatin-coated CdS nanocrystallites formed in a marine phytoplanktonic alga (Phaeodactylum tricornutum, Bohlin) in response to Cd,". *Plant Science*;**165**:803–810.

Sharma A, Sharma S, Sharma K, Chetri SPK, Vashishtha A, Singh P, Kumar R, Rathi B & Agrawal R (2016). Algae as crucial organisms in advancing nanotechnology: a systematic review. *J Appl Phycol*; **28**:1759–1774.

Shem PM, Sardar R & Shumaker-Parry JS (2009). One-step synthesis of phosphine-stabilized gold nanoparticles using the mild reducing agent 9-BBN. *Langmuir*; **25**:13279-13283.

Singaravelu G, Arockiamaryc JS, Kumarb VG & Govindaraju K (2007). A novel extracellular synthesis of monodisperse gold nanoparticles using marine alga, Sargassum wightii Greville. Colloids and Surfaces B: *Biointerfaces*; **57**:97–101.

Siddhanta AK, Mody KH, Ramavat BK, Chauhan VD, Garg HS, Goel AK, Doss MJ, Srivastava MN, Patnaik GK & Kamboj VP (1997). Bioactivity of marine organisms: Part VIII-Screening of some marine flora of western coast of India. Indian J. Exp. Biol; **35**:638-643.

Silva, P. C., Basson, P. W. and Moe, R. L. (1996). Catalogue of the benthic Marine algae of the Indian Ocean. University of California Press. Berkeley.

Singaravelu G, Arockiamaryc JS, Kumarb VG & Govindaraju K (2007). A novel extracellular synthesis of monodisperse gold nanoparticles using marine alga, Sargassum wightii Greville. Colloids and Surfaces B: *Biointerfaces*; **57**:97–101.

Smit AJ (1997) Optimising Gracilaria verrucosa production in a laboratory based culture system. MSc Dissertation, University of Port Elizabeth, Port Elizabeth, South Africa.

Sobol M (2010). Comparasion methods of high-pressure freezing and automated freeze-substitution of suspension cells combined with LR-White embedding. *Histochem Cell Bio*; **134(**6):631-641.

Stalin Dhas T,Ganesh Kumar V, Abraham L. S, V. Karthick, and Govindaraju K (2012), “Sargassummyriocystum mediated biosynthesis of gold nanoparticles,” *Spectrochimica Acta Part A: Molecular and Biomolecular Spectroscopy*, **99**;97–101.

Stegenga, H., Bolton, J. J. and Anderson, R. J. (1997) Seaweeds of the South African West Coast. Contributions from the Bolus herbarium. Number **18**. 655 pg.

van den Hoek, C. (1982a) Phytogeographic distribution groups of benthic marine algae in the North Atlantic Ocean. - *Helgolinder Meeresunters*; **35**: 153-214.

van den Hoek, C. (1982b) The distribution of benthic marine algae in relation to the temperature regulation of their life histories. - *Biol. J. Linn. Soc. Lond*; **18**: 81-144.

van den Hoek, C., Mann, D. G. and Jahns, H. M. (1995) Algae, An introduction to phycology. Cambridge University Press. Cambridge. Pg 390 – 408.

Wang ZL (2000). Transmission Electron Microscopy of Shape-Controlled Nanocrystals and Their Assemblies. *J. Phys. Chem. B*; **104**:1153-1175.

Winey M, Meehl JB, O’Toolea ET & Giddings TH Jr. (2013). Conventional transmission electron microscopy. *Mol Biol Cell*; 25:319-323.

Yasantha A, Lee KW, Kim SK & Jeon YJ (2007). Anticoagulant activity of marine green and brown algae collected from Jeju Island in Korea. *Bioresource Technol*; **98**:1711-1716.

Yaich H, Garna H, Besbes S , Paquot M, Blecker C, Attia H (2011). Chemical composition and functional properties of Ulva lactuca seaweed collected in Tunisia. *Food Chem*; **128**:895–901.

Appendix

7.1 ^{1}H and ^{13}C data

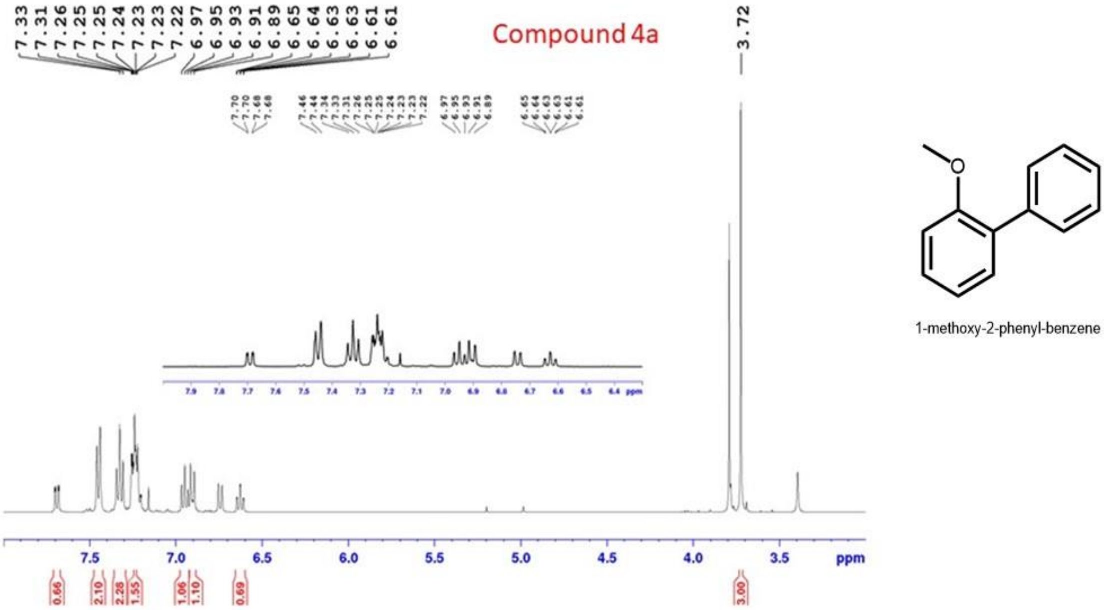

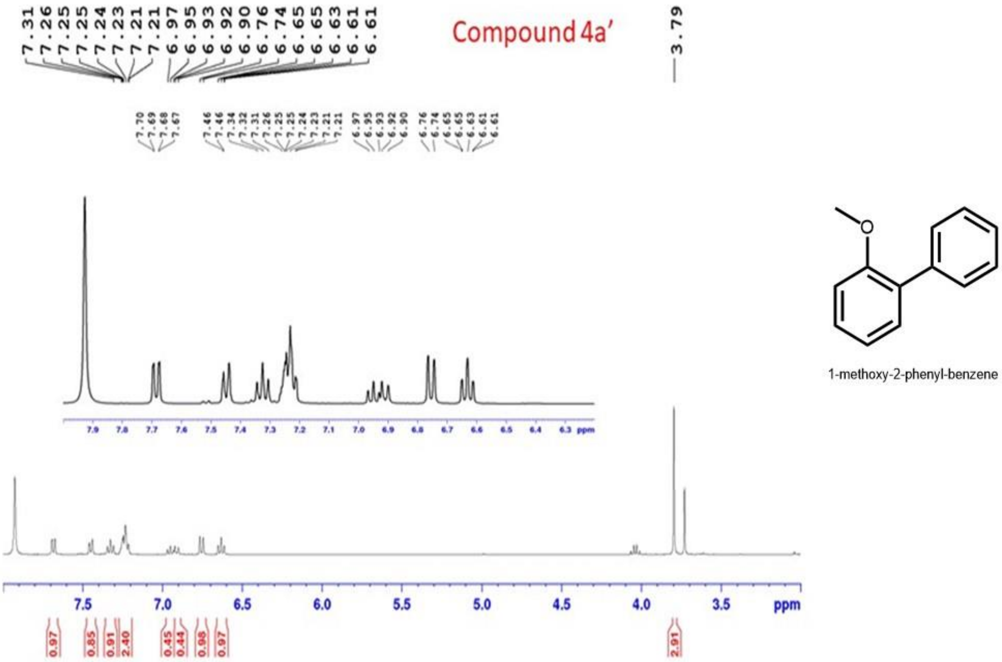

Compound 4a

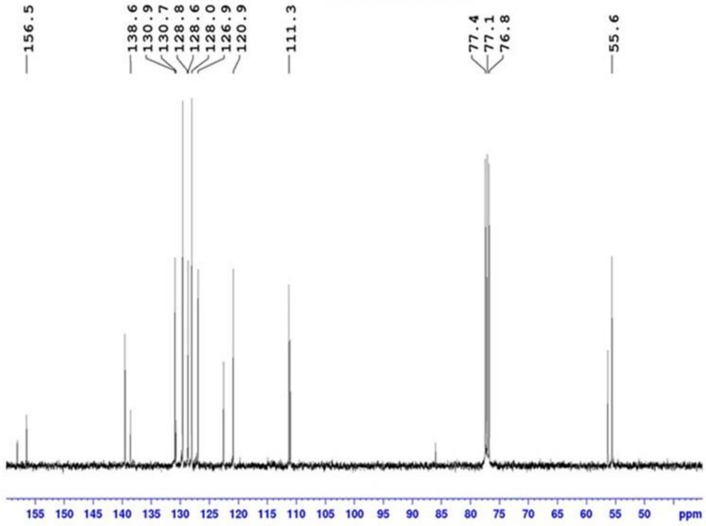

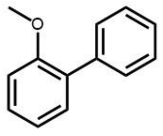

1-methoxy-2-phenyl-benzene

Compound 4a'

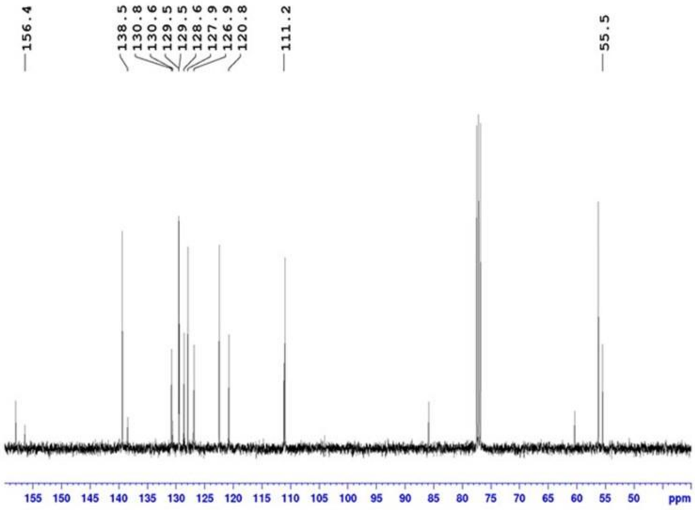

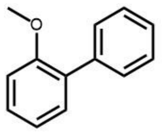

1-methoxy-2-phenyl-benzene

Compound 4b

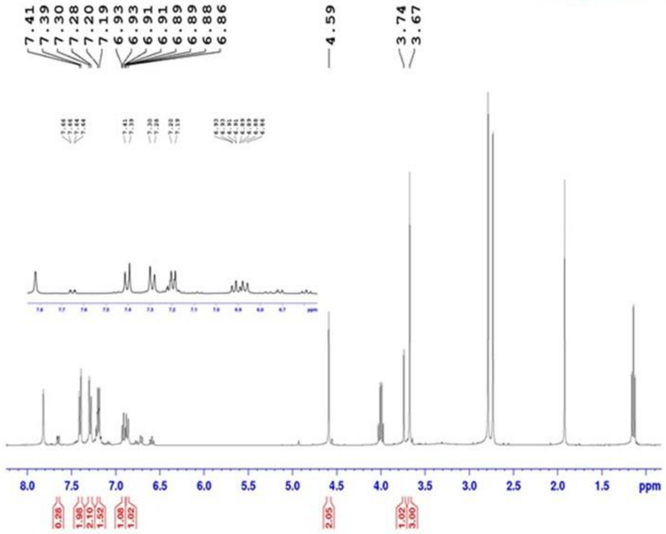

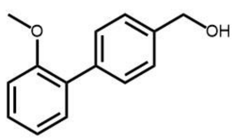

[4(2-methoxyphenyl)phenyl]methanol

Compound 4b'

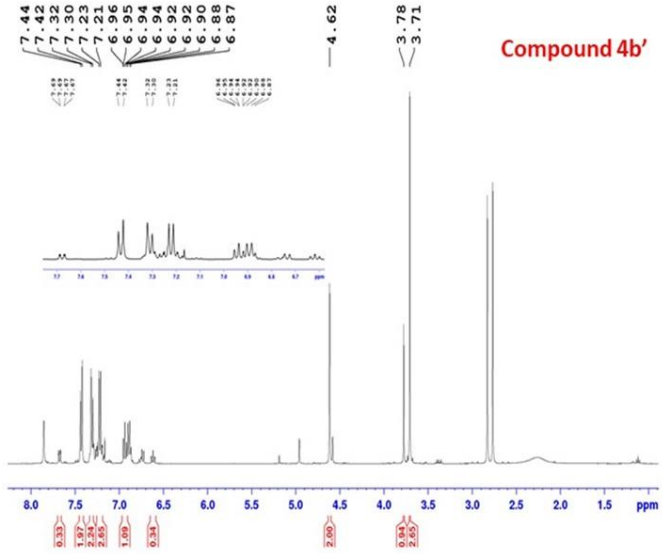

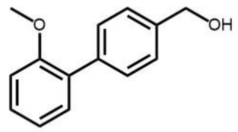

[4(2-methoxyphenyl)phenyl]methanol

Compound 4b

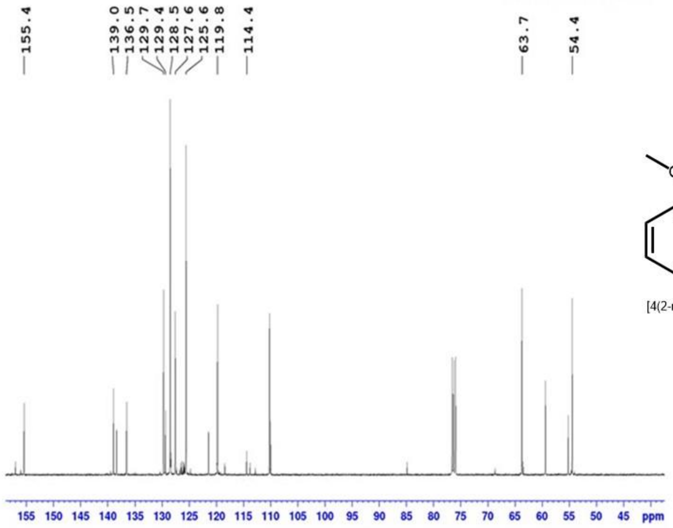

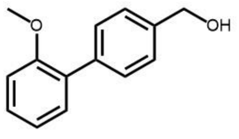

[4(2-methoxyphenyl)phenyl]methanol

Compound 4b'

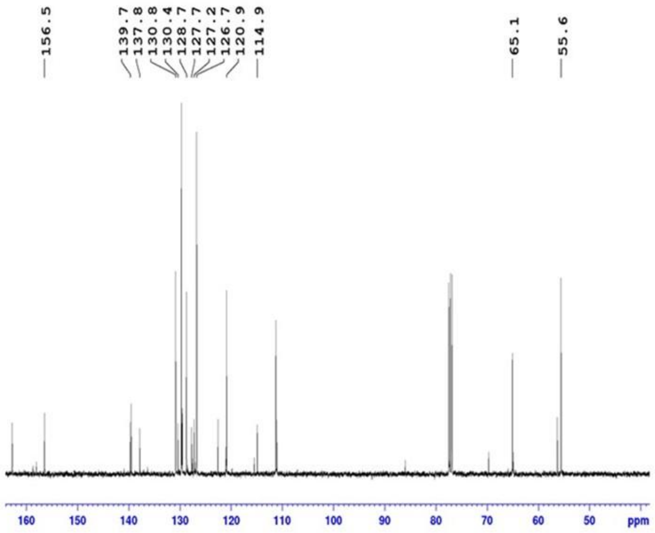

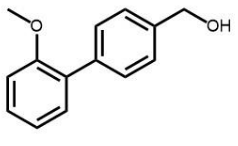

[4(2-methoxyphenyl)phenyl]methanol

Compound 4c

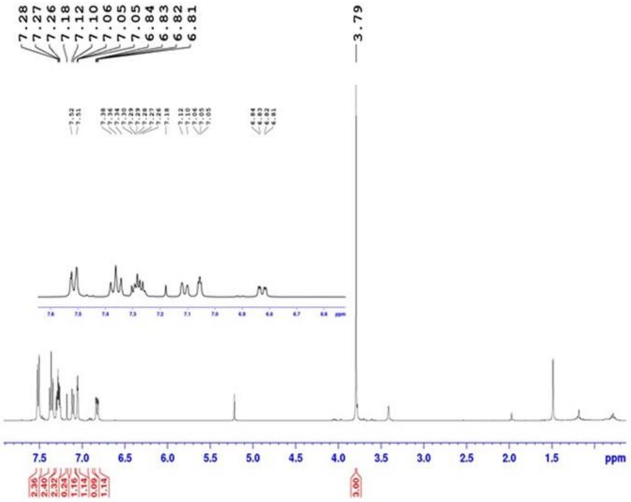

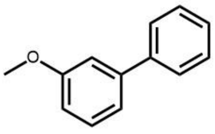

1-methoxy-3-phenyl-benzene

Compound 4c'

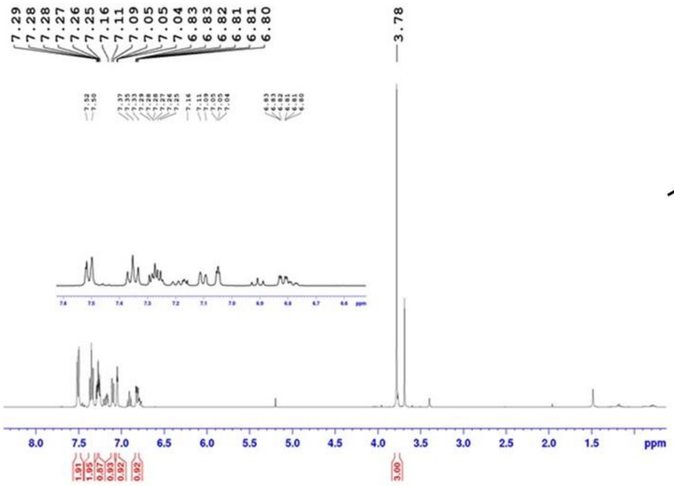

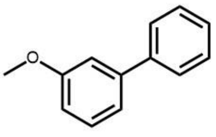

1-methoxy-3-phenyl-benzene

Compound 4c

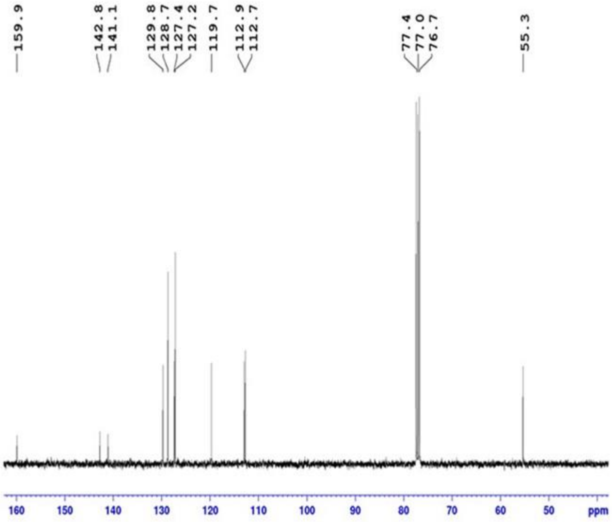

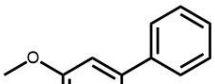

1-methoxy-3-phenyl-benzene

Compound 4c’

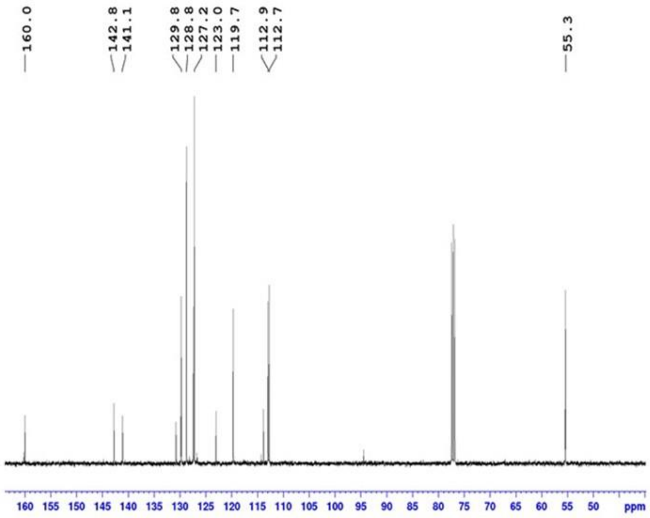

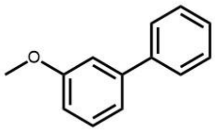

1-methoxy-3-phenyl-benzene

Compound 4d

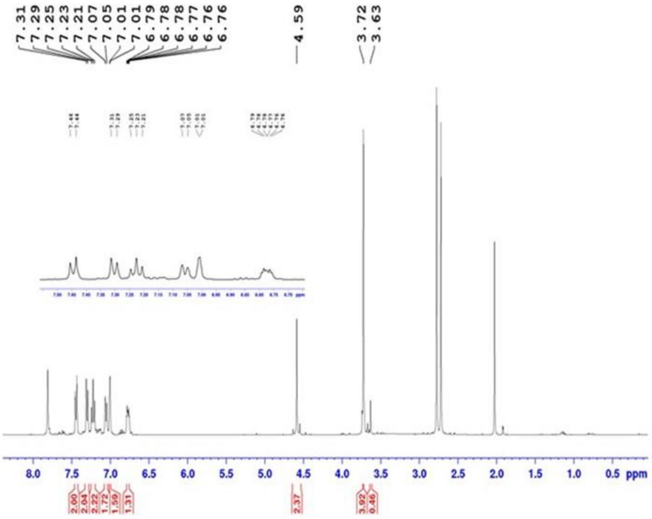

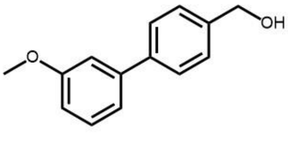

[4-(3-methoxyphenyl)phenyl]methanol

Compound 4d'

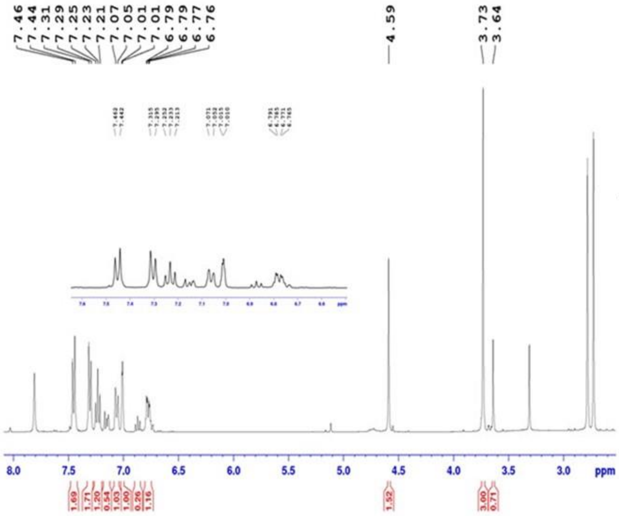

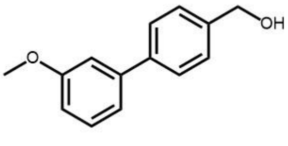

[4-(3-methoxyphenyl)phenyl]methanol

Compound 4d

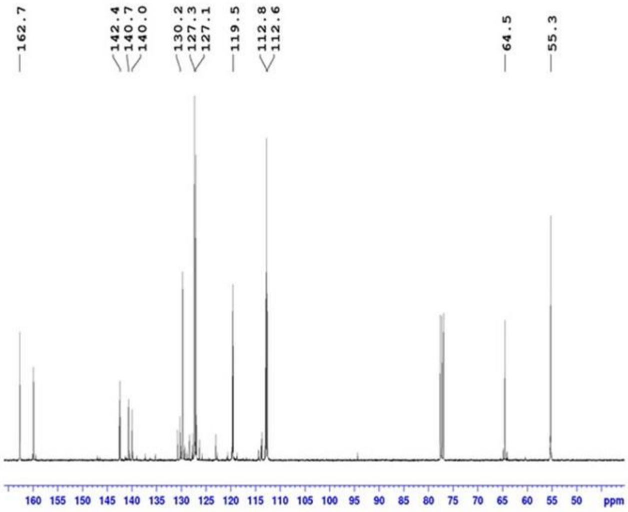

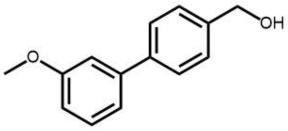

[4-(3-methoxyphenyl)phenyl]methanol

Compound 4d'

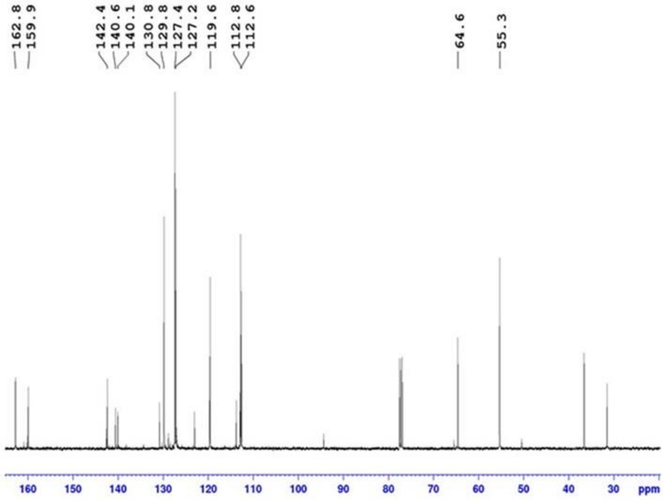

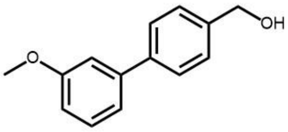

[4-(3-methoxyphenyl)phenyl]methanol

Compound 4e

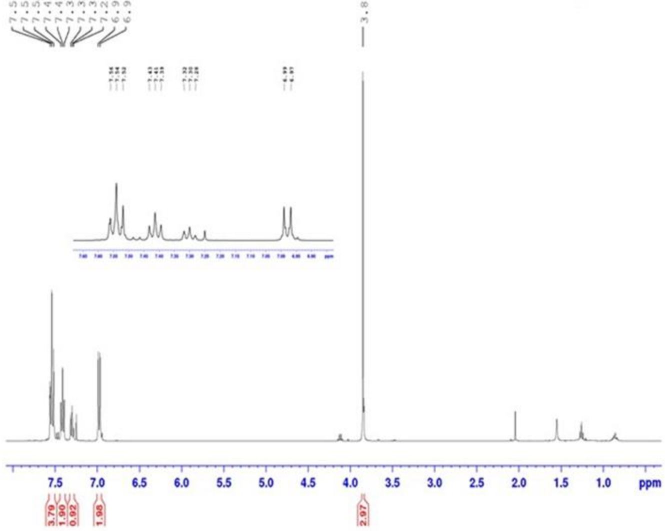

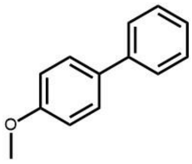

1-methoxy-4-phenyl-benzene

Compound 4e’

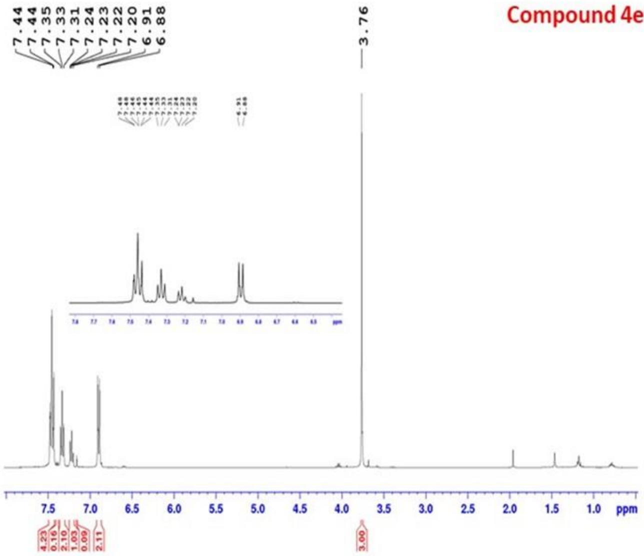

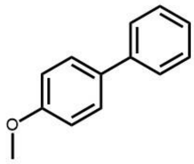

1-methoxy-4-phenyl-benzene

Compound 4e

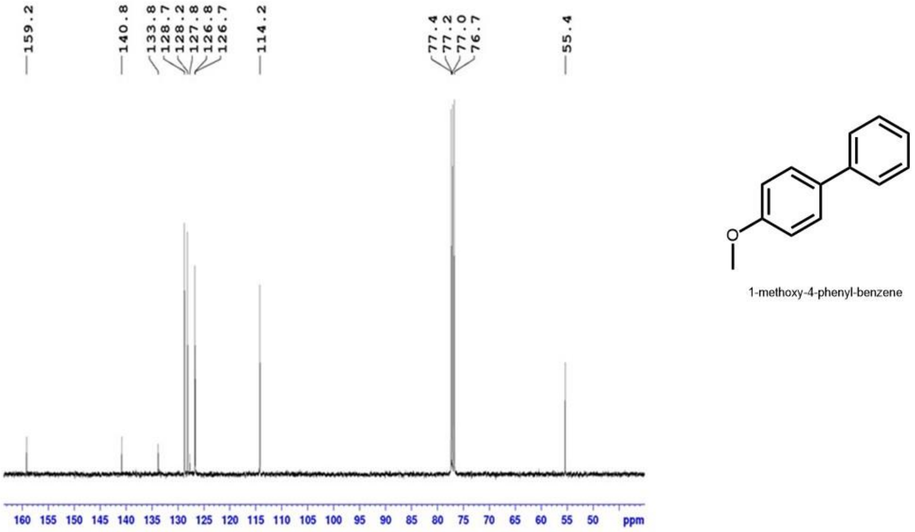

Compound 4e'

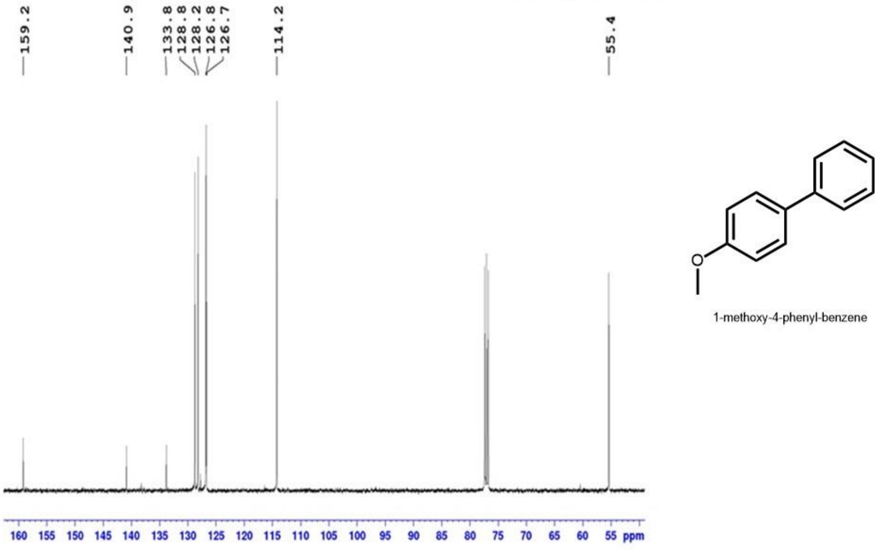

Compound 4f

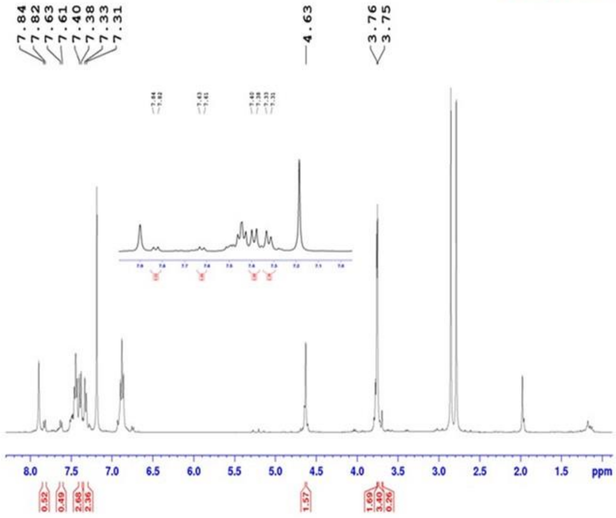

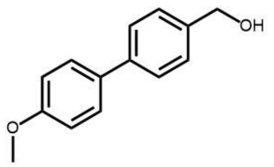

[4-(4-methoxyphenyl)phenyl]methanol

Compound 4f’

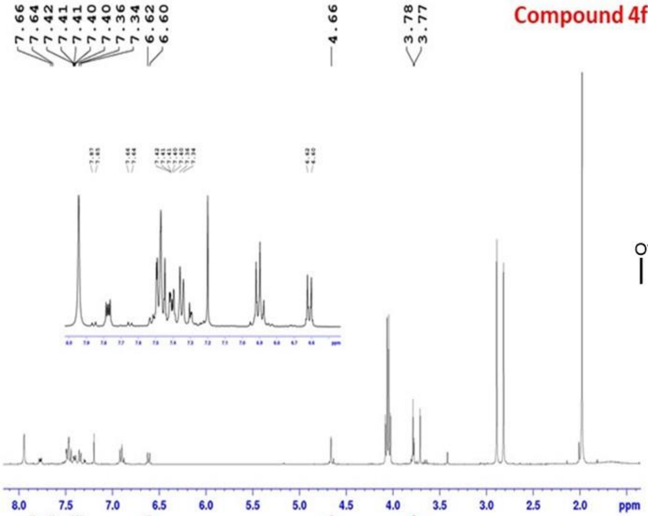

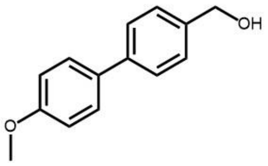

[4-(4-methoxyphenyl)phenyl]methanol

Compound 4f

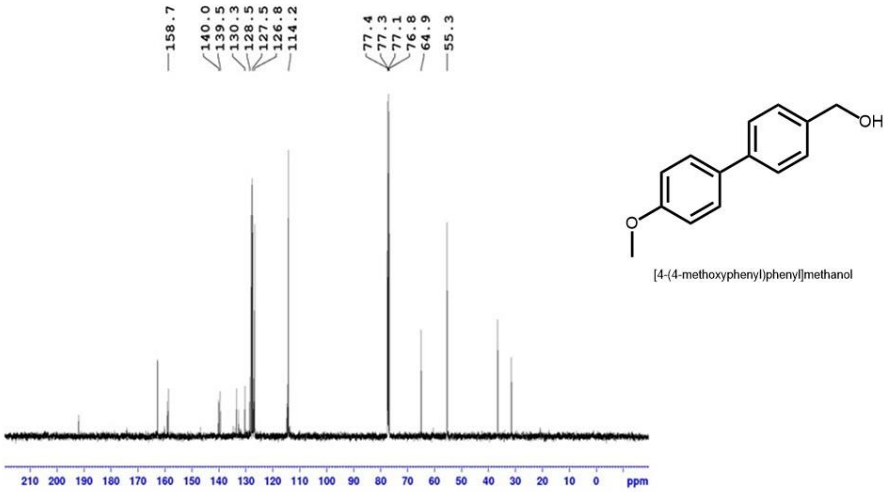

[4-(4-methoxyphenyl)phenyl]methanol

Compound 4f’

[4-(4-methoxyphenyl)phenyl]methanol

7.2 GC-EIMS data

Compound 4a

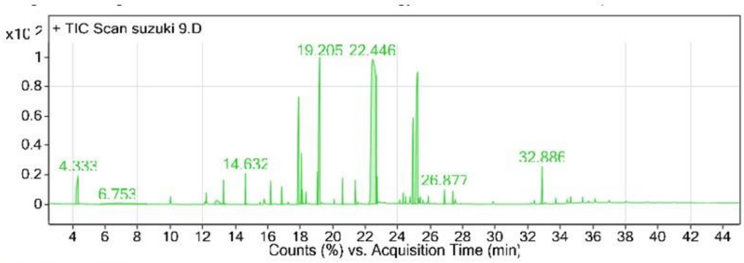

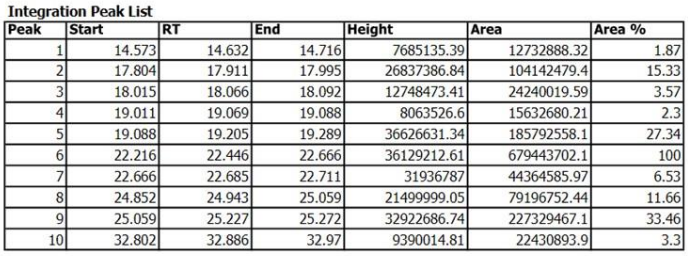
Integration Peak List

Peak	Start	RT	End	Height	Area	Area %
1	14.573	14.632	14.716	7685135.39	12732888.32	1.87
2	17.804	17.911	17.995	26837386.84	104142479.4	15.33
3	18.015	18.066	18.092	12748473.41	24240019.59	3.57
4	19.011	19.069	19.088	8063526.6	15632680.21	2.3
5	19.088	19.205	19.289	36626631.34	185792558.1	27.34
6	22.216	22.446	22.666	36129212.61	679443702.1	100
7	22.666	22.685	22.711	31936787	44364585.97	6.53
8	24.852	24.943	25.059	21499999.05	79196752.44	11.66
9	25.059	25.227	25.272	32922686.74	227329467.1	33.46
10	32.802	32.886	32.97	9390014.81	22430893.9	3.3

Compound 4a’

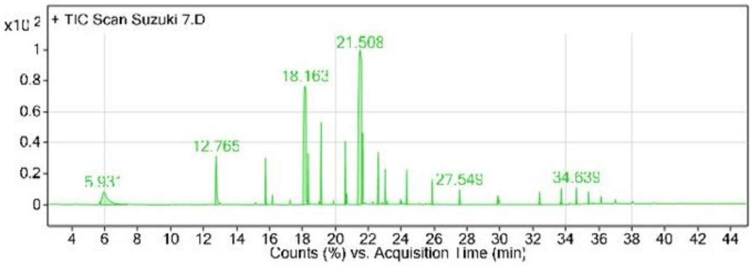


Integration Peak List

Peak	Start	RT	End	Height	Area	Area %
1	12.687	12.765	12.963	11809155.72	50778493.91	11.07
2	15.706	15.757	15.88	11269626	23047247.4	5.02
3	18.013	18.163	18.312	28741446.28	277499188.9	60.49
4	18.312	18.351	18.474	12407117	22655407.52	4.94
5	19.082	19.14	19.224	19950600.15	38551965.97	8.4
6	20.55	20.608	20.66	15355707.17	27970691.96	6.1
7	21.341	21.508	21.611	37507402.94	458749325.5	100
8	21.611	21.669	21.753	17191334.23	30270387.04	6.6
9	22.526	22.607	22.685	12652680.45	29672562.49	6.47
10	22.986	23.028	23.111	8579310.39	13741413.07	3

Compound 4a

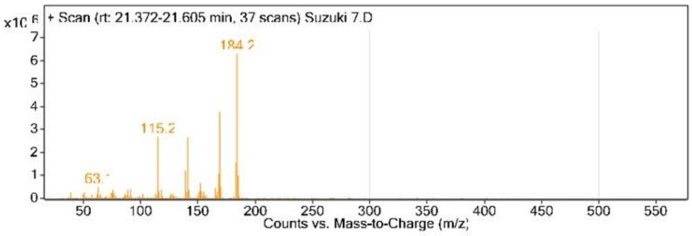

Peak List

m/z	z	Abund
115.2	1	2679699
139.2		1207813.25
141.2	1	2657053.5
152.2		658504.63
168.2		1058549.63
169.2	1	3756992
170.2	1	504112.22
183.2		1554435.5
184.2	1	6305390.5

Compound 4a’

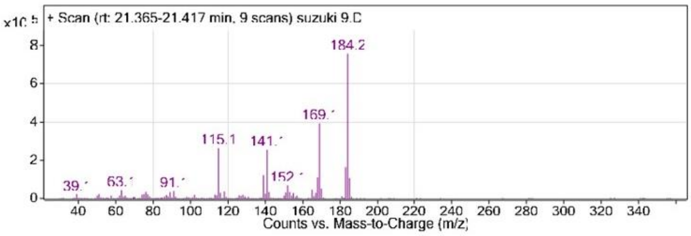

Peak List

m/z	z	Abund
115.1	1	262483.56
139.1		122078.22
141.1	1	253901.33
152.1		68235.55
168.1		109604.45
169.1	1	392827.56

Compound 4b

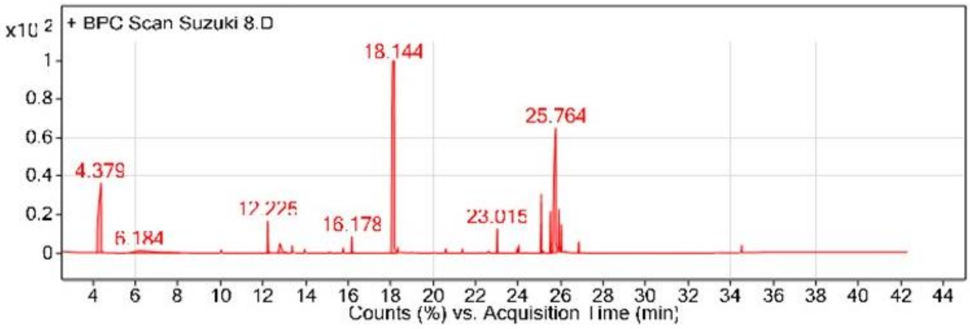

Integration Peak List

Peak	Start	RT	End	Height	Area	Area %
1	4.181	4.379	4.463	3049178.96	24623803.49	38.27
2	12.187	12.225	12.309	1398497.1	2608006.5	4.05
3	16.143	16.178	16.301	725023.33	1167193.16	1.81
4	18.008	18.144	18.325	8380139.93	64350457.22	100
5	22.977	23.015	23.054	1056883.28	1626638.35	2.53
6	25.037	25.085	25.163	2571219.9	4233683.09	6.58
7	25.48	25.518	25.602	1826158.92	2820714.88	4.38
8	25.616	25.764	25.848	5440177.09	32085479.65	49.86
9	25.9	25.926	26.003	1829972.19	2848960.5	4.43
10	26.003	26.036	26.12	1185169.76	1777246.52	2.76

Compound 4b’

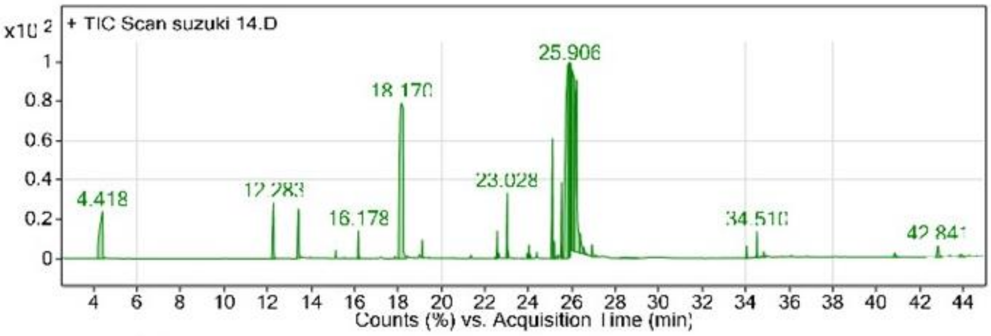

Integration Peak List

Peak	Start	RT	End	Height	Area	Area %
1	12.182	12.283	12.368	10169634.54	36109128.64	11.2
2	18.002	18.17	18.409	28314698.68	322420733.1	100
3	22.977	23.028	23.047	11892003.48	19865814.84	6.16
4	25.014	25.111	25.156	21816734.67	54002332.89	16.75
5	25.473	25.531	25.564	13901673.67	26163804.82	8.11
6	25.609	25.835	25.842	35444068.67	305485937.2	94.75
7	25.842	25.906	25.939	35480987.45	205258449.6	63.66
8	25.939	25.958	26.003	33949908.03	128543376.7	39.87
9	26.003	26.029	26.126	32714429.23	216781973.4	67.24
10	26.126	26.217	26.359	31327109.96	189289328.6	58.71

Compound 4b

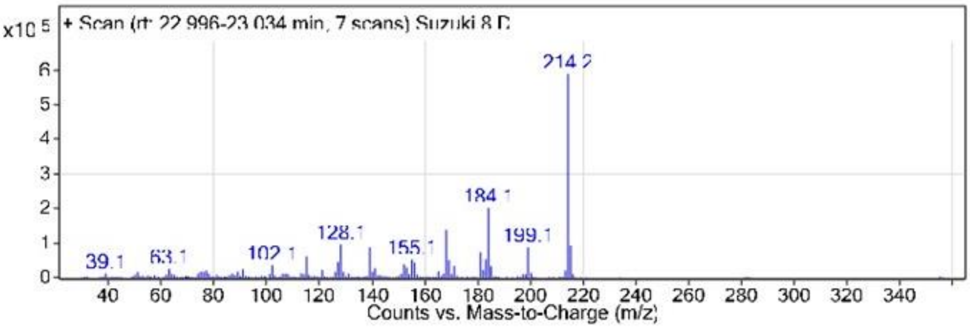

Peak List

m/z	z	Abund
115.1	1	60348.71
128.1		95105.14
139.1		87204.57
168.1		136995.42
181.1		72194.14
183.1		51775.29
184.1	1	201092.58
199.1	1	86686
214.2	1	588452.56
215.2	1	91317.71

Compound 4b’

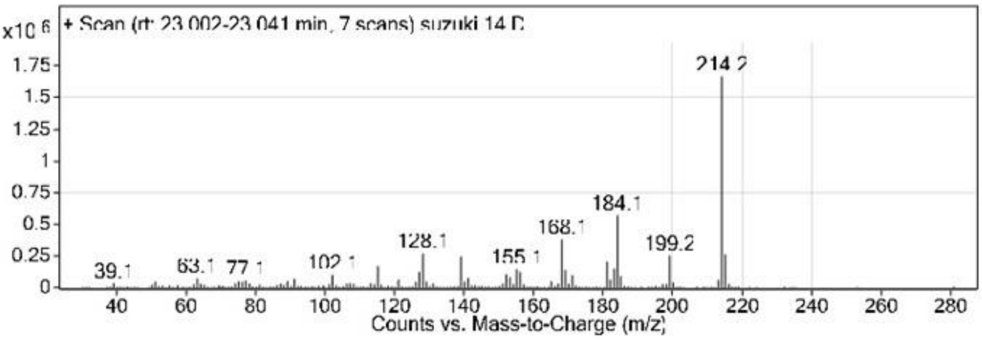

Peak List

m/z	z	Abund
115.1	1	167982.86
128.1		266668.56
139.1		241184
168.1		378262.84
181.1		201988.58
183.2		147801.14
184.1	1	568155.44
199.2	1	250553.14
214.2	1	1665307.38

Compound 4c

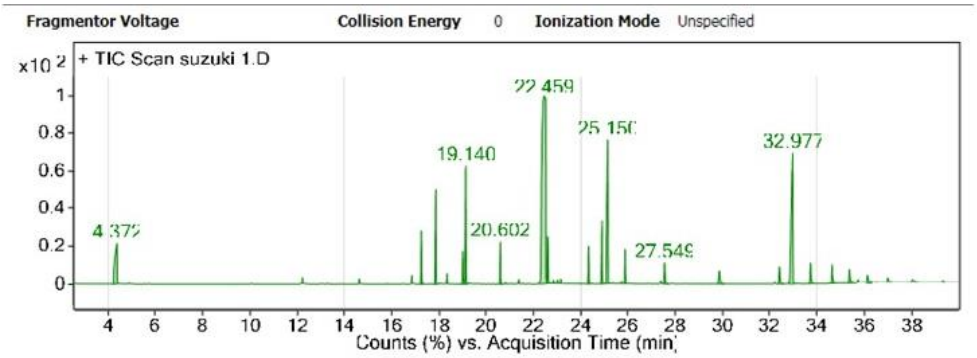

Integration Peak List

Peak	Start	RT	End	Height	Area	Area %
1	4.224	4.372	4.418	7467726.34	47886359.16	12.21
2	17.206	17.258	17.342	9867947.37	15063379.31	3.84
3	17.801	17.872	17.956	17469348.56	35191218.62	8.97
4	19.076	19.14	19.224	21860781.15	45690201.16	11.65
5	20.55	20.602	20.686	7776292.63	12362886.12	3.15
6	22.226	22.459	22.569	34787517.06	392318264.9	100
7	22.569	22.607	22.73	8586008.26	16528698.7	4.21
8	24.848	24.904	24.988	11627173.38	21762318.37	5.55
9	25.047	25.15	25.234	26619799.9	85116674.5	21.7
10	32.815	32.977	33.061	24196343.69	116054784.3	29.58

Compound 4c’

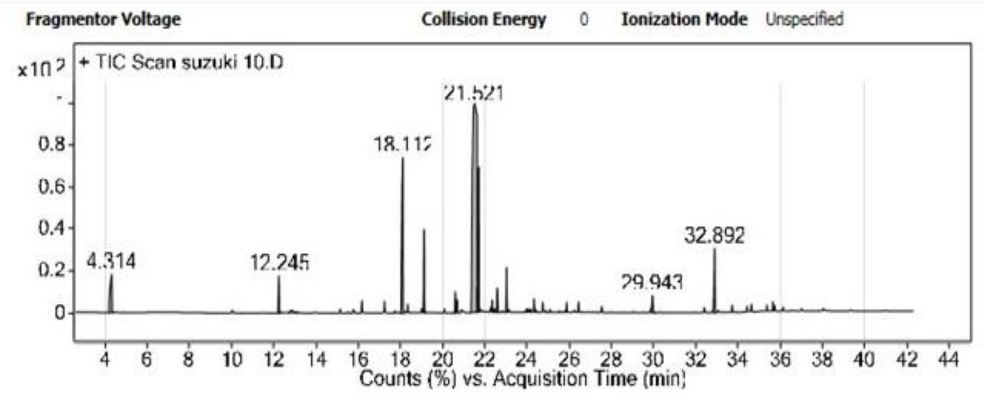

Integration Peak List

Peak	Start	RT	End	Height	Area	Area %
1	4.185	4.314	4.398	6791757.11	38340820.02	7.49
2	12.167	12.245	12.329	6554422.56	15841121.1	3.09
3	17.995	18.112	18.196	27417317.68	105660999.5	20.63
4	19.075	19.121	19.205	14727528.51	25583090.75	5
5	20.55	20.602	20.647	3781754.86	6134106.88	1.2
6	21.34	21.521	21.637	36832700.78	512163099.8	100
7	21.637	21.715	21.786	25542881.7	85745166.7	16.74
8	22.543	22.588	22.659	4326003.13	11266441.87	2.2
9	22.982	23.028	23.092	7895283.5	12366115.98	2.41
10	32.789	32.892	32.976	11283055.63	31740470.79	6.2

Compound 4c’

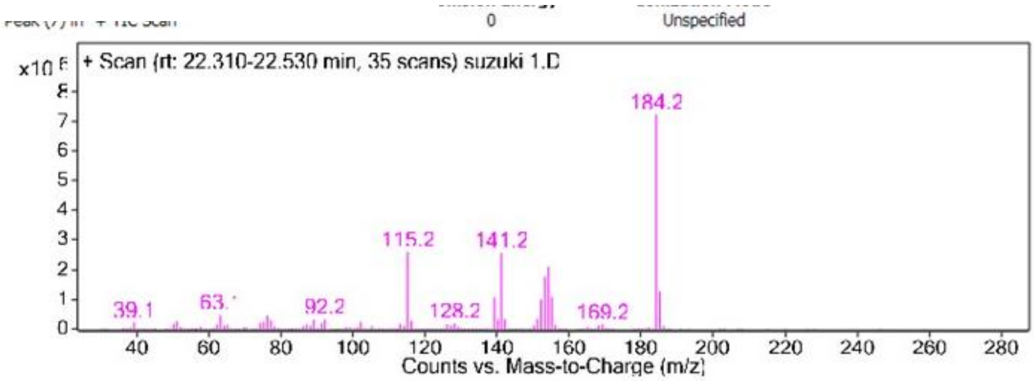

Peak List

m/z	z	Abund
63.1		454660.34
115.2	1	2584501
139.2		1057880.5
141.2	1	2560848.5
152.2		982424.94
153.2		1763072
154.2		2089512.25
155.2	1	1077600.63
184.2	1	7212829.5
185.2	1	1260706.75

Compound 4c’

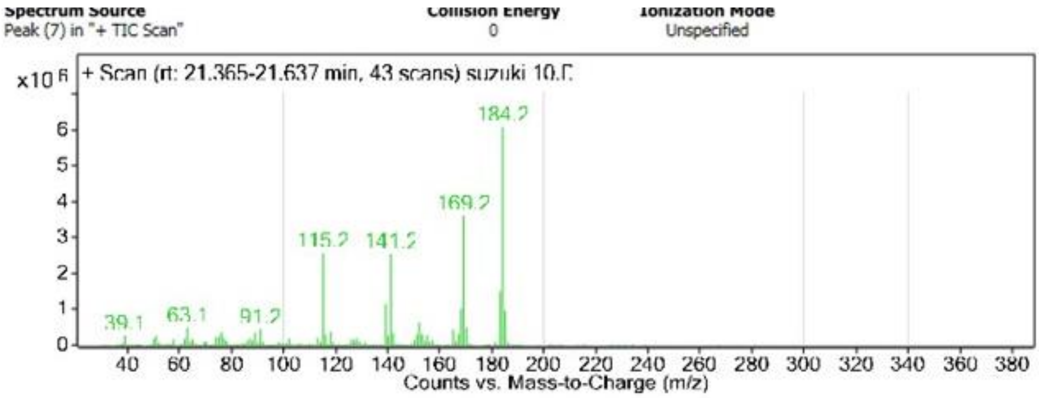

Peak List

m/z	z	Abund
115.2	1	2563755.75
139.2		1147647.5
141.2	1	2544379.5
152.2		628637.56
168.2		1014464
169.2	1	3605752.5
170.2	1	485256.56
183.2		1494555.5
184.2	1	6074153.5
185.2	1	951587.19

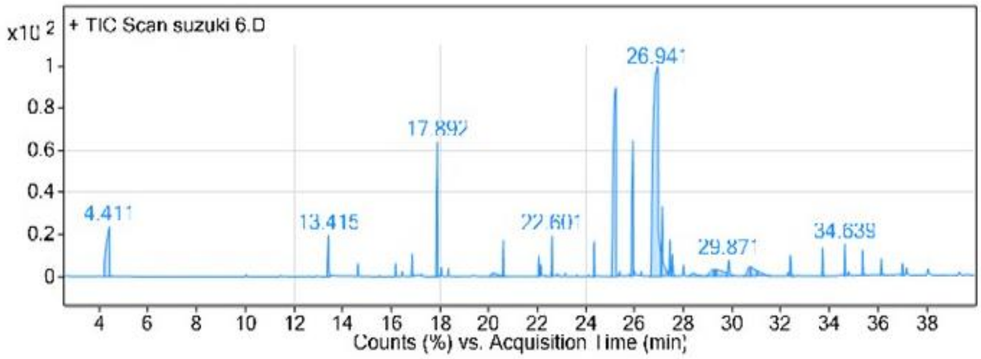

Integration Peak List

Peak	Start	RT	End	Height	Area	Area %
1	4.197	4.411	4.495	8381213.2	76173160.99	14.39
2	13.347	13.415	13.499	6967624.74	19097303.24	3.61
3	17.782	17.892	17.969	22655437.65	61030517.17	11.53
4	20.55	20.602	20.686	6106561.69	9874242.8	1.87
5	22.555	22.601	22.64	6822045.56	10981161.17	2.07
6	25.046	25.227	25.337	31734972.58	250211385	47.27
7	25.834	25.926	25.958	22871634.81	71941663.48	13.59
8	26.625	26.941	27.09	35336420.84	529272380.8	100
9	27.09	27.135	27.316	11684247.94	43058533.57	8.14
10	27.4	27.452	27.504	6064608.48	13537968.4	2.56

Compound 4d’

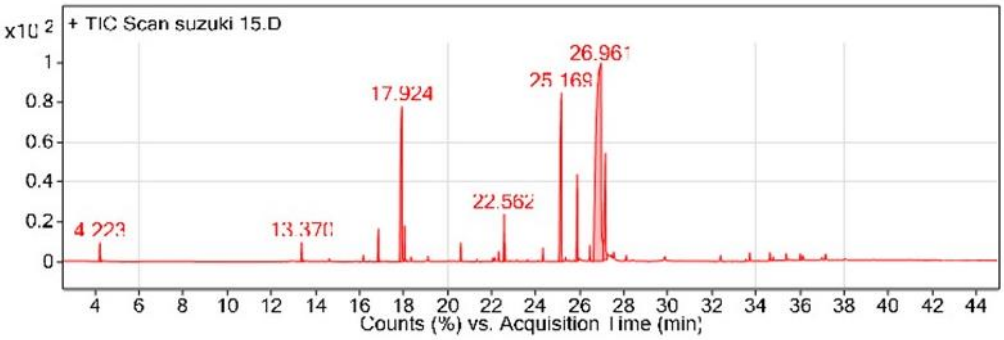

Integration Peak List

Peak	Start	RT	End	Height	Area	Area %
1	4.185	4.223	4.307	3374675.32	8592574.91	1.52
2	13.332	13.37	13.493	3444990.12	7315624.79	1.29
3	16.811	16.857	16.941	5884350.48	10927701.92	1.93
4	17.799	17.924	18.008	27769982.56	132393302.2	23.37
5	18.014	18.047	18.163	6290107.8	10320694.73	1.82
6	22.52	22.562	22.581	8461501.96	13471717.72	2.38
7	25.045	25.169	25.246	30151699.62	135793400	23.97
8	25.809	25.887	25.939	15554583.65	33042159.3	5.83
9	26.606	26.961	27.071	35541145.18	566597983.5	100
10	27.071	27.161	27.245	19087475.95	69750506.19	12.31

Compound 4d

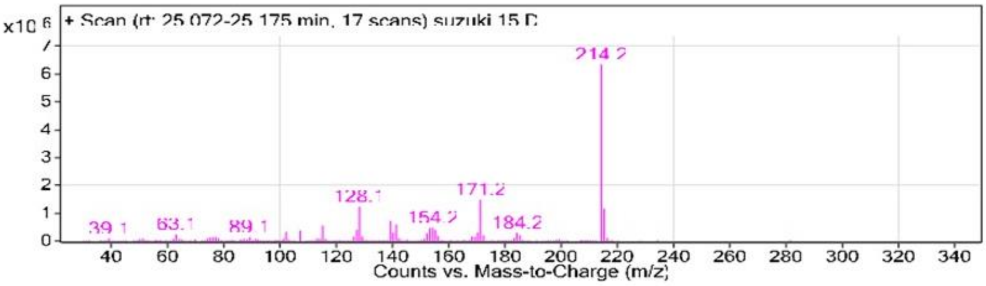

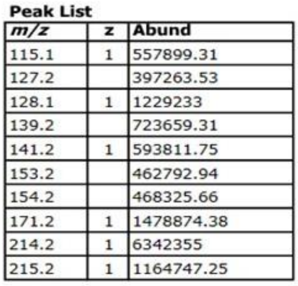

Peak List

m/z	z	Abund
115.1	1	557899.31
127.2		397263.53
128.1	1	1229233
139.2		723659.31
141.2	1	593811.75
153.2		462792.94
154.2		468325.66
171.2	1	1478874.38
214.2	1	6342355
215.2	1	1164747.25

Compound 4d’

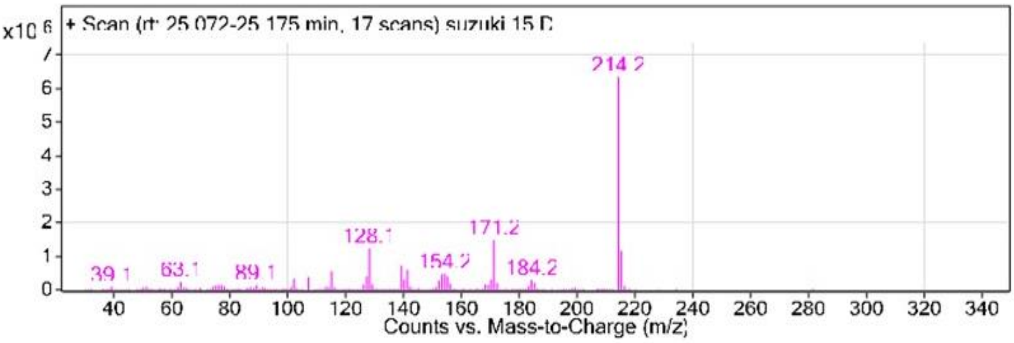

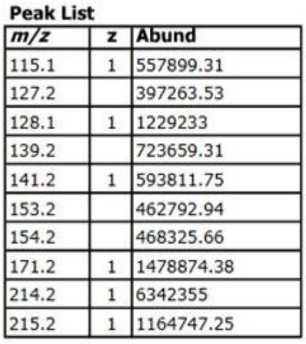

Peak List

m/z	z	Abund
115.1	1	557899.31
127.2		397263.53
128.1	1	1229233
139.2		723659.31
141.2	1	593811.75
153.2		462792.94
154.2		468325.66
171.2	1	1478874.38
214.2	1	6342355
215.2	1	1164747.25

Compound 4e

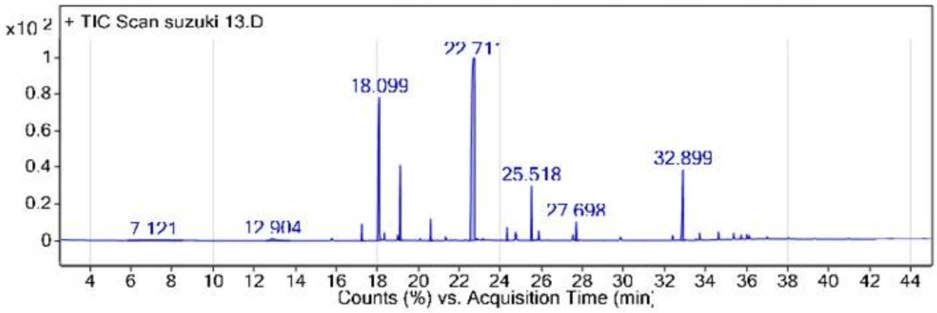

Integration Peak List

Peak	Start	RT	End	Height	Area	Area %
1	12.581	12.904	13.745	317332.11	5482402.73	1.56
2	17.213	17.245	17.368	3156215.45	4853020.81	1.38
3	17.991	18.099	18.183	27202382.75	112252761	31.85
4	19.069	19.121	19.205	14347017.62	24088841.11	6.83
5	20.55	20.596	20.718	4111681.41	6621565.27	1.88
6	22.488	22.711	22.834	34667408.48	352478084.6	100
7	24.283	24.328	24.373	2466579.58	4063503.09	1.15
8	25.466	25.518	25.641	10340929.44	18866566.98	5.35
9	27.64	27.698	27.815	3531406.26	7890661.62	2.24
10	32.776	32.899	32.983	13390309.27	41419102.11	11.75

Compound 4e’

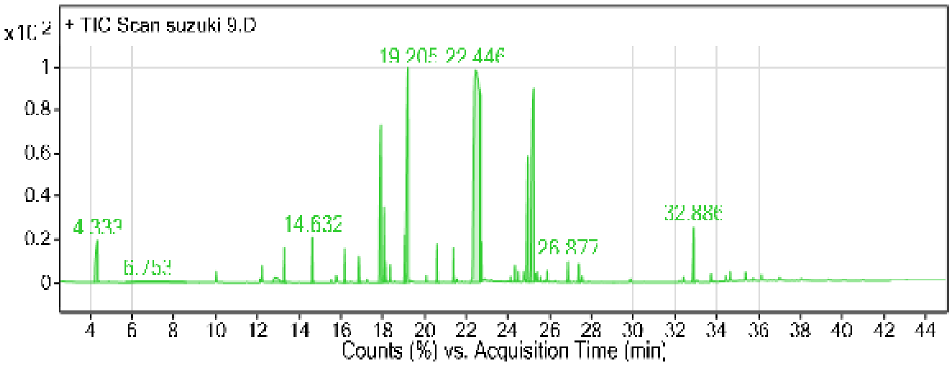

Integration Peak List

Peak	Start	RT	End	Height	Area	Area %
1	14.573	14.632	14.716	7685135.39	12732888.32	1.87
2	17.804	17.911	17.995	26837386.84	104142479.4	15.33
3	18.015	18.066	18.092	12748473.41	24240019.59	3.57
4	19.011	19.069	19.088	8063526.6	15632680.21	2.3
5	19.088	19.205	19.289	36626631.34	185792558.1	27.34
6	22.216	22.446	22.666	36129212.61	679443702.1	100
7	22.666	22.685	22.711	31936787	44364585.97	6.53
8	24.852	24.943	25.059	21499999.05	79196752.44	11.66
9	25.059	25.227	25.272	32922686.74	227329467.1	33.46
10	32.802	32.886	32.97	9390014.81	22430893.9	3.3

Compound 4e

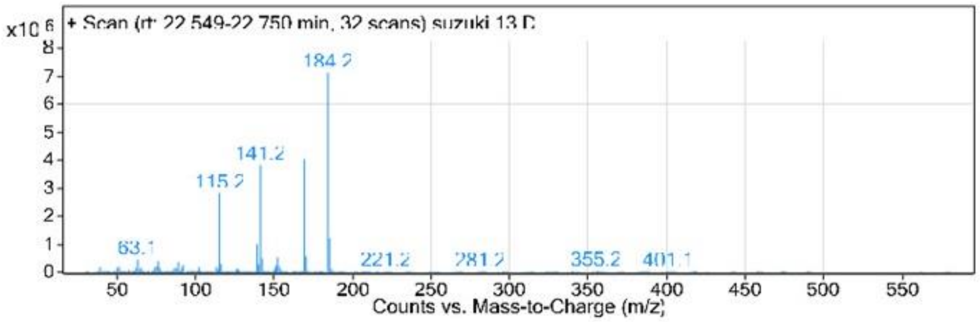

Peak List

m/z	z	Abund
63.1		447373.5
115.2	1	2818358
139.2		997222
141.2	1	3824872
142.2	1	481168.5
152.2		522602
169.2	1	4034806
170.2	1	567274.75
184.2	1	7130080
185.2	1	1206028

Compound 4e'

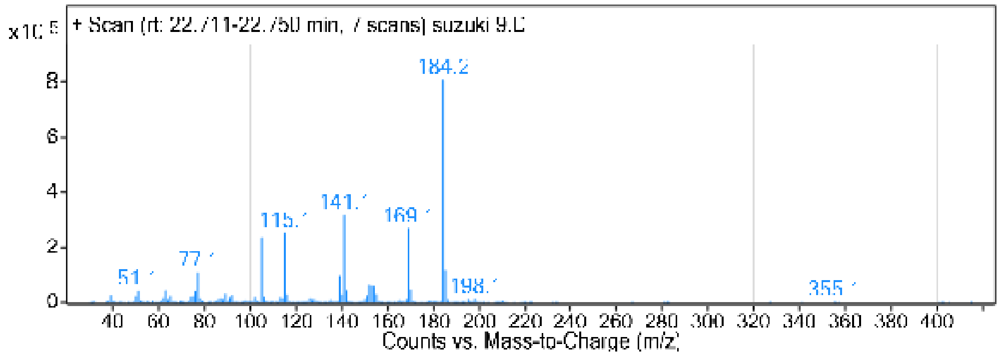

Peak List

m/z	z	Abund
77.1		107013.71
105.1	1	233360.86
115.1	1	250950.86
139.1		94892.57
141.1	1	316692.56
152.1		62418.29
153.1		58793.14
169.1	1	267951
184.2	1	807113.13
185.2	1	114774.86

Compound 4f

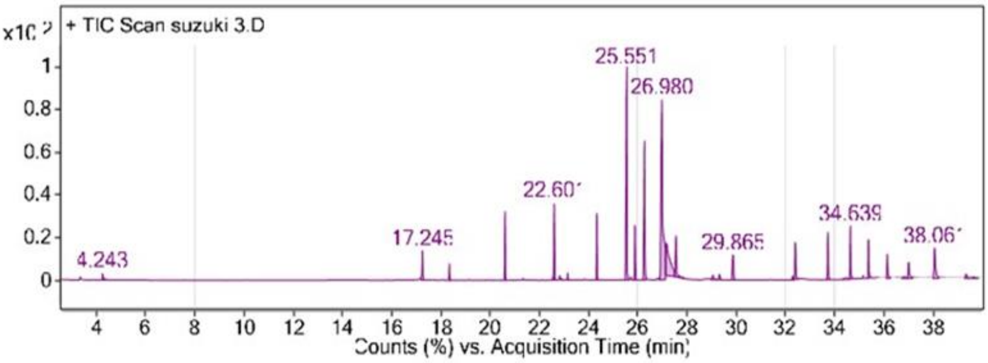

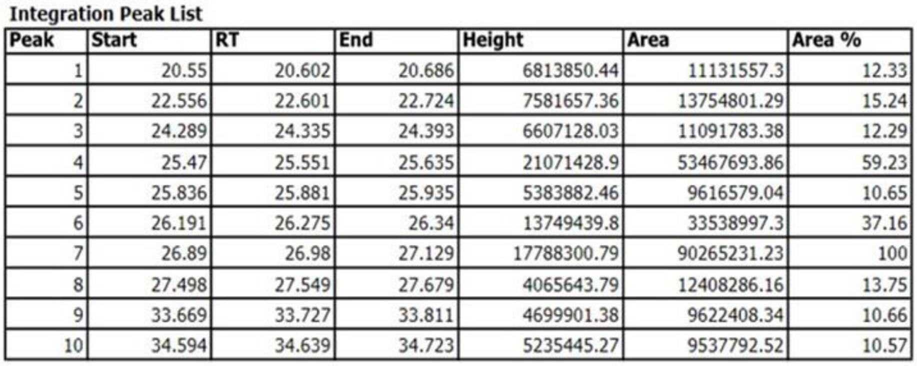

Integration Peak List

Peak	Start	RT	End	Height	Area	Area %
1	20.55	20.602	20.686	6813850.44	11131557.3	12.33
2	22.556	22.601	22.724	7581657.36	13754801.29	15.24
3	24.289	24.335	24.393	6607128.03	11091783.38	12.29
4	25.47	25.551	25.635	21071428.9	53467693.86	59.23
5	25.836	25.881	25.935	5383882.46	9616579.04	10.65
6	26.191	26.275	26.34	13749439.8	33538997.3	37.16
7	26.89	26.98	27.129	17788300.79	90265231.23	100
8	27.498	27.549	27.679	4065643.79	12408286.16	13.75
9	33.669	33.727	33.811	4699901.38	9622408.34	10.66
10	34.594	34.639	34.723	5235445.27	9537792.52	10.57

Compound 4f’

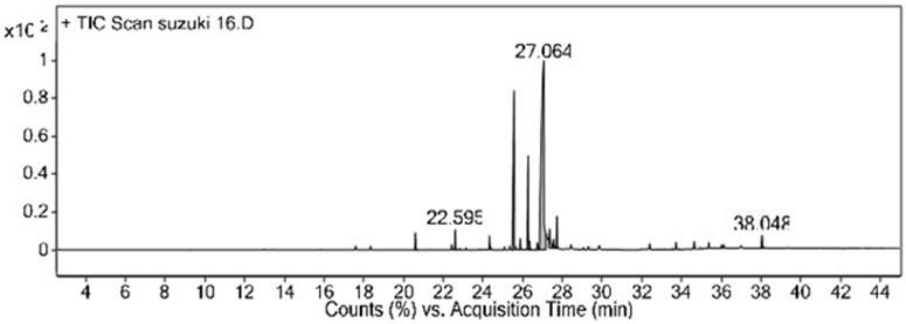

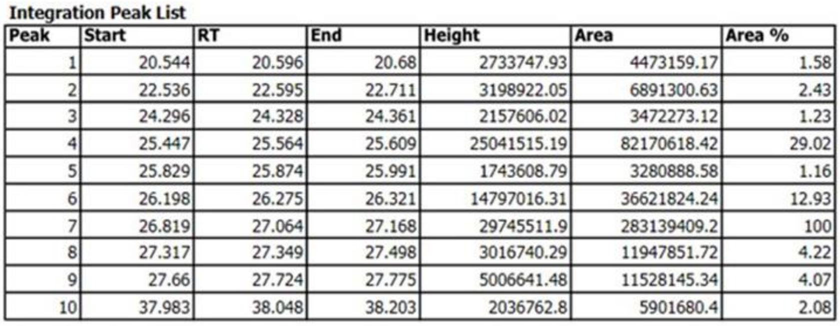

Integration Peak List

Peak	Start	RT	End	Height	Area	Area %
1	20.544	20.596	20.68	2733747.93	4473159.17	1.58
2	22.536	22.595	22.711	3198922.05	6891300.63	2.43
3	24.296	24.328	24.361	2157606.02	3472273.12	1.23
4	25.447	25.564	25.609	25041515.19	82170618.42	29.02
5	25.829	25.874	25.991	1743608.79	3280888.58	1.16
6	26.198	26.275	26.321	14797016.31	36621824.24	12.93
7	26.819	27.064	27.168	29745511.9	283139409.2	100
8	27.317	27.349	27.498	3016740.29	11947851.72	4.22
9	27.66	27.724	27.775	5006641.48	11528145.34	4.07
10	37.983	38.048	38.203	2036762.8	5901680.4	2.08

Compound 4f

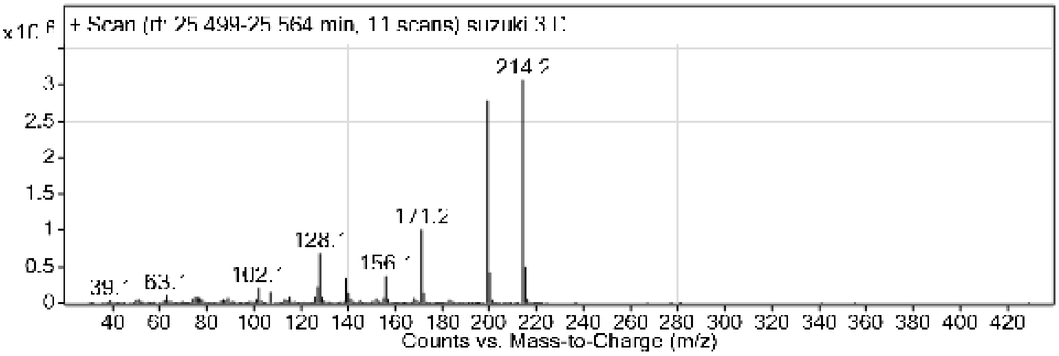

Peak List

m/z	z	Abund
102.1		202659.64
127.1		220126.55
128.1	1	680570.19
139.1		335925.81
156.1	1	365253.09
171.2	1	1006144
199.2	1	2783616
200.2	1	411560.72
214.2	1	3063779

Compound 4f’

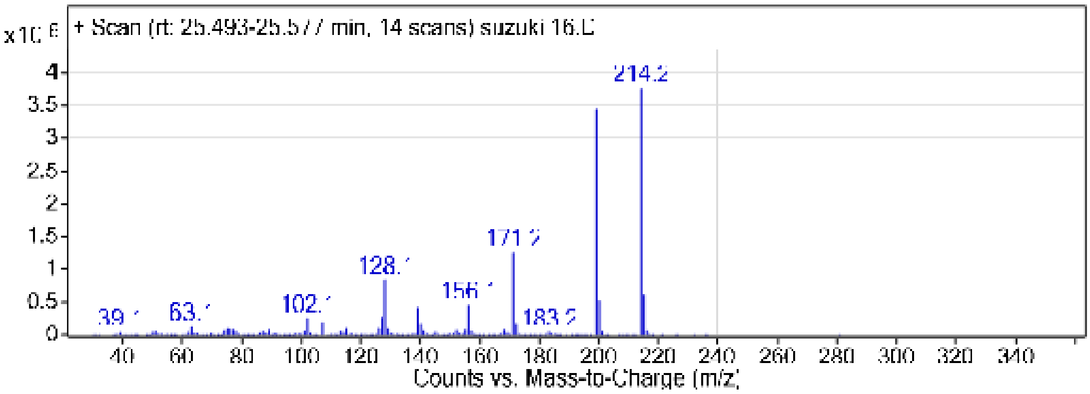

Peak List

m/z	z	Abund
102.1		247801.72
127.1		270367.44
128.1	1	834285.69
139.1		409282.84
156.1	1	448188
171.2	1	1250752
199.2	1	3434628.5
200.2	1	519250.28
214.2	1	3750020.5
215.2	1	610552